NTNU

Norwegian University of
Science and Technology

Exploring the interaction capacities of microorganisms by the use of high-resolution experimental tools

Lilli Theres Eilertsen Bay

Biotechnology (5 year)
Submission date: June 2018
Supervisor: Marit Sletmoen, IBT

Norwegian University of Science and Technology
Department of Biotechnology and Food Science

Preface

This thesis is submitted to the department of Biotechnology and Food Science at the Norwegian University of Science and Technology (NTNU) as a final part of the Integrated Master's Degree Program in Biotechnology. The work for this thesis was carried out between January 2017 and June 2018, where 7 weeks of the period was used at Université de Toulouse, INSA, in Toulouse, France. I would like to thank my supervisor Marit Sletmoen for the guidance and support I have received through the work on my thesis.

For my stay in Toulouse, I would like to thank Mickaël Castelain from Laboratoire d'Ingénierie des Systèmes Biologiques et des Procédés (LISBP) for providing the equipment for the shear stress flow chamber, as well as the guidance and support I received during my stay. A thanks also goes to Hélène Martin-Yken and Marion Schiavone for helpful discussions regarding the interaction between fumonisin B1 and *S. cerevisiae* cells.

I wish to thank the staff of NTNU Nanolab for all the help and advice during my work in the clean room. A thanks also goes to Gjertrud Maurstad and Nina Bjørk Arnfinnsdottir, Department of Physics, for providing AFM images of my samples.

A thanks goes to Kertu Liis Krigul, Karen Dunker, Retina Shresta, Ida Monshaugen and Sylvi Oliva Kjær for the company in the lab, which helped keep my mood up during the experimental challenges I faced during the work with this thesis. A special thanks goes to my parents and my boyfriend, Einar Agdestein, for their support and encouragement. Einar's contribution as technical support in Latex has been greatly appreciated, and I am grateful for your patience regarding my constant questions. I would also like to thank my fellow students for their company during our breaks from working with the master thesis. A thanks also goes to those not already mentioned, who has contributed to the work of this master thesis.

Trondheim, 2018-06-05

Lilli Theres Eilertsen Bay

Abstract

Cells of *Saccharomyces cerevisiae* poses a possible detoxification method for the removal of mycotoxins through the formation of a yeast-mycotoxin complex. One of the main fungal genus that produces mycotoxins is the *Fusarium*, where fumonisin B1 is considered to be the most toxic. Fumonisin B1 is a carcinogen, predominantly found in maize- and maize based animal feeds. This study aims to characterize the ability of *S. cerevisiae* to interact with fumonisin B1, as well as to elaborate on the molecular mechanism involved in the yeast-fumonisin B1 complex formation.

The adhesiveness of *S. cerevisiae* was investigated using optical tweezers and shear stress flow chamber. The optical tweezers enables measurement of forces in the range of 0.1-200 pN, while the simple setup of the flow chamber offers measurements within a widely applicable force range. It was discovered that viable BY4741 and mutant Δmnn9 cells of *S. cerevisiae* were not able to interact with fumonisin B1. The outer mannan-layer of the cell wall was concluded to not participate in an interaction with fumonisin B1. Furthermore, reducing the mannan-layer did not improve the adhesiveness and it was thus considered to not limit the access to the adsorption sites. An interaction frequency of 16% was recorded between β-glucan and fumonisin B1, in which the structure of β-glucan was considered to affect the ability to interact with the mycotoxin molecules. Heat treated BY4741 cells presented an improved adhesiveness, where the treatment was assumed to alter the cell wall structure which promoted the availability of the adsorption sites. The lack of a negative control is at present a limitation that that entails challenges related to verification of the reliability of the obtained results.

Investigating cellular adhesion at the single cell level is important for detecting cell heterogeneity. This focus on detecting cell heterogeneity has lead to the development of new methods for single cell analysis, such as microcontact printing. Another objective of this thesis was to investigate the use of microcontact printing in order to produce a microoarray of *S. cerevisiae* cells on a PLL patterned glass surface. A PDMS stamp with micrometer scale features was successfully fabricated and used to deposit a pattern of fluorescent PLL onto a glass slide. However, within the limited time period available, *S. cerevisiae* was not successfully immobilized on a PLL-functionalized surface.

Sammendrag

Saccharomyces cerevisiae utgjør en mulig avgiftningsmetode for å fjerne mykotoksiner, via dannelsen av et gjær-mykotoksin kompleks. *Fusarium* er en av de viktigste sopp slektene som evner å produsere mykotoksiner, hvor fumonisin B1 regnes som en av de giftigste mykotoksinene produsert av denne slekten. Dette kreftfremkallende giftstoffet finnes hovedsakelig i mais og maisbasert dyrefôr. Målet med denne masteroppgaven er å karakterisere evnen *S. cerevisiae* har til å interagere med fumonisin B1, samt utdype den molekylære mekanismen som ligger til grunne for dannelsen av gjær-fumonisin B1 komplekset.

Interaksjonsevnen til *S. cerevisiae* og fumonisin B1 ble undersøkt ved bruk av en optisk pinsett og et strømningskammer, hvor cellene i sistnevnte utsettes for skjærspenning. Den optiske pinsetten kan detektere krefter i området 0.1-200 pN, mens strømningskammeret tilbyr målinger innenfor et bredt anvendelig kraftområde. Det ble observert at levedyktige BY4741 og mutant Δmnn9 celler ikke var i stand til å interagere med fumonisin B1. Det ytre mannan laget i celleveggen viste ikke evnen til å interagere med fumonisin B1. Samtidig viste heller ikke dette laget å begrense tilgangen til bindingssetene, da et redusert nivå av mannan ikke forbedret interaksjonsevnen. β-Glukan presenterte en interaksjonsfrekvens på 16 %, og det ble indikert at strukturen til β-glukan kjedene kan påvirke evnen til å interagere med fumonisin B1 molekylene. Varmebehandlede BY4741 celler demonstrerte en forbedret interaksjonsevne. Det ble antatt at varmebehandlingen medførte en endring i celleveggstrukturen, som promoterte tilgjengeligheten til bindingssetene. Mangelen på en negativ kontroll utgjør for øyeblikket en begrensning som innebærer utfordringer relatert til verifiseringen av resultatene.

Undersøkelser av celleadhesjon på enkeltcellenivå er viktig for å detektere cellulær heterogenitet. Fokuset på cellulær heterogenitet har medført en utvikling av nye metoder innen enkeltcelle analyse, slik som μCP. Et av objektivene ved denne masteroppgaven var å undersøke bruken av μCP for å produsere en mikromatrise av *S. cerevisiae* celler på en PLL-mønsteret glassoverflate. ET PDMS stempel med mønster på mikrometer skalaen ble brukt til å deponere et mønster av fluorescerende PLL på en glassoverflate. Innenfor den begrensende tidsperioden ble det ikke oppnådd en vellykket immobilisering av *S. cerevisiae* på en PLL-funksjonaliser overflate.

Contents

Preface i
Abstract iii
Sammendrag v
List of tables xiii
List of figures xv

1 Introduction **1**

2 Background **3**

2.1 Fumonisin 3
2.1.1 Available detoxification techniques 4
2.1.2 Microorganisms as mycotoxin adsorbents 6
2.2 *Saccharomyces cerevisiae* 6
2.2.1 Properties of the cell wall 6
2.2.2 Cell wall stress 11
2.3 Cellular adhesion at the single cell level 11
2.4 Aims of the thesis 12

3 Theory of applied methods **15**

3.1 Microscopy 15
3.1.1 Light Microscopy 15
3.1.2 Fluorescence microscopy 17
3.1.3 Phase contrast microscopy 18
3.1.4 Atomic Force Microscopy 20

3.2 Optical Tweezers . . . 21
3.2.1 Requirements of trapped objects . . . 22
3.2.2 The principle of optical trapping . . . 22
3.2.3 Principles behind force measurements . . . 23
3.3 Dynamic force spectroscopy . . . 27
3.3.1 Rupture force of single interacting pairs . . . 28
3.3.2 Probing the energy landscape of binding objects . . . 28
3.4 Shear stress flow chamber . . . 30
3.5 Chemical modification of biopolymers by reducing end modification . . . 31
3.6 Soft Lithography . . . 32
3.6.1 Fabrication of mold by photolithography . . . 33
3.6.2 Replica molding . . . 34
3.6.3 PDMS . . . 35
3.6.4 μCP . . . 36
3.6.5 Microarray of cells . . . 37

4 Materials and methods **41**
4.1 Chemicals used in the experiments . . . 41
4.2 *S. cerevisiae* cells . . . 42
4.2.1 Cultivation of *S. cerevisiae* . . . 42
4.2.2 Protease treatment of *S. cerevisiae* cells . . . 43
4.2.3 Heat treatment of *S. cerevisiae* cells . . . 43
4.3 Covalent immobilization of fumonisin B1 and yeast cell wall components onto polystyrene beads or glass surfaces . . . 44
4.3.1 Functionalization of polystyrene beads . . . 44
4.3.2 Coating of glass slides . . . 45
4.4 Quantification of interactions by the use of optical tweezers . . . 47
4.4.1 Instrument set up of JPK optical tweezers . . . 47
4.4.2 Preparation of sample chamber . . . 48
4.4.3 Force measurements using the optical tweezers . . . 49

4.4.4 Data analysis . . . 51
4.5 Preparation of samples for AFM imaging . . . 54
4.6 Shear stress flow chamber experiments . . . 54
4.6.1 Assembly of flow cell . . . 54
4.6.2 Procedure for shear-stress flow chamber experiments . . . 55
4.6.3 Cleaning procedure of coupons . . . 57
4.6.4 Data analysis . . . 58
4.7 Preparation of microarray of yeast cells . . . 58
4.7.1 Fabrication of PDMS stamp . . . 58
4.7.2 Microcontact printing . . . 60

5 Presentation and evaluation of results **65**
5.1 Quantification of interactions between *S. cerevisiae* and fumonisin B1 by the use of shear stress flow chamber . . . 65
5.1.1 Sensitivity of the shear stress flow chamber measurements . . . 67
5.1.2 AFM height images of fumonisin B1 coated glass . . . 70
5.2 Quantification of interactions between *S. cerevisiae* and fumonisin B1 by the use of optical tweezers . . . 73
5.2.1 Interaction capacity of different strains of *S. cerevisiae* and the effect of treatments affecting the cell wall structure . . . 73
5.2.2 Interactions between the cell wall components of *S. cerevisiae* and fumonisin B1 . . . 82
5.3 Force measurements by the use of optical tweezers . . . 92
5.4 Challenges associated with the optical tweezers . . . 92
5.4.1 Identifying specific interactions . . . 92
5.4.2 Factors able to affect the frequency of interactions . . . 95
5.4.3 Impurities in the sample . . . 98
5.5 Microarray of *S. cerevisiae* cells . . . 99
5.5.1 Microcontact printing of PLL-FITC . . . 99
5.5.2 Microcontact printing of PLL . . . 101

5.5.3 Immobilization of *S. cerevisiae* cells on PLL pattern 102

6 Comprehensive discussion of the information provided by the experimental work 109

6.1 *S. cerevisiae* as an adsorbing agent of fumonisin B1 109

6.2 Interaction between *S. cerevisiae* cells and fumonisin B1 109

6.2.1 Identifying the *S. cerevisiae* cell wall component involved in the interaction with fumonisin B1 110

6.2.2 Improved adhesiveness of *S. cerevisiae* cells upon heat treatment 112

6.2.3 Evaluating the specificity of the recorded interactions 113

6.2.4 The effect of the choice of functional group used for immobilization of fumonisin B1 116

6.3 Quantification of interactions by shear stress flow chamber and optical tweezers . 116

6.3.1 Establishing a good negative control 117

6.3.2 Importance of the density and homogeneity of the surface functionalization 118

6.4 Microarray of *S. cerevisiae* on PLL patterned glass surface 119

6.4.1 Microcontact printing of PLL 120

6.4.2 Adsorption of *S. cerevisiae* on a clean glass surface 120

6.4.3 Immobilization of *S. cerevisiae* on PLL-treated surface 120

7 Recommendations for further work 123

7.1 Further investigation required in order to apply *S. cerevisiae* as an adsorbing agent 123

7.1.1 Further investigation of the effect of heat treatment 123

7.1.2 Investigate the role of the functional groups on fumonisin B1 in the formation of a yeast-mycotoxin complex 123

7.1.3 Identify the optimal structure of the polysaccharide chains 124

7.1.4 Alternative techniques for investigating the adhesiveness 124

7.1.5 Other applications of the investigated cellular adhesion 125

7.2 Further work for obtaining a microarray of cells 125

8 Conclusion 127

Bibliography 129

Appendices **I**

A Acronyms **II**

B Preparation of solutions **III**

C Percentage of interaction for optical tweezers experiments **IV**

D Data analysis of flow chamber experiments **V**

D.1 Calculations of parameters for analysis V

List of Tables

4.1 Composition of cell wall in different *S. cerevisiae* strains 42

5.1 Shear stress calculated in the shear stress flow chamber for viable and heat treated WT cells attached to FB1 coated glass 66

5.2 Surface roughness of AFM height images of FB1 adsorbed or covalently immobilized on glass 72

5.3 The ability of *S. cerevisiae* cells to interact with FB1 74

5.4 Overview of the ability of the cell wall components of *S. cerevisiae* to interact with FB1 92

C.1 A summary of all experiments performed with the optical tweezers, presenting the percentage of interaction observed for each of the examined interacting pairs. . . . IV

List of Figures

2.1 Structure of fumonisin B1 4
2.2 Mechanism of action of fumonisin 5
2.3 Structure of the *Saccharomyces cerevisiae* cell wall 7
2.4 Conformation and chemical structure of β-glucan 8
2.5 Structure of N-linked and O-linked mannan in *S. cerevisiae* 10
2.6 Chemical structure chitin 10

3.1 Working principle of a light microscope 15
3.2 Working principle of fluorescence microscopy 18
3.3 Working principle of phase contrast microscopy 19
3.4 Working principle of atomic force microscopy 21
3.5 Schematic illustration of the principle of back-focal-plane interferometry. 25
3.6 Screen print of the calibration procedure implemented in the NanoTracker software 27
3.7 Reaction of reductive amination 31
3.8 Structure of α-picoline borane 32
3.9 Demonstration of the photolithography sequence 34
3.10 Structure of a poly(dimethylsiloxane) unit 36
3.11 Structure of PEG 38
3.12 Schematic illustration of the conformation of PLL-g-PEG on glass surface in aqueous solution. 39
3.13 Structure of PLL monomer 39

4.1 Working principle of the coupling agent EDC 44

4.2 Chemical structure of N-((3-Trimethoxysilyl)-propyl)ethylenedamine triacetic acid trisodium salt. 46
4.3 Schematic diagram of the JPK NanoTracker Optical Tweezers 48
4.4 Assembly of liquid cell 49
4.5 A schematic drawing of optical traps with two trapped beads. 50
4.6 Screen print of interaction analysis in the iNanoTrackerOT3DPostProcess program 53
4.7 Assembly of flow cell 56
4.8 Schematic diagram for setup of shear stress experiments 57
4.9 Fabrication procedure of a PDMS stamp 59
4.10 Schematic overview of the microcontact procedure for obtaining a microarray of *S. cerevisiae* cells. 63

5.1 Percentage of detachment under shear flow for heat treated WT cells 66
5.2 Number of cells present on the coupon before and after rinsing 67
5.3 Demonstration of uneven coverage of FB1 on the coupon surface 70
5.4 AFM height images of FB1 adsorbed or covalently immobilized on glass 71
5.5 Marked region of AFM height image for determination of surface roughness 72
5.6 Frequency of interaction for heat treated WT yeast cells and FB1 on either NH_2- or COOH-beads, as well as the corresponding controls 75
5.7 Examples of force curves for heat treated WT cells vs. FB1-coated or uncoated COOH-beads 76
5.8 Unbinding forces between heat treated WT yeast cells and FB1 on COOH-beads . 77
5.9 Comparison of the dynamic power spectra of heat treated WT yeast cells - FB1 on COOH-beads, and heat treated cells - untreated COOH-beads 78
5.10 Examples of force curves for heat treated WT cells vs. FB1-coated or uncoated NH_2 beads 79
5.11 Distribution of unbinding forces between heat treated WT yeast cells and FB1 on NH_2-beads 80
5.12 Comparison of the dynamic power spectra of heat treated WT yeast cells - FB1 on NH_2-beads, and heat treated cells - untreated NH_2-beads 81

5.13 Comparison of the dynamic power spectra for the interactions between heat treated WT *S. cerevisiae* cells and FB1 on either NH_2- or COOH-beads 82
5.14 Frequency of interactions for the cell wall components of *S. cerevisiae* with FB1, and the corresponding controls. 83
5.15 Examples of force curves for β-glucan vs. FB1-coated or uncoated COOH-beads . 84
5.16 Unbinding forces between the cell wall component β-glucan and FB1 on COOH-beads 85
5.17 Comparison of the dynamic power spectra of β-glucan - FB1 on COOH-beads, and β-glucan - untreated COOH-beads 86
5.18 Examples of force curves for β-glucan vs. FB1-coated or uncoated NH_2 beads . . . 87
5.19 Unbinding forces between β-glucan and FB1 on NH_2-beads 88
5.20 Comparison of the dynamic power spectra of β-glucan - FB1 on NH_2-beads, and β-glucan - untreated NH_2-beads 89
5.21 Examples of force curves obtained for the self-interaction of NH2-beads 89
5.22 Dynamic power spectrum for β-glucan - FB1 compared with the spectrum for interactions between untreated NH_2-beads 90
5.23 Comparison of the dynamic spectra for the interactions between β-glucan and FB1 on either NH_2- or COOH-beads 91
5.24 Demonstration of force curve with good estimation of loading rate 93
5.25 Demonstration of force curve with multiple bond ruptures 94
5.26 Demonstration of force curves with inaccurate estimation of loading rate 95
5.27 μCP of PLL-FITC on glass slide 100
5.28 Demonstration of failed deposition of PLL-FITC pattern on glass slide 101
5.29 μCP of PLL on glass slide 102
5.30 Immobilization of *S. cerevisiae* on PLL patterned glass slide 103
5.31 *S. cerevisiae* immobilized on cleaned cover glass 105
5.32 *S. cerevisiae* immobilized on pegylayed glass slide 106
5.33 Immobilization of *S. cerevisiae* on pegylated glass slide functionalized with PLL . . 107
5.34 Uneven coverage of *S. cerevisiae* cells on PLL functionalized glass slides 107

D.1 Demonstration of custom made excel sheet for recording weight of run through buffer and number of cells for the flow chamber assay VII

1. Introduction

Annually, a high percentage of the world's crops are contaminated by toxic compounds produced by fungi [1]. These mycotoxins poses a threat to both animals and humans by introducing diseases through contaminated food and feed [2]. A variety of physical and chemical methods have been suggested for detoxification of mycotoxins. However, many of these techniques present challenges that prevent their acceptance for practical use [1]. As a result, microorganisms able to bind mycotoxins in a solution have been suggested as a possible detoxification technique. Several bacterial and yeast strains have been investigated, which have revealed the ability of *Saccharomyces cerevisiae* to form complexes with a variety of mycotoxins [3]. The formation of such microorganism-mycotoxin complexes in the gastrointestinal tract can prevent adsorption of the mycotoxins into the blood stream. Hence, the development of toxin-induced diseases is hindered [4]. However, before these adsorbing agents can be applied *in vivo*, further information is required on the underlying molecular mechanism of this physical adsorption.

The complex nature of cells can cause a considerable difference in their adhesion ability. This cell heterogeneity is hidden during bulk experiments, and thus require adhesion analysis at the single cell level. The adhesiveness of cells is generally quantified based on their ability to remain attached to a surface upon the exposure of a detachment force. There are several techniques available today for investigation cellular adhesion, such as atomic force spectroscopy, optical tweezers and flow chamber assay [5]. However, new possibilities have emerged related to the growing field on nanobiotechnology. Microcontact printing enables patterning of surfaces to facilitate cell adhesion. Such isolation of cells allows high throughput study of single cell events, or the study of interactions between pairs and triplets of cells [6].

2. Background

2.1 Fumonisin

Mycotoxins are secondary metabolites of fungi that can be harmful for both animals and humans, by introducing diseases known as mycotoxicosis. One of the main fungal genus able to produce mycotoxins is the *Fusarium*, which is responsible for the production of zearalenone, trichothecenes and fumonisin [2]. In this thesis, the mycotoxin fumonisin will be further elaborated, as well as the challenges related to the detoxification techniques applied today.

Fumonisins are mainly produced by *Fusarium proliferatum* and *F. verticillioides* (formerly known as *F. moniliforme*). The different *Fusarium* species are located all over the world [7], but thrives mostly in temperate regions where they are widely distributed in soil or associated with plants [8]. Highest occurrence of fumonisins have been recorded in maize and maize-based animal feeds [7, 9, 10]. Animal studies have presented fumonisins as hepatoxic, nephotoxic, atherogenic, immunosuppressive and embryotoxic [11]. Several different types of fumonisins have been identified. The most important ones are fumonisin B1 (FB1) and fumonisin B2 (FB2), where FB1 seems more abundant than FB2. Together they constitute approximately 70% of the fumonisins recorded in naturally contaminated food. Both present phytotoxicity to various weeds and crop cultivate, as well as cytotoxicity to different mammalian cell lines. In addition, studies using rats as a model organism have documented that FB1 is carcinogenic to liver and kidney [9]. FB1 is the most toxic of the fumonisins, and is considered to be a human carcinogen of class 2B [10]. It is also responsible for the two well-identified diseases in domestic animals; equine leukoncephalomalacia in horses and pulmonary edema syndrome in swine [8, 9].

Fumonisins are alkylamines with a long hydroxylated chain and further esterified with two propanetricarboxylic acid moieties on adjacent carbons (figure 2.1). The different types of fumonisins are classified into A and B series, where the fumonisins are N-acetylated or contain free amino groups, respectively. The propanetricarboxylic acid moieties of fumonisins B1 and B2 can be hydrolytically removed, resulting in the formation of the respective aminopentols AP1

and AP2 [8]. The free amino group seems to enhance their activity. This assumption is based on N-acetylated fumonisins not presenting any detectable toxicity [9]. The role of the aminopentols in the toxic mechanism of fumonisins, as well as the enzymes responsible for the formation of these aminopentols, needs further investigation. These enzymes are widely present in both plant and animal tissues, and are primary located i liver, kidney, duodenum and brain in mammalian systems. If these enzymes are required in order to activate the fumonisins, then this can be an explaining factor for the observed variety in sensitivity of different cell lines and organs to the toxin [8].

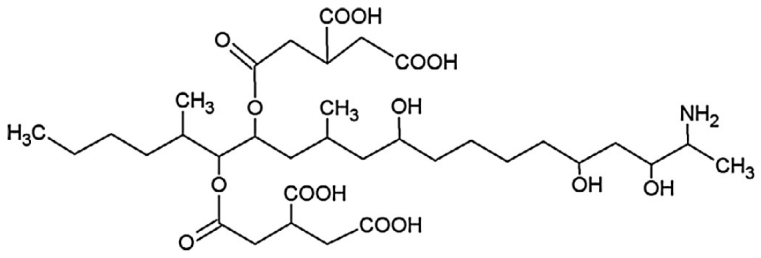

Figure 2.1: Structure of fumonisin B1. Figure reproduced from Marin *et al.* (2013) [2].

The mechanism of action of fumonisins involves the inhibition of the enzyme ceramide synthase, which is responsible for the acylation of sphinganine (Sa) and sphingosine (So) (figure 2.2). Fumonisins, and especially FB1, resemble the structure of Sa and So, rendering it able to interact with ceramide synthase. Consequently, the level of these cytotoxic sphingoid bases increases and the sphingolipid metabolism is disrupted [7, 10, 11]. Being important structural components of the cell membrane, as well as participating in transduction pathways as secondary messenger, sphingolipids are essential in maintaining normal regulatory mechanisms within cells. The effects of fumonisin, documented for animal and human systems *in vitro*, involve regenerative cell proliferation and apoptosis, as a consequence of disrupted sphingolipid metabolism [10]. The accumulation of free sphingoid bases also leads to proapoptotic and growth inhibitory effects, contributing to the toxic and carcinogenic effects of fumonisin [7].

2.1.1 Available detoxification techniques

The presence of fumonisin in food products can be avoided either by preventing their formation, or by eliminating or inactivating already present fumonisin. Avoiding mycotoxin contam-

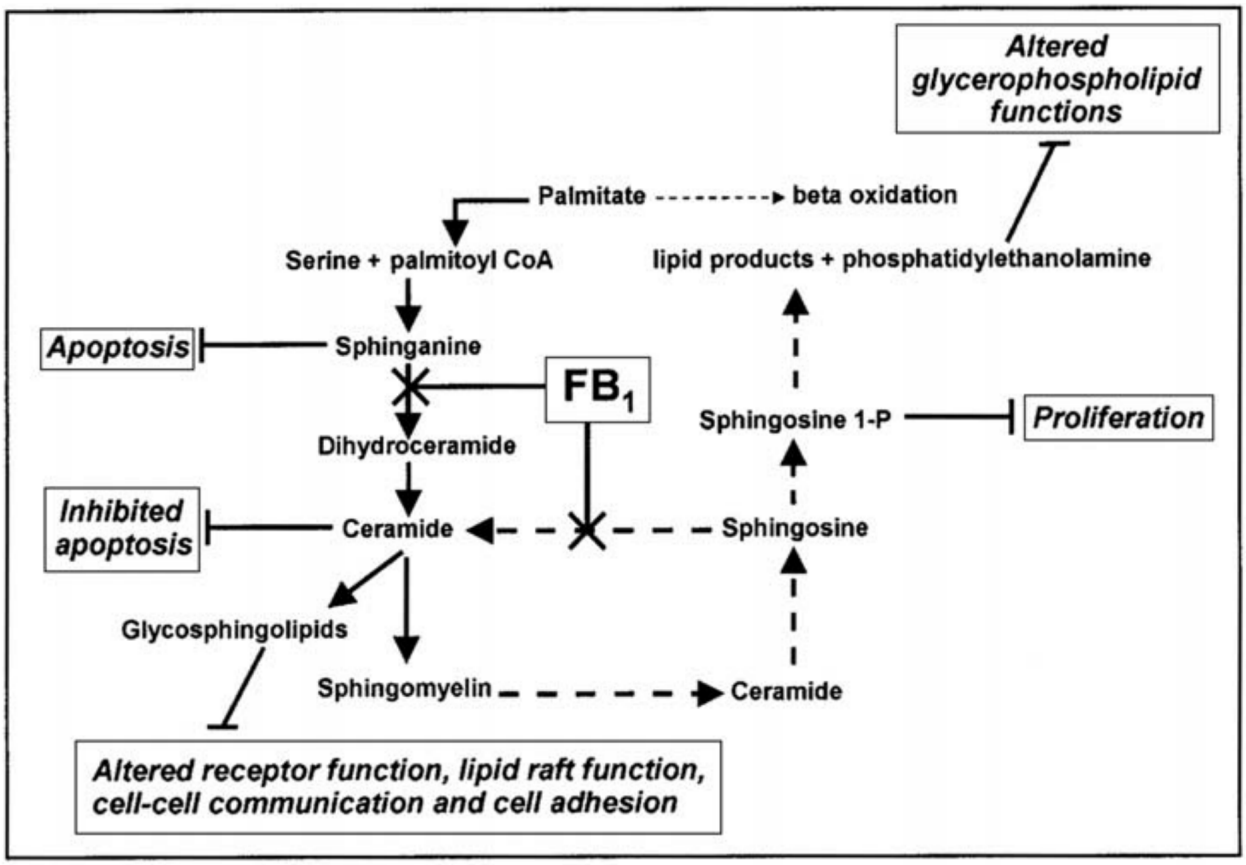

Figure 2.2: The pathways of sphingolipid biosynthesis, and the biological activities affected by fumonisin B1 (FB1). FB1 inhibit the ceramide synthase, resulting in the disruption of sphingolipid metabolism. Figure reproduced from IARC Monographs (2002) [10].

ination can be achieved by inhibiting the growth of molds through the application of well-selected harvesting, storage and processing methods. However, if mycotoxins are already present on the field, correct storage or the use of mold inhibitors will not influence the presence of the mycotoxins. The detoxification techniques available today include both physical and chemical methods. However, they are not widely used due to their high cost, complex procedure and the possible consequence of reducing nutritional and sensory properties of the food products. Furthermore, some detoxification techniques result in even more toxic by-products. The physical methods include radiation, ultrasound, washing procedures and direct removal of the contaminated section of the crop [1]. Some of the inorganic compounds proven effective against mycotoxins, include clays, bentonites and aluminosilicates. Despite these promising results, these inorganic compounds are not specific adsorbents, resulting in inefficient adsorption of some mycotoxins, as well as the possibility of adsorbing essential nutrients. As a result, organic com-

pounds, such as yeast or bacterial cell walls have been investigated for their adhesiveness of mycotoxins [3].

2.1.2 Microorganisms as mycotoxin adsorbents

Several yeast and bacterial strains has proven the ability of reversibly adsorbing mycotoxins in a suspension. One promising sequestering agent is *Saccharomyces cerevisiae*, which have presented the ability to form complexes with several mycotoxins, including fumonisin B1. The cell wall components are assumed to be responsible for the interactions, however, the molecular mechanism behind the microorganism-mycotoxin complex is still not completely established [3, 4, 12–14].

2.2 *Saccharomyces cerevisiae*

The yeast *Saccharomyces cerevisiae* is of the phylum Ascomycetes [15]. This facultative anaerobe fungus plays an important role in brewing and bakery, while also being a well known model organism. In 1994, *S. cerevisiae* became the first eukaryote to have its full genome sequenced [16].

S. cerevisiae is capable of both asexual and sexual reproduction, and can therefore exists both as haploid or diploid cells. By asexual reproduction, a new cell is formed by budding cell division of the zygote. Upon separation of daughter cell from the mother cell, both cells are marked with a scar at the point of separation. Sexual reproduction is based upon the event were two cells of different mating type fuse. During conditions of starvation, the formed zygote will further initiate meiosis, which eventually leads to the formation of haploid ascospores. One cycle produces four haploid cells, two of each mating type. A single cell of *S. cerevisiae* has a diameter of approximately 6 µm, and has a spherical, oval or cylindrical shape [16].

2.2.1 Properties of the cell wall

Constituting 15-30% of the total weight of a cell, the cell wall of *S. cerevisiae* determines the shape of the cell and offers protection from both osmotic and physical factors. The bi-layered

structure is composed of β-glucan, mannan, chitin, phosphate, lipids and many different proteins. [17, 18]. All these components are cross-linked in different ways to produce high-order complexes. The relative amount and location of the individual cell wall components are highly dependent on the developmental stage and growth phase of the cell, as well as external factors. This includes nutritional conditions and stress imposed by drug treatment, hypo-osmolarity or mutational loss of wall biosynthetic activities or wall proteins [18].

The inner layer, consisting of glucan polymers and chitin, offer mechanical strength and acts as a scaffold for the outer protective layer of mannan and mannoproteins. 80-90% of this inner layer is constructed of β-1,3-linked glucan chains, which are branched through β-1,6-linkages [19, 20]. A schematic presentation of the structure of the *S. cerevisiae* cell wall is shown in figure 2.3.

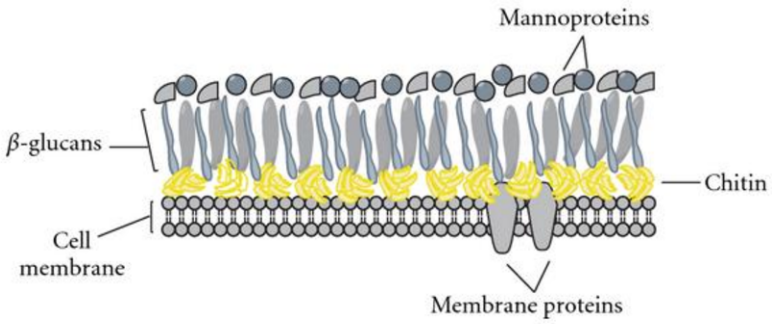

Figure 2.3: Structure of the *Saccharomyces cerevisiae* cell wall. The β-glucan contains both β-1,3- and β-1,6-linked glucan. Figure reproduced from Vega *et al.* (2012) [21].

β-Glucan

The polysaccharide chains of β-glucan consist of a backbone of D-glucose sugar units, assembled through β-1,3-glycosidic linkages. The helical nature of the β-1,3-linked glucan chains is primarily responsible for the elasticity of the cell wall (figure 2.4). Furthermore, the β-1,3-linked glucan chains contain β-1,6-linked side chain [22]. The presence of these side chains results in local association of the β-1,3-linked glucan molecules through hydrogen bonds, which create a continuous and elastic, three-dimensional network. The β-1,6-linked glucan and β-1,3-linked glucan constitutes 5-10% and 30-45% of the cell wall, respectively. Although the β-1,6-linked glucan constitutes a minor component of the wall, they play a central role in cross-linking cell

wall components [18, 23].

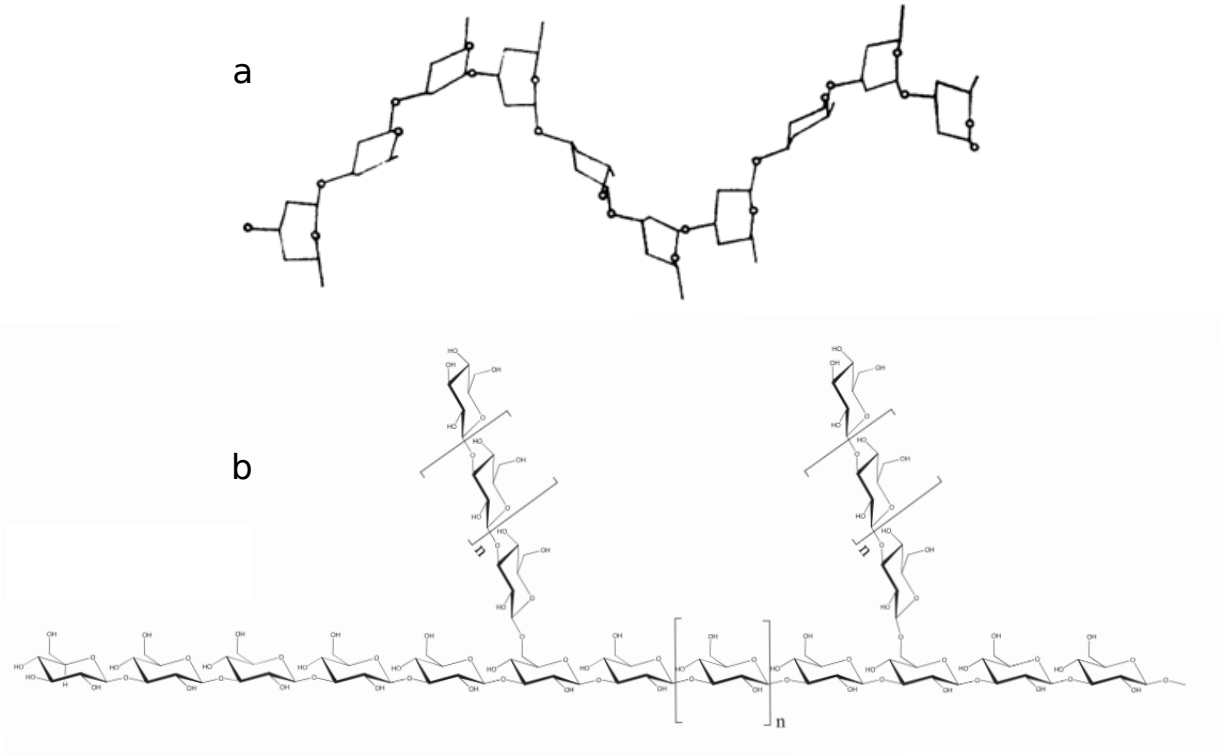

Figure 2.4: (a) Helical conformation of the β-1,3-linked glucan chain. Figure reproduced from Rees *et al.* (1971) [22]. (b) Chemical structure of β-1,3-linked glucan with β-1,6-linked side chains. Figure reproduced from Samuelsen *et al.* (2014) [24].

The non-reducing ends of β-1,3-linked glucan chains can function as attachment sites for other polysaccharides in the cell wall. For instance, chitin chains can attach to the non-reducing ends of the β-1,3-linked glucan network in the lateral walls [23]. In response to cell wall stress, chitin can also become glycosidically linked to the non-reducing ends of the β-1,6-linked glucan chains [20]. The cross-linking of β-glucan to chitin results in insolubility in alkali-solutions [18]. Furthermore, these highly branched and water soluble β-1,6-linked glucan chains are also able to attach to glycosylphosphatidylinositol (GPI)-modified mannoproteins at the external face of the β-1,3-glucan network [23].

Mannan and mannoproteins

The mannoproteins that constitutes the outer layer of the cell wall have a protein moiety of about 100 kDa in apparent size [25]. The two main classes of cell wall proteins (CWPs) are GPI-

dependent cell wall proteins (GPI-CWPs) and Pir proteins (Pir-CWPs). The GPI-CWPs are as mentioned indirectly linked to β-1,3-linked glucan through their β-1,6-linked branches. Pir-CWPs is linked to β-1,3-linked glucan though an alkali-sensitive bond. The mannoproteins are heavily glycosylated with a mannan fraction that can exceed 90%. These heavily glycosylated mannoproteins play an important role in cell-cell recognition, as well as shielding the inner part of the cell wall from foreign enzymes [20].

The mannan polymer, constituting 30-50% of the cell wall, consists of mannose sugar units in a α-1,6-linked backbone, with α-1,2- and α-1,3-linked branches [23, 26]. The phoshodiester bridges in both N- and O-linked mannosyl side chains result in the cell surface having numerous negative charges. The large N-linked mannans chains are heavily branched and linked to asparagine residues of a mannoprotein. The presence of these long and branched carbohydrate side chains, as well as the presence of disulfide bridges, makes the outer layer less permeable compared to the internal fibrous layer. The O-linked mannans consists of shorter chains, approximately five mannose residues, that are attached to serine or threonine residues of a protein [20]. The structure of N-linked and O-linked mannan is illustrated in figure 2.5.

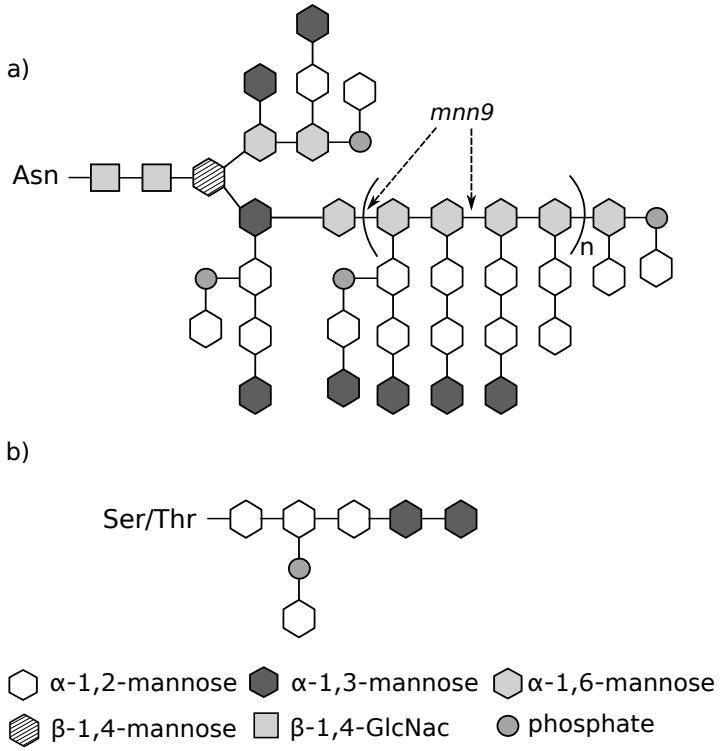

Figure 2.5: Structure of (a) N-linked and (b) O-linked mannan in *Saccharomyces cerevisiae.* Asn, asparagine; Ser, serine; Thr, threonine; GlcNAc, N-acetylglucosamine. Figure modified from Jigami *et al.* (1999) [27] and Hirayama *et al.* (2012) [28].

Chitin

Chitin is a linear polysaccharide composed of repeating β-1,4-linked N-acetylglucosamine (GlcNAc) monomers (figure 2.6), which contributes no more than 1-2% of the dry weight of the wall. As mentioned, this polymer is located in the innermost layer of the wall, as well as deposited in a ring between the emerging bud and the mother cell, in the primary septum and in bud scars [18, 20]. Chitin is present in three polydisperse forms in the wall: free chains, bound to β-1,3-linked glucan at the neck between mother and bud, and bound to β-1,6-linked glucan at the lateral walls. As a response to cell wall stress, the amount of chitin in the lateral walls can increase up to 20% of the wall [18].

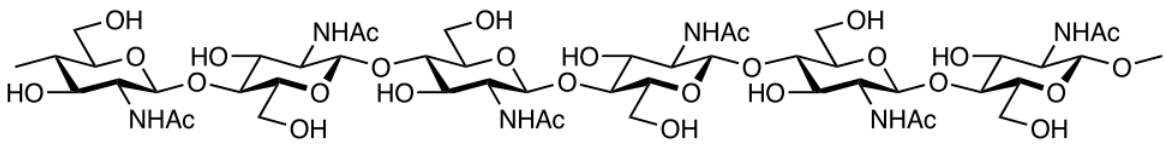

Figure 2.6: Chemical structure of chitin. Figure reproduced from Kurita *et al.* (2006) [29].

2.2.2 Cell wall stress

S. cerevisiae, as many other microorganisms, has developed a defense mechanism in order to survive under adverse conditions. The cells sense and respond to the environment via signaling pathways, and initiate an appropriate cellular response upon environmental changes [30, 31]. A variety of environmental conditions are able to initiate an stress response, including pH, high salt level, osmotic stress, oxidative stress, cell wall stress, high temperature, or stress caused by antifungal compounds. The integrity of the cell is largely depended on the cell wall, which offers mechanical strength that allows the cell to support turgor pressure against the plasma membrane [19, 30]. Maintaining the mechanical strength of the cell wall is thus necessary for survival, and such stress-induced changes in the cell wall structure initiate a cellular response referred to as the "compensatory mechanism". This cellular response results in increased levels of chitin and changed association between β-glucan, mannoproteins and chitin [23, 32, 33]. The expression of several cell wall proteins is also increased, such as the Pir proteins, while some of the cell wall proteins are relocated from the cell wall construction machinery to the lateral wall. Furthermore, the β-1,3-glucan synthase complex is temporary redistributed throughout the cell [33, 34].

2.3 Cellular adhesion at the single cell level

Cells are complex biological systems and they behave individually, which results in a considerable difference in their adhesion ability. This cell heterogeneity is hidden during bulk experiments, and thus require adhesion analysis at the single cell level. Quantification of adhesiveness is generally based on the ability of cells to remain attached to a surface upon exposure to a detachment force. The complexity of cellular systems requires investigation of a large number of single cells, to compensate for the uncertainty regarding abnormal behaviour. Cell adhesion is generally a combination of specific and nonspecific interactions. It is therefore necessary to perform control experiments, in order to identify specific adhesive interaction from the many possible non-specific interactions [5].

Several techniques are available today for analysis of single cells. To identify each adhesive feature of a cell, techniques such as optical tweezers and flow chamber have been applied. In

the latter method, cells are exerted to shear stress by a homogeneous buffer. The adhesiveness is indicated by the number of remaining cells as the shear stress is increased. The optical tweezers enables trapping of nano- or micrometer-sized objects by a focused laser beam. Interactions are measured by pulling two trapped objects apart, where the detachment force is recorded in the range of 0.1-200 pN [5].

There is an increasing interest for developing high throughput platforms for single cell analysis [35, 36]. Techniques related to nanobiotechnology offers new possibilities for performing analysis at the single cell level [37]. Patterning of surfaces to facilitate cell adhesion has been investigated. Microcontact printing utilizes an elastomeric stamp with designed features to deposit a cell-binding chemical onto the substrate surface. This creates patches where cells are likely to attach, on an otherwise cell-repellent surface [38].

Cellular adhesion plays a major role in guiding a range of cell functions, which is important for several applications within the fields of physiology, pathology and biotechnology. A deeper understanding of the biophysical and biochemical mechanisms related to cellular adhesion can be useful for controlling the interaction of certain cells with an artificial environment for medical purposes. Furthermore, it is important for the development of cell-based regenerative therapy of human tissues, as well as optimizing the activity of cells in a bioreactor for applications in pharmacy, in addition to the food industry and materials engineering [39].

2.4 Aims of the thesis

The main objectives of this Master's project are summarized in the following aims:

- Evaluate the ability of *S. cerevisiae* to interact with the mycotoxin fumonisin B1, by the use of optical tweezers and shear stress flow chamber. The adhesiveness of the cell wall components mannan and β-glucan, as well as the wild-type BY4741 and mutant Δmnn9 strains of *S. cerevisiae* will be characterized.

- Investigate if subjecting the *S. cerevisiae* cells to a protease treatment or heat shock improves their adhesiveness towards fumonisin B1.

- Deposit PLL pattern by using microcontact printing.

- Investigate the suitability of microcontact printing using PLL and cells of *S. cerevisiae* as a method to achieve microarrays of yeast cells on glass slides.

3. Theory of applied methods

3.1 Microscopy

3.1.1 Light Microscopy

After the invention of the light microscope in the 17^{th} century it has been an important tool used by biologists. Microscopes are used to produce images of structures, and can be used to study a specimen in real time [40]. The simplest form of a light microscope is the bright field microscope. The optical system of such a microscope includes the light source, condenser lens, microscope slide containing the specimen, objective lens and oculars through which the image of the specimen is visualized (figure 3.1). The light source, which often is a halogen lamp, can be built into the base of the microscope, where light is shined directly into the condenser. The condenser acts to focus the light onto a small area of the sample. The specimen will diffract the light, which is further collected by the objective lens and converted into an image at the real intermediate image plane located close to the eyepieces or oculars (figure 3.1). The ocular lenses offer additional magnification of the image produced by the objective lenses [41].

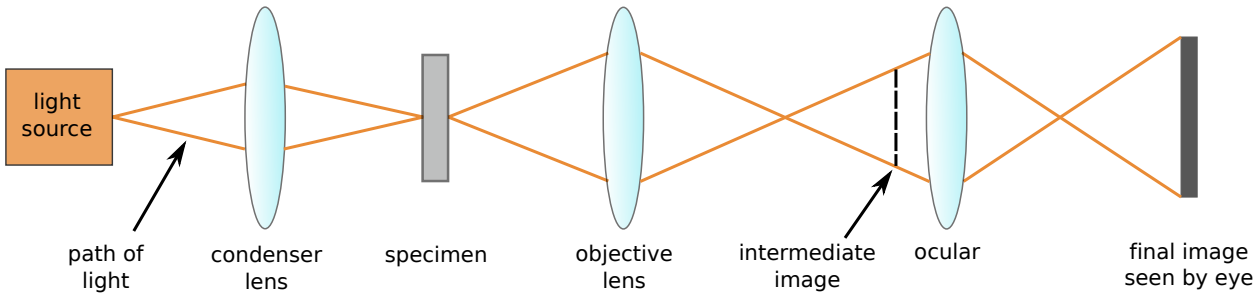

Figure 3.1: Working principle of a light microscope.

The total level of magnification is determined by multiplying the magnification of the objective lens with the magnification of the ocular. In the case of studying very small organisms or in the field of microbiology, an oil immersion objective is preferred. Such objectives have a magnification of 100x and requires a drop of oil between the slide and the objective [41].

The resolving power of a lens is the ability to distinguish between separate objects or points located close to each other. Both the numerical aperture (NA) of a lens and the wavelength of the light beam (λ) affects the resolution of a light microscope. The numerical aperture is defined by the following equation:

$$\text{NA} = n \sin \alpha \tag{3.1}$$

where n is the refractive index of the medium between the sample and objective lens, and α the maximum angle of incident light entering the objective lens [42]. The refractive index is defined as the ratio between the speed of light in a vacuum and its speed in a medium [43].

NA indicates the amount of light collected by the lens, and the highest value of NA is obtained when applying an oil immersion, resulting in a value of 1.4. To obtain maximum resolution, the NA of the condenser lens should match the NA of the objective lens. For light microscopes, the light beam is from the visible part of the spectrum, with wavelengths in the range of 0.4-0.7 µm. The resolving power of a bright field microscope, where the condenser NA ≥ the objective NA, is given by equation 3.2:

$$d = \frac{0.61\lambda}{\text{NA}} \tag{3.2}$$

where d is the minimum resolved distance and λ is the imaging wavelength [42].

Bright and even illumination of the specimen plane is achieved through Köhler illumination. The collector lens is responsible for generating an image of the light source at the front aperture of the condenser. The front aperture refers to the opening at the front focal plane of a lens, when the light travels from the lamp to the retina. The condenser lens further generates an image of the field stop diaphragm in the object. In the front focal plane of the condenser lens is the condenser diaphragm. The light source illuminates a certain area of the field stop diaphragm in the specimen. This results in limited light scattered from other areas of the object, which further contributes to the formation of an image. Light originating from the same point in the light source are able to enter the object in parallel when the front aperture of the condenser is located in the focal plane of the condenser lens. An even illumination is achieved by ensuring that each light source point will contribute equally to illumination in the specimen plane [42].

Another important aspect of the microscope is the level of contrast, which is the variation in the amount of light falling on each point of the image plane. Light absorption and scattering of light presents two sources of contrast in bright field microscopes. Bright field microscopes are suited for studying specimens with good contrast level. This includes specimens with naturally occurring pigmentation or samples where components or the whole specimen has been dyed. Dyes or pigments allows the specimen to appear in color by absorbing specific wavelengths of the white light. The contrast level of transparent biological specimens is naturally poor due to a refractive index similar to that of the glass. This can be improved by staining or by applying alternative microscopy techniques [41, 42].

3.1.2 Fluorescence microscopy

A bright field microscope can be used for fluorescence microscopy, but it requires strong attenuation of the excitation light. This can be obtained by epi-illumination, where the specimen is illuminated and the emitted light is detected from the same side, as demonstrated in figure 3.2. In order to use a bright field microscope to detect the fluorescence, a filter cube containing an excitation filter, a dichroic mirror and an emission filter, is inserted into the optical pathway (figure 3.2). The optical properties of the filter cube are designed to match the adsorption and emission wavelength range of the fluorophore, which is a chromophore that fluoresces. The dichoric mirror functions by directing the excitation light towards the specimen, as well as allowing the emitted fluorescent light to pass through. The emission filter acts to select the light in the range of wavelengths absorbed by the fluorophore [42]. A bright field microscope containing such a setup will generate an image that appears dark in areas corresponding to locations in the specimen without fluorophores, and colored in areas where there are fluorophores [40].

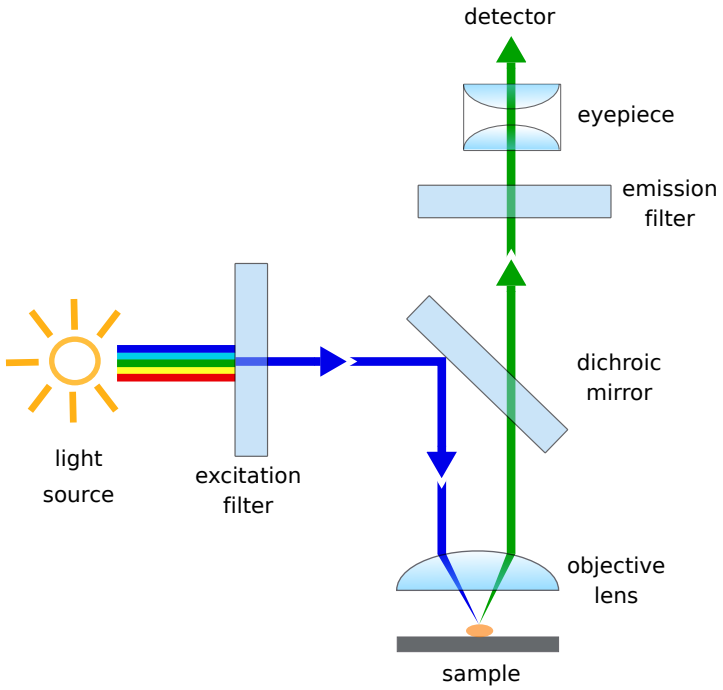

Figure 3.2: Schematic demonstration of the optical pathways in a fluorescence microscope, including the working principle of the filter cube.

3.1.3 Phase contrast microscopy

Phase objects are specimens that are not able to absorb light, but can diffract light and cause a phase shift in the light rays passing through them. This phase shift is not visible by the naked eye, but can be detected by transforming the phase shift into an intensity difference. A phase contrast microscope is able to perform such transformation, and is therefore suited for imaging of transparent biological specimens. When light passes through a phase object, the illuminating beam is separated into two components. Most of the light passes through the specimen without interacting with it, while a small portion gets scattered in many directions. Both light waves are collected by the objective lens and focused in the image plane. Due to their difference in the optical pathway, the waves undergo interference and generate a particle wave. For the microscope to detect the object image, a significant difference in the amplitude of the particle wave and the diffracted wave is required [42]. The principle of a phase contract microscope is presented in figure 3.3.

The optical design of the phase contrast microscope needs to isolate and separate the unobstructed and diffracted waves, so that they occupy different locations in the diffraction plane

at the back aperture of the objective lens. It is also necessary to obtain constructive or destructive interference, as well as reduce the amplitude of the unobstructed wave to enhance the differences in amplitude between the object and the background in the image plane. Such optical design is achieved by inserting a ring shaped aperture diaphragm and a phase plate at the back focal plane. This modulator plate is made out of glass with a partly transparent ring. The diffracted wave light is modified by $\lambda/4$ relative to the phase of the unobstructed wave. The unobstructed wave is further advanced in the positive phase contrast by $\lambda/4$ at the phase plate, resulting in a total phase shift of $\lambda/2$. This enables a destructive interference with the diffracted wave in the image plane. Specimens with a higher or lower refractive index than its surrounding medium will appear dark or bright, respectively. A negative phase contrast is achieved when the unobstructed wave is retarded by $\lambda/4$, resulting in a total phase shift of 0. This enables constructive interference with the unobstructed waves in the image plane [42].

However, relative phase advancements is not sufficient to generate a high contrast image, due to the amplitude of the unobstructed wave being too high to obtain an adequate contrast level. This can be solved by darkening the ring in the phase plate by a semitransparent metallic coating, which results in about 70% reduction in the amplitude of the unobstructed wave. Since the particle wave is a product of both the unobstructed and diffracted waves, the generated particle wave will have a considerable lower amplitude than the diffracted wave. This is due to the interference in the image plane. The difference in phase from diffraction by the sample is transformed into an observable difference in contrast, and the object can be visualized in the microscope [42].

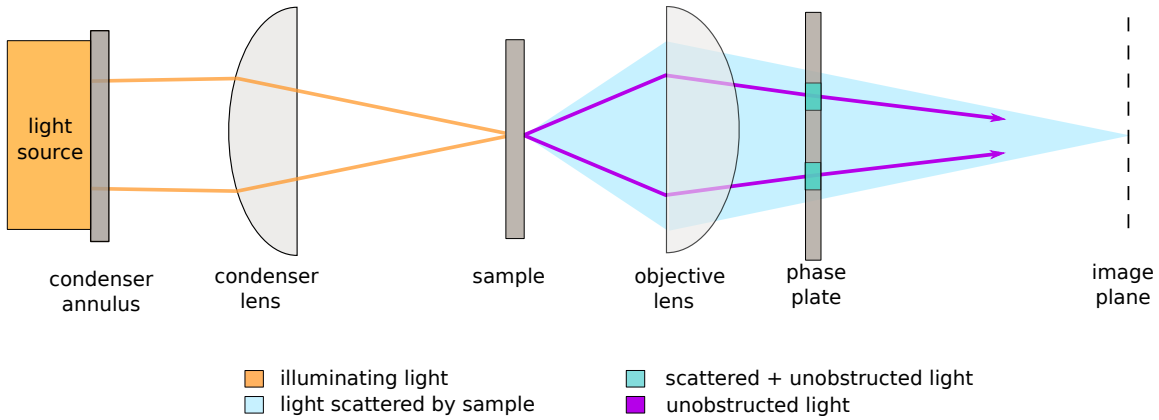

Figure 3.3: Working principle of phase contrast microscopy.

3.1.4 Atomic Force Microscopy

The atomic force microscopy (AFM) offers two modes of function: force spectroscopy and imaging. The main components of the AFM are a tip attached to a cantilever, a sample stage and an optical deflection system, which consist of a laser diode and a photodetector (figure 3.4). Images are created by scanning the sample surface with the sharp tip mounted to the soft cantilever spring. The interaction force between the tip and the sample is used to probe the topography of the surface. A laser beam, focused on the free end of the cantilever, is used to detect the deflection of the cantilever, which is directly proportional to the force [42].

The AFM is able to operate in three different modes for imaging: contact, tapping and non-contact. In the contact mode, the tip is in direct contact with the sample surface. Variation in the height of the sample results in deflection of the cantilever. A feedback loop will maintain a constant sample probe distance by adjusting the height of the sample stage. The direct contact between the tip and the sample might induce damage to the sample surface, which can be reduced by applying the tapping mode. Instead of continuously touching the surface, the cantilever oscillates over the sample and gently taps the sample surface. When the tip is close to the surface, the oscillation frequency is reduced. As with the contact mode, a feedback loop will adjust the probe height to maintain a constant amplitude. In the third mode, the tip never touches the surface, but is oscillating above the surface level. The topography is detected based on van der Waals forces. The non-contact mode requires vacuum for optimal function [42]. In this master thesis, AFM was used to investigate fumonisin B1 coated glass surfaces, and the tapping mode was utilized.

In the force spectroscopy mode, the cantilever deflection is recorded as a function of the vertical displacement of the piezoelectric scanner. The AFM can detect forces such as mechanical contact forces, chemical binding and van der Waals forces. The spectroscopy mode of AFM was not used in this thesis, and is therefore not further elaborated [42].

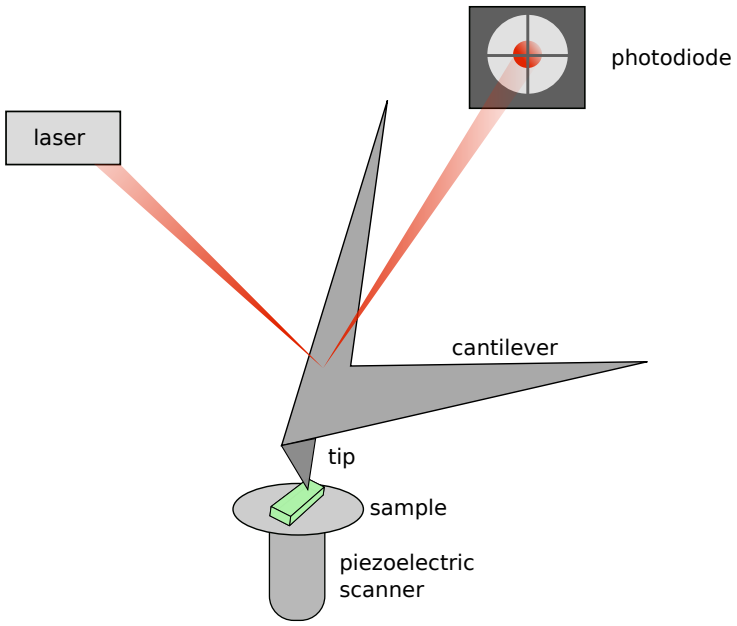

Figure 3.4: Working principle of atomic force microscopy.

3.2 Optical Tweezers

The optical tweezers (OT) were invented in the 1990s, but the first observations of optical trapping were already reported by Arthur Ashkin and coworkers at Bell Labs in 1970. He demonstrated the ability of optical forces to displace and levitate micron-sized dielectric particles, both in water and in air. This work further lead to the development of a single-beam gradient force optical trap, which is today known as the "optical tweezers". The OT utilizes a high numerical aperture microscope to focus a laser beam at a diffraction limited spot, in order to restrain micro- and nanosized objects stably in space. It can also be used to control the state of motion and trajectory of these objects. Since there is no mechanical contact with the trapped object, the OT offers the possibility of manipulate and reposition living cells and single molecules without causing them any damage. The position of the trapped object can be detected with nanometer-level precision, and in combination with the OT this enables quantitative measurements of force interactions at the piconewton (pN) level [42, 44]. The force of the optical trap is in the order of 1-100 pN, depending on the properties of the trapped object, such as size and refractive index, in addition to the wavelength of the laser beam [45].

3.2.1 Requirements of trapped objects

In order for an object to be manipulated by the OT, it has to fulfill certain requirements. Objects that are small, mostly transparent and often dielectric particles, can be trapped by the laser beam of an OT [42]. Dielectric particles, such as polystyrene beads, can be used alone or as carriers to manipulate other objects that are too small to be trapped by a laser, including biological molecules such as polymers and proteins. The polystyrene beads used in OT studies generally have sizes in the range of 10 nm to 4 µm (JPK technical note). Biological specimens, such as bacteria, yeast and organelles of larger cells, can be trapped directly. The refractive index (n) of the object is important in the sense that it needs to be higher than the refractive index of the surrounding medium [44]. The first experiments performed with an OT revealed that the focusing effect only functioned when the objects had a higher refractive index than the surrounding medium [42]. Objects with a lower refractive index than the surrounding medium will be propelled forward, in the opposite direction of the intensity gradient [44].

3.2.2 The principle of optical trapping

Optical forces depends on the relationship between the radius of the trapped sphere (a) and the wavelength of the laser (λ), as well as the relationship between the wavelength and the beam waist (w_0). Consequently, optical trapping is described in the two main regimes: Geometrical optics regime ($a \gg \lambda$) and Rayleigh regime ($a \ll \lambda/20$). In this experiment, polystyrene beads and yeast cells are used, which have sizes in the Mie regime (from 200 nm to 7 µm) [42], and therefore only the geometrical optics regime will be further explored.

The rays travelling in an optical field will follow a straight line in an uniform media. When the rays reaches an interface separating two media of different refractive indices, the direction of propagation is changed. For instance, as light impinges on one side of the polystyrene bead, some of the light is absorbed while the rest is scattered in several directions. Since light carries momentum, this corresponds to a change in the momentum of the light [42, 44]. The force exerted on the polystyrene bead, due to the transfer of momentum from the photons, equals the difference between the initial and final momentum of a photon. This force F can therefore be defined as the change in momentum over time, $F = \Delta(P)/\Delta(t)$ [46]. The transfer of momentum

is possible due to the polarizable material and the low conductivity of the dielectric particle [44].

The laser beam applied in the OT has a Gaussian intensity profile, where the light intensity is strongest in the middle of the beam and decreases further out [42]. The rays of light will therefore have different intensities based on where they are located according to the center of the laser beam. Rays with higher intensities will exert higher force on a polarized dielectric particle, resulting in the particle being forced towards the region of more intense light in the beam axis. The force responsible for this movement is referred to as the gradient force and is defined as the optical force arising from refraction of the particle. Another force, referred to as the scattering force, will push the particle in the direction of the propagation of the light (Z-direction). This force arises from both the absorption and reflection by the particle. Consequently, in order for the particle to be trapped stably by the laser in all three dimensions, the axial gradient force, pulling the particle towards the focal region, must be greater than the scattering force and the radiation pressure from the photons. The scattering force is responsible for pushing the particle away from the focal region. The balance between the force components results in an axial equilibrium position of the particle slightly beyond the focal point. If the particle moves in the focused laser beam, the imbalance of optical forces will push the particle back to its equilibrium position. The stability of the optical trap can also be influenced by other forces acting on the trapped particle, including gravity and forces exerted by the surrounding medium. To overcome these forces, the OT has to apply a sufficiently powerful laser [44].

3.2.3 Principles behind force measurements

The forces exerted by the laser cannot be directly measured. However, the light scattered by the trapped particle can be used to determine the external forces acting on the particle. These external forces result in a displacement of the particle away from the center of the trapping beam. This imbalance can be induced by for instance Brownian motion of the surrounding liquid, collisions with other particles in the sample solution or pulling forces produced when surface molecules of the particle interacts with something else. A Gaussian beam profile will result in the behavior of the optical trap resembling a linear spring. Based on the displacement of the trapped particle and the trap stiffness, it is therefore possible to calculate the external forces acting on the object. Since the force exerted on the particle is obtained by the deviation

from the equilibrium position, the precision of force measurements depends on the OTs ability to accurately measure the position of the particle [47].

Brownian motion

Brownian motion is defined as random diffusion of particles suspended in a liquid. Even though a particle is trapped by a laser beam, it will also undergo Brownian motion by being constantly bombarded by other molecules in the solution. However, this movement is restricted to the focal volume of the trap. Based on equations 3.3 and 3.4, the Brownian motions can be determined for one dimension at a time [42]:

$$\langle x^2 \rangle = 2Dt \tag{3.3}$$

$$D = \frac{k_B T}{3\pi\eta d} \tag{3.4}$$

$\langle x^2 \rangle$ represents the mean square displacement distance of the particle as a result of Brownian motion. D is the diffusion constant of the trapped object, and t represents the time from zero position. In equation 3.4, where the diffusion constant is obtained, k_B denotes the Boltzmann constant and T denotes the absolute temperature measured in Kelvin. T is usually estimated based on the room temperature, but will be slightly (a few degrees) higher due to the heating of the sample by the laser. η is the solvent viscosity and d is the diameter of the particle. Based on these two equations and the mentioned parameters, the movement of the particle can be calculated for the X, Y and Z direction [42].

Back-focal-plane interferometry

The position of the bead in the optical trap is achieved by back-focal-plane interferometry. When light passes through the trapped particle in an optical trap, the particle will act as a small lens and refracts the rays passing through it. The distribution of the light in the back-focal-plane, after refraction, is detected by a quadrant photodiode (QPD). The back focal plane is located behind the detection objective. The QPD device consists of four equal quadrants, where each of

them detects the light intensity striking it (figure 3.5). The light rays detected are converted to a voltage difference over the device, which is proportional to the difference in light intensity. The displacements signal detected in the lateral directions (x,y) can be transformed into two dimensionless numbers, Q_x and Q_y [42]. These are obtained by the following formulas:

$$Q_x = \frac{(V_2 + V_4) - (V_1 + V_3)}{(V_1 + V_2 + V_3 + V_4)} \tag{3.5}$$

$$Q_y = \frac{(V_1 + V_2) - (V_3 + V_4)}{(V_1 + V_2 + V_3 + V_4)} \tag{3.6}$$

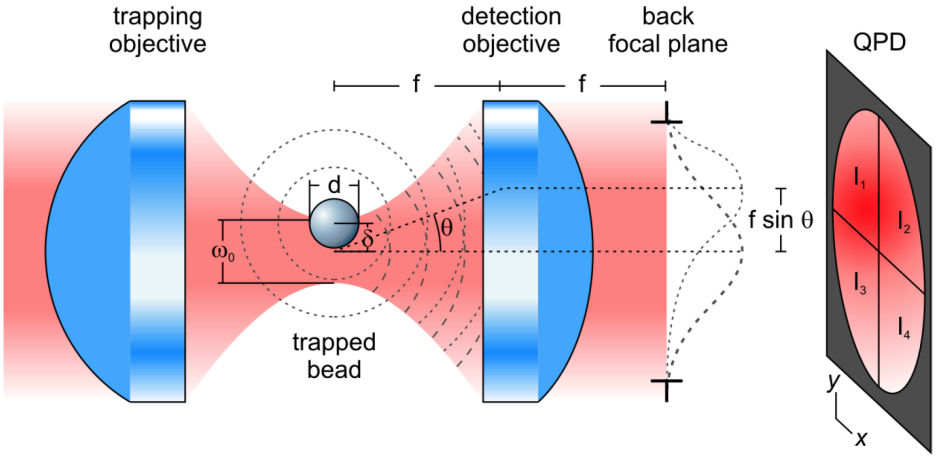

Figure 3.5: Schematic illustration of the principle of back-focal-plane interferometry. Photons refracted from the bead are detected on the back-focal-plane by a quadrant photodiode (QPD). The figure demonstrates the configuration for detection of displacement in the lateral directions: x and y. Figure reproduced from JPK Technical Note for Optical Tweezers, "Quantitative force measurements with optical tweezers: The JPK NanoTracker^{TM}".

The optical trap can be characterized in the lateral directions (x,y) by two spring constants k_x and k_y. The recorded Q_x on the QPD is directly proportional to both the actual displacement (x) from the center of the beam trap and the force (F_x) exerted on the sphere. The same considerations will also apply for the y-axis, and the subscripts x and y are therefore not included in further formulas [42].

As the object moves away from the center of the optical trap, it will experience a force that is proportional to the spring constant k. The detector sensitivity, β, is responsible for translating

the detector signal Q (in volt) into a physical displacement x. According to Hooke's law, the force F can be obtained from the position data, by multiplying the displacement distance x with the spring constant of the optical trap [42]:

$$F = -kx \tag{3.7}$$

Lorentzian shape function

The conversion factors β and k are essential when using optical tweezers as a force measurement device. However, these conversion factors are difficult to obtain by theoretical considerations, and are instead determined by experimental calibration of the optical traps [42].

One method of calibrating the position detector is based on the thermal motion of the object in the optical trap. This thermal motion is believed to follow a distribution that can be fitted to the Lorentzian equation (equation 3.8). The one-sided power spectrum of the Brownian motions of the particle will follow the expression [44]:

$$S(f) = \frac{k_B T}{\gamma \pi^2 (f_c^2 + f^2)} \tag{3.8}$$

where S(f) is the function for the Lorenztian power spectrum, and gives output in units of displacement^2/Hz. γ is the hydrodynamic drag coefficient of the particle, and can be obtained by Stoke's law for a spherical particle (equation 3.9) [44]:

$$\gamma = 6\pi\eta a \tag{3.9}$$

If the solvent viscosity (η) and the radius of the spherical particle (a) are known, the stiffness of the optical trap, κ, can be obtained from the characteristic roll-off or corner frequency of the power spectrum, f_c (equation 3.10) [48]:

$$f_c = \frac{\kappa}{2\pi\gamma} \tag{3.10}$$

By comparing the measured power spectrum (V^2/Hz) with the expected theoretical value (m^2/Hz), the sensitivity of the detector (in m/V), β, is obtained [42]. Figure 3.6 presents a screen

print of the calibration procedure implemented in the NanoTracker software.

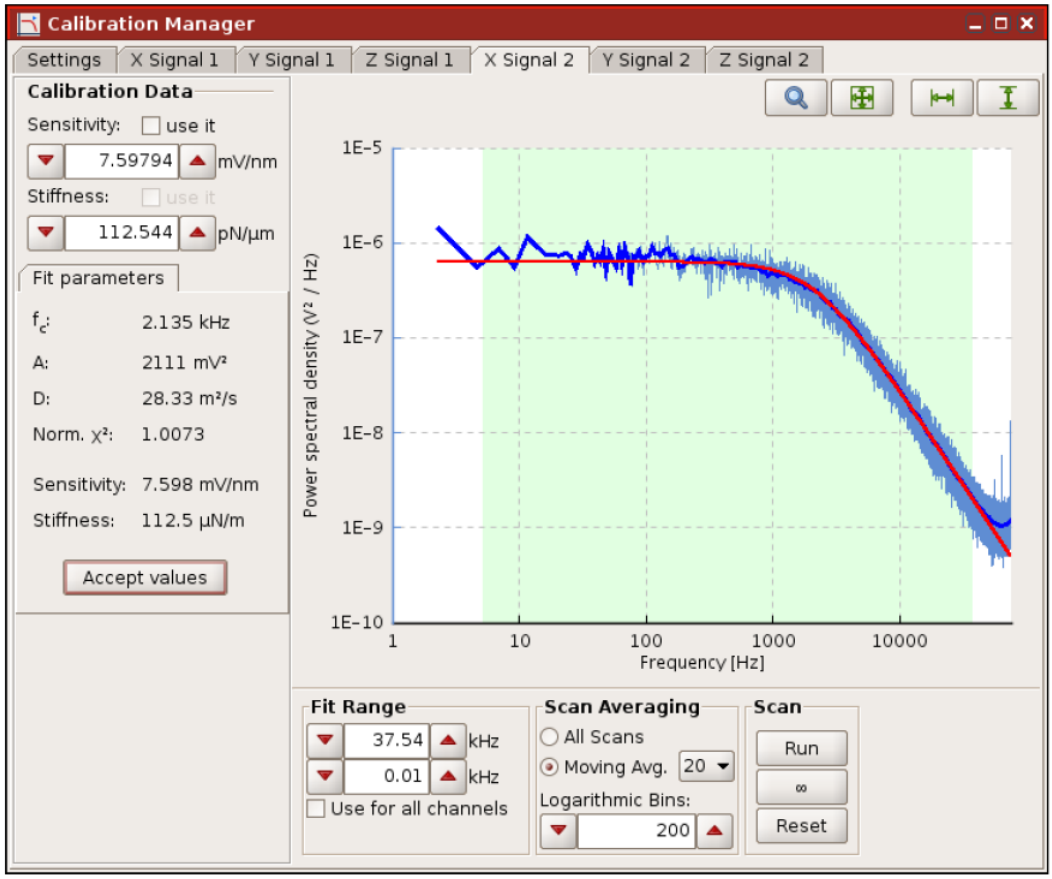

Figure 3.6: Screen print of the calibration procedure implemented in the NanoTracker software. The blue curve is the thermal motion of the trapped particle, that are driven by Brownian motions. The red curve represents the sample data fitted to the Lorentzian power spectrum function. The presented results are obtained by calibration of the particle trapped in trap 2, in the X-direction. This procedure must be carried out for both the x, y and z directions, and both for trap 1 and trap 2. Both the sensitivity of the detector (m/V) and the stiffness of the optical trap (N/m) is obtained from the fitted Lorenzian power spectrum curve, and their respective values are presented in the panel on the left side of the window. The figure is reproduced from JPK Technical Note for Optical Tweezers, "Characterizing quantitative measurements of force and displacement with Optical Tweezers in the NanoTracker^{TM}".

3.3 Dynamic force spectroscopy

The non-covalent intermolecular bond between biomolecules are mainly due to van der Waals forces, electrostatic interaction, hydrogen bonds and hydrophobic interactions. These bonds have a limited lifetime and will eventually rupture when a force pulls them apart with a sufficient strength and time [49, 50]. The strength of these interactions can be quantified using sensitive

force probes, such as an optical tweezers [45]. Dynamic force spectroscopy (DFS) enables the study of these binding forces, and can provide molecule properties such as bond strength. In a DFS experiment, the external force applied to a molecular bond is increased with time. The increase in applied force per unit time is defined as the loading rate (r_f) [51]:

$$r_f = \Delta f / \Delta t \tag{3.11}$$

By increasing the loading rate, the force required to rupture the molecular bond is determined as a function of the loading rate [49, 50]. In an OT, the trapped particle will experience a displacement from the center of the trap, which is proportional to the applied force [45]. The potential barrier landscapes and lifetime of the bonds can be obtained by analyzing the relationship between the bond strength (f) and the logarithm of the loading rate (r_f) [50, 51]. The rupture events of a non-covalent interaction are stochastic processes and the quantification of the bond strength therefore requires several measurements of individual bond rupture events [50].

3.3.1 Rupture force of single interacting pairs

As two objects are moved together, allowed to interact and then separated, the loading rate and magnitude of the bond rupture strength are recorded. The different objects are expected to interact through bonds characterized by different rupture strengths, lifetimes and binding geometries. This will lead to different energy landscapes of the interactions.

3.3.2 Probing the energy landscape of binding objects

In OT studies, the two objects anchoring the bond are moved apart as one of the objects is pulled away with a force that increases over time at a constant rate, $\Delta x/\Delta t$. The loading rate can therefore be defined by the retraction speed and the spring constant of the trap, k [49]:

$$r_f = k(\Delta x/\Delta t) \tag{3.12}$$

This is the basis for the well known Bell-Evans model, which assumes that the association rate (k_{on}) is minimal compared to the dissociation rate (k_{off}). The Arrhenius equation states that

the dissociation rate will then increase with the activation energy [52]:

$$k_{off} \propto exp\left(\frac{-\Delta G^*}{k_B T}\right) \tag{3.13}$$

where ΔG^* is the activation energy, k_B is the Boltzmann's constant, and T is the absolute temperature in Kelvin [52]. Bell-Evans model explains that as an external force is applied to rupture a bond, the thermal activation is aided by the applied force and must be taken into account when determining the new dissociation constant [49]:

$$k_{off}(f) = k_{off,0} exp\left(\frac{x_\beta}{k_B T}\right) \tag{3.14}$$

where $k_{off,0}$ is the rate of dissociation at equilibrium, when no external force is applied. x_β is the thermally average distance from bound state to activation barrier, and f is the applied force [52]. The other parameters are defined above.

The loading force, *f*, is assumed to act in the direction of x_β until the transition state is reached [49]. This consider the case where only a single pair of molecules are interacting, as well as the force increasing linearly with time [52]. Equation 3.14 presents a exponential increase of the disassociation coefficient according to the force [49]. k_{off} can further be used to calculate the lifetime of the bond, τ_0, using equation 3.15:

$$\tau_0 = \frac{1}{k_{off}} \tag{3.15}$$

The probability density *P(f)* for observing a bond rupture between a molecular pair at the force f subjected to constant force loading rate r_f predicted by the Bell-Evans assumption is [49, 52]:

$$P(f) = k_{off,0} exp\left(\frac{x_\beta}{k_B T}\right) exp\left[\frac{k_{off,0} k_B T}{x_\beta r_f}\left(1 - exp\left(\frac{x_\beta f}{k_B T}\right)\right)\right] \tag{3.16}$$

By maximizing equation 3.16, the most probable rupture force (f^*) at a specific loading rate can be obtained [49, 52]:

$$f^* = \frac{k_B T}{x_\beta} ln\left(\frac{r_f x_\beta}{k_{off} k_B T}\right) \tag{3.17}$$

3.4 Shear stress flow chamber

A shear stress flow chamber enables the researcher to subject cells to laminar flow conditions and study their response to fluid shear stresses [53]. The system aims to mimic *in vivo* shear stresses imposed by the physiological environment of cells [54]. The transparent viewing region of the flow cell enables real-time investigation of cell adhesion, as well as imaging of cell morphology both before, during and after flow of the chosen buffer [53]. The flow chamber has been used to study cell reaction upon adhesion to a variety of surface topographies, as well as investigating bacterial adhesion, microsphere deposition and receptor-ligand bonds. Furthermore, it has the potential to gain information about natural phenomenons that are poorly understood, such as the rolling motion of leucocytes or the migration of granulocytes [55].

The shear stress flow chamber is based on the flow of a fluid through a flow channel, which can be shaped as a square or rectangle. The slide placed in the flow channel, also referred to as a coupon, can be of different materials, depending on the application [56]. Typical materials applied include glass, polystyrene and stainless steel. The surface can be further functionalized for the desired application. The flow rate is generally adjusted by a pump, but can also be regulated by hydrostatic pressure [55–57]. The shear stress produced at the wall in the channel can be estimated based on the following equation:

$$\tau_w = \frac{3\mu Q}{4h^2 l} \tag{3.18}$$

with Q corresponding to the mass flow (m^3/s), μ is the fluid dynamic viscosity, h is the half-height of the channel and l is the half-width of the chamber [56, 57].

The establishment of laminar flow can be confirmed by calculating its Reynolds number (Re), which is the ratio of inertial forces to viscous forces. The flow is laminar if the viscous forces predominate, resulting in a Re value of less than 2300 [53]. Re can be calculated by equation 3.19:

$$Re = \frac{\rho Q D_h}{\mu l h} \tag{3.19}$$

where ρ is the fluid density and D_h is the hydraulic diameter [53]. The other parameters are defined above.

3.5 Chemical modification of biopolymers by reducing end modification

The aim of reductive amination is the conversion of a carbonyl group into an amine [58]. In a reversible reaction, the carbonyl group, presented in an open-ring form of a carbohydrate, reacts with a primary or secondary amine to form an imine, also called a Schiff base (figure 3.7). The imine is further reduced to give a secondary or tertiary amine, in an irreversible reaction [59]. The reaction can be performed in one single step, also called a "one-pot" system, where the formation of an imine and its reduction proceeds in one operational stage. Its is also possible for the reaction to proceed stepwise, where the imine is isolated and further reduced in the second stage [58].

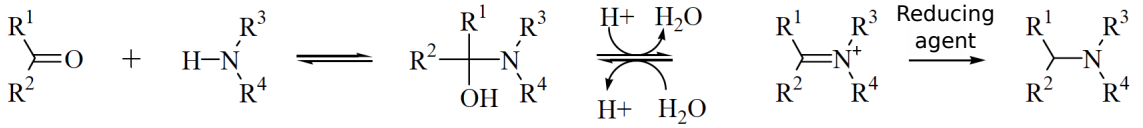

Figure 3.7: General reaction mechanism for reductive amination. A carbonyl group reacts with a primary or secondary amine to form a Schiff base, which is further reduced to give a secondary or tertiary amine. Reproduced from Cosenza *et al.* (2011) [58].

The reaction of a reductive amination requires a carbonyl compound, a reducing agent and an amine donor. Several different reducing agents are commercially available, such as sodium cyanoborohydride ($NaBH_3CN$), sodium triacetoxyborhydride ($NaBH_3(OAc)$), pyridine borane (Pyr-BH_3) and α-picoline borane (Pic-BH_3). The three first mentioned reducing agents are commonly employed for laboratory scale, however they present some challenges, including instability and toxic sub-products. The newly accessible Pic-BH_3 offer a solution to these challenges, by offering stable working conditions in different solvents and no generation of toxic sub-products. In addition, this agent is cost-effective and highly selective [58]. The structure of Pic-BH_3 is presented in figure 3.8

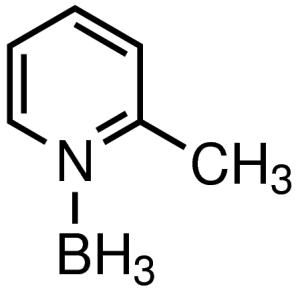

Figure 3.8: Structure of the reducing agent α-picoline borane. Figure achieved from Sigma-Aldrich.

3.6 Soft Lithography

The development of micro- and nano-fabrication techniques has offered great progress in the electronic industry. It has enabled the production of miniaturized circuits that are less expensive and more efficiently manufactured. Miniaturization has also opened up new possibilities within the field of biology through a collaboration with nanotechnology and microfabrication, resulting in the field of nanobiotechnology. This collaboration presents advantages within both fields, where nanotechnology on one hand achieves knowledge on the functional nanosystems of biomolecules. On the other hand, micro- and nano-sized devices can be useful in studying biological materials. Well-established and high resolution nanotechnological approaches, such as X-ray lithographies, electron- and focused-ion beam, photolithography and scanning probe methods, are at the moment unsuitable for biological applications due to lack of biocompatibility and the need of cleanroom facilities and specific equipment. For many of these approaches the cost is also very high and therefore unaffordable for large-scale industry [37].

Based on these limitations, a new set of non-photolithographic patterning techniques was developed in the late 1990s by G. M. Whitesides and his co-workers. These techniques were collectively referred to as soft lithography [37]. The techniques are based on printing and molding by the use of elastomeric stamps, for fabricating micro- and nanostructures for biological applications. The technique offers a rapid, inexpensive and convenient method of producing patterns and structures [6]. The size of the features on the stamp surface can range from 30 nm to 100 µm. These stamps have a variety of applications and are used in techniques such as microcontact printing (µCP), replica molding (REM), microtransfer molding (µTM), micromolding in capillaries (MIMIC) and solvent-assisted micromolding (SAMIM) [60]. As multiple copies of a

stamp can be produced from a single master mold, these simple, reliable and inexpensive techniques can justify the cost and the time consumed of producing the master by high-resolution techniques, such as photolithography [38].

The decreased size of the devices results in a higher demand of the surface properties, regarding their performance ability. Soft lithography has shown to match these demands, and has proven to be well suited in patterning the composition, topography and properties of surfaces. Advantages with miniaturizing such biochemical assays is the reduced need of required analytes and maximization of number of assays performed in parallel [6].

3.6.1 Fabrication of mold by photolithography

Photolithography utilizes light and a light-sensitive polymer, referred to as a photoresist, to create a 3D relief image on a substrate surface. The substrate surface is most commonly a silicon wafer [6]. The generated image will ideally have the exact same shape as the intended pattern in the substrate plane. A binary resist pattern is formed, where the photoresist will cover the substrate in certain areas while other areas are completely uncovered. This is achieved based on the properties of the photoresist. This chemical compound will either polymerize or depolymerize when exposed to light of a specific wavelength. A *positive* resist depolymerizes in exposed areas due to increased solubility, while a *negative* resist experiences decreased solubility in exposed areas and therefore polymerizes. The desired pattern is created by controlling which areas of the resist get exposed, resulting in the removal of certain areas of the resist during developing of the substrate [61]. A photomask is often used to control the exposure, which functions by blocking UV-light in some areas based on the designed pattern. However, designing and producing such a photomask is expensive, difficult and time-consuming. Maskless photolithgraphy offers a solution to these problems by directly exposing the patterns without the need of a mask [62].

A general photolithography sequence consist of the following steps: preparation of substrate, spin coating of photoresist, pre-bake, exposure, post-exposure bake, development and post-bake (figure 3.9). The preparation step is intended to ensure an even and uncontaminated substrate surface, as well as ensuring good adhesive properties for the photoresist. A dehydration bake can be performed to remove water from the substrate surface. The substrate is then allowed to cool, and further covered with the chosen photoresist by spin coating. The solid

components of the photoresist are dissolved in a solvent, which is poured onto the substrate. Spin coating provides an uniform coating of the photoresist, with a well-controlled thickness. The desired thickness of the resist is obtained by adjusting the time and acceleration of each spin speed, as well as the spin speed itself. After coating, the photoresist is dried to evaporate remaining traces of solvent. This pre-bake process helps stabilize the resist film, as well as improving the adhesion of the photoresist. The coated substrate is then exposed to UV light, where a maskless aligner is used to define the exposed areas [61]. This device utilizes an illumination mode of 405 nm or 375 nm and directly exposes the pattern through a raster-scan mode, generating one stripe of the pattern at a time [63]. A negative resist contain a cross-linker which is activated upon exposure. During the post-exposure bake, cross-links in the exposed areas of a negative photoresist is thermally induced, which stabilizes the pattern in the developer [64]. Once exposed, the substrate is submersed in a developer to remove photoresist which is not cross linked. During the post-bake, the final resist image is harden to improve its stability even further [61] .

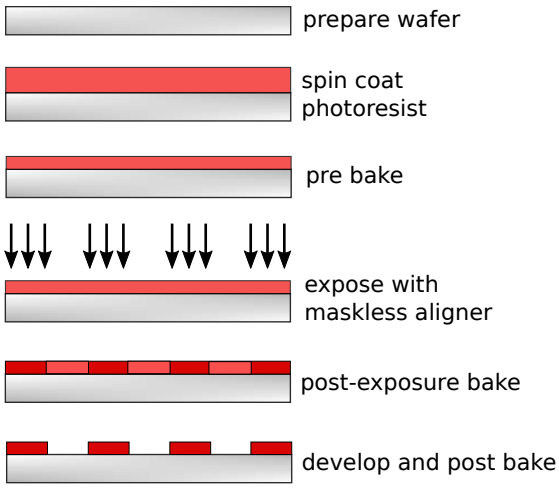

Figure 3.9: Schematic demonstration of the photolithography sequence.

3.6.2 Replica molding

Replica molding is a single step duplication of the three-dimensional topologies present in the surface of a master mold. A liquid elastomeric pre-polymer is poured onto the surface of the master mold, which contains micro- or nanoscaled features, and is further *in situ* polymerized

by thermal curing. The cured polymer will present almost the same dimensions and topologies as the mold by offering less than 3% shrinkage. The elastic quality of the polymer allows it to be peeled off from the master mold and the duplication can be repeated to produce multiple copies [60]. The technique does not require clean room facilities and can therefore be performed in ambient laboratory conditions [38].

3.6.3 PDMS

Poly(dimethylsiloxane)(PDMS) is one of the widely used polymers in the production of stamps and molds for soft lithography techniques. This linear polymer presents an unique combination of properties due to the arrangement of an inorganic siloxane backbone and two organic methyl side-groups for each Si atom (figure 3.10) [37]. Both physical and chemical characteristics of PDMS makes it qualified to work with biological material, such as being nontoxic to cells and proteins, chemically inert, gas permeable, as well as being stable at temperatures required for biological procedures (40–95°C). Another advantage is the transparent nature of PDMS, which allows the use of optical methods to modify the ink or for inspection of the experimental process [60].

PDMS is commercially available as a pre-polymer base and a curing agent, such as Sylgard 184 supplied by Dow Corning. Their low melting point and glass transition temperatures results in the elastomer being a fluid at room temperature [65]. By the process of thermal curing, the liquid material is converted into a solid elastomer due to cross-linking [60]. The time and temperature required for the thermal curing varies and are dependent on the application and type of structures used [38]. This readily available polymer has a low Young's modulus value of about 3 MPa, rendering it quite flexible and guarantees conformal contact with different target substrates. However, this can induce a possible loss of resolution since the molds can suffer from distortions, collapse or sagging [37].

The elastomer has a surface energy value of around 22 mN/m, rendering it hydrophobic with a water contact angle of about 110°. These properties allows small hydrophobic molecules, biopolymers and cells to irreversibly adhere to the surface. In order to bind organic groups, plasma oxygen treatments have presented the possibility of inducing superficial silanol functional groups that can act as reactive sites on the PDMS surface. The surface properties of PDMS

presents another advantage over glass, silicon and hard plastic, that is the capability of reversible or irreversible bonding to different substrates [37].

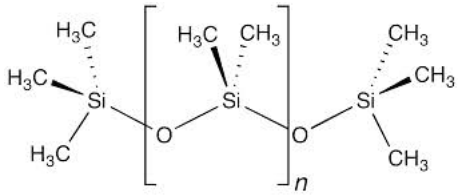

Figure 3.10: Chemical structure of a poly(dimethylsiloxane) (PDMS) unit.

3.6.4 μCP

The original purpose of μCP was to produce self-assembled monolayers of alkanethiolates onto gold surfaces. However, in recent years the application has developed into patterning of proteins and DNA onto solid supports, as well as controlling the spatial distribution of living cells on surfaces [37]. μCP is a form of soft lithography, where an elastomer stamp with features or punches on the micro- or nanometer scale is used to deposit an ink onto a surface of interest. The ink, which can be a chemical substance or small micro- or nanoscopic particles, will form patterns of self-assembled monolayers on the surfaces of substrates [60]. This conformal contact between the elastomer stamp and the substrate determines the success of the printing process [66]. Once the mold has been created, the μCP does not require cleanroom facilities and can be performed in a standard biology lab. Further advantages with this patterning technique is the ability to pattern non-planar surfaces, as well as patterning of larger areas in one single printing step [65].

μCP has proven to be both quick, simple and convenient, and multiple copies of the pattern can be produced from the same stamp, resulting in minimal waste of materials. The principle of the technique is to transfer molecules onto a substrate surface through contact with the raised features of a stamp. The stamp is covered with the chosen ink solution, where excess solution is removed through evaporation, and then placed in conformal contact with the substrate surface. Depending on the ink solution, the transfer of the ink can happen only after a few seconds of contact. When the stamp is peeled off, the stamped ink molecules will remain on the substrate surface. In order to transfer the molecules onto the substrate, binding to the substrate surface

must be more energetically favorable than remaining on the stamp surface [65]. This adhesion can be either specific or non-specific [65]. The ink molecules can attach to the substrate covalently if the surface is reactive or adhere through electrostatic interactions. It is also possible for the molecules to physically adsorb on the substrate [67]. A specific adhesion can be achieved by exploiting the strong interaction between biotin and avidin, where biotin-conjugated proteins are captured by available biotin-binding sites on avidin located on the substrate surface. Through such interactions, the protein ink is more likely to maintain is native conformation [65].

There are some concern regarding how the stamping procedure might impact the function of some biomolecules. The aggregation and functionality of biomolecules might be influenced by the drying process and interactions with the substrate surface. However, studies indicate that the functionality of the proteins is retained in most cases. To retain the function of the stamped biomolecule, it is important to perform the procedure at room temperature and use solvents that are compatible with the molecule. The quality of the stamping can be investigated by tagging the stamped biomolecules with a fluorescent molecule and examining the stamped surfaces with a fluorescence microscope [68].

3.6.5 Microarray of cells

Soft lithography has made it possible to position cells on a surface, while controlling their size and spatial arrangement. Such isolation of cells allows the study of single cell events, or the study of interactions between pairs and triplets of cells. This is a great advantage in cases where cell-based screens are required [6]. A microarray of cells can be obtained by creating patterns with regions that either promote or resist the adhesion of cells to the surface. Cells are able to adhere to many surfaces. However, there are fewer surfaces that resist their adsorption and adhesion, making it difficult to create patterns and structures. An inert surface is therefore required, which can be achieved by covering the surface with a sufficient density of for instance poly(ethylene glycol) [6].

Poly(ethylene glycol)

Poly(ethylene glycol) (PEG) is a condensation polymer of ethylene oxide and water (figure 3.11). The chemical properties renders it possible to utilize this polymer for a range of application, such as within the fields of biology, chemistry and pharmaceutics. The polymer can easily be synthesized into a range of molecular weights and with different end groups [69]. PEG can be linear or branched, with a neutral charge, and is soluble in most organic solvents and water. When attached to other molecules, PEG controls the solubility of the complex, but does not interfere with the chemistry of the molecule [70].

The inert feature of PEG makes it suitable for biological applications, since it does not initiate an immune response [70]. The inert character of PEG-treated surfaces is believed to be due to its electrical neutrality and the reduction in surface interfacial. PEG is able to exclude cells and proteins from its presence in an aqueous environment. When a cell or protein approaches the PEG-treated surface, a repulsive force develops due to a reduction in available conformations of the poly(ethylene glycol) chains. Furthermore, an osmotic repulsive force also develops due to the compression or interpenetration of the polymer chains [71].

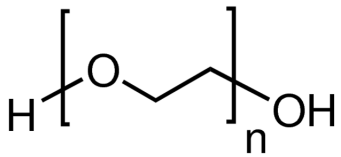

Figure 3.11: Chemical structure of poly(ethylene glycol). Figure reproduced from Sigma-Aldrich.

PEG can be immobilized on surfaces through coupling to a functional group, which possesses affinity for the surface, or through grafting onto a polymer backbone. The latter can be achieved by grafting PEG side chains onto a poly-L-lysine backbone, creating a comblike structure [72]. This complex is referred to as poly-L-lysine-graft-poly(ethylene glycol) (PLL-g-PEG), and a schematic illustration of its conformation is presented in figure 3.12.

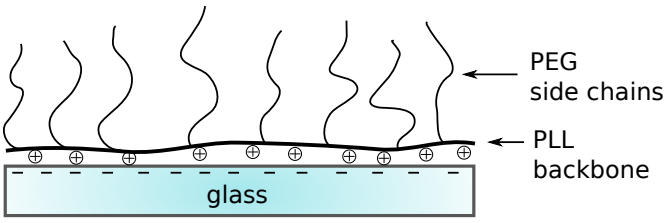

Figure 3.12: Schematic illustration of the conformation of PLL-g-PEG on glass surface in aqueous solution.

Poly-L-lysine

Poly-L-lysine (PLL) is a positively charged polymer composed of α-poly-L-lysine monomers (figure 3.13). This polycation is commonly used to immobilize cells on various surfaces [73]. As a polyelectrolyte, PLL acts to neutralize any opposite charge present on a surface. The positively charged amino groups of PLL will bind to a negatively charged surface, such as glass, metals and metal oxides, through an electrostatic interaction [72, 74]. These amino groups are provided by the lysine residues (pKa = 10.54) in the PLL side chains [75]. The polymer will attain a flat-lying conformation, by orienting parallel to the surface in thin layers [72].

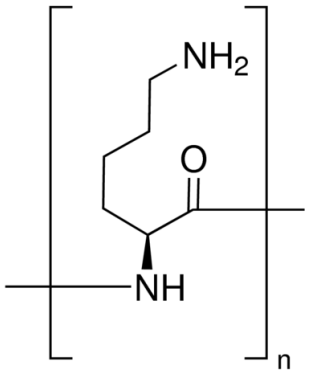

Figure 3.13: Structure of poly-L-lysine monomer. Figure reproduced from Sigma-Aldrich.

The conformation of PLL is influenced by temperature, as well as the properties of the solvent, including the ionic strength and pH. In acidic and neutral solutions, PLL has a positive charge due to the protonation of its amino groups. This introduces an electrostatic repulsion between the side chains, resulting in an extended conformation of the polymer. The polymer will obtain an equilibrium between the P_{II}-helical conformation, which lacks intramolecular hydrogen bonds, and an extended β-strand. As the pH increases, the amino groups gets deprotonated, resulting in a reduction of electrostatic repulsion. The PLL polymer will be structured

as an α-helix or β-sheets structure, depending on the temperature of the solvent [73].

PLL enables immobilization of cells on surfaces based on electrostatic forces. The positive charge of PLL promotes an electrostatic interaction with the negatively charged cell surface. High concentrations of PLL have been shown to present an inhibitory effect on microbial growth [76]. However, yeast cells are more protected than animal cells due to their cell wall [77].

4. Materials and methods

4.1 Chemicals used in the experiments

Chemicals purchased from Sigma Aldrich:

- Boric acid (50 mM, pH 5.8)
- Bovine Serum Albumin (BSA), BioReagent, heat shocked fraction, ≥ 96%, CAS number: 9048-46-8
- D-(+)-Glucose, ≥ 99.5%, MW: 180.16 g/mol, CAS number: 50-99-7
- EDC (N-(3-Dimethylaminopropyl)-N'-ethylcarbodiimide hydrochloride), Chrystalline, CAS number: 25952-53-8
- Fumonisin B1, 5 mg, CAS number: 116355-83-0
- HEPES (4-(2-Hydroxyethyl)piperazine-1-ethanesulfonic acid)) (25 mM HEPES, 150 mM NaCl, pH 7.4)
- Poly-L-lysine solution (0.01%),BioReagent, MW: 150 000 - 300 000 Da, sterile-filtered, suitable for cell culture, CAS number: 25988-63-0
- Poly-L-lysine-FITC labeled, MW: 30 000 - 70 000, MDL number: MFCD00165427
- Protease from *Streptomyces griseus*, powder, CAS number: 9036-06-0
- Mannan from *S. cerevisiae*, prepared by alkaline extraction, CAS number: 9036-88-8
- Yeast extract, for use in microbial growth medium, powder, CAS number: 8013-01-2

Other chemicals:

- Agar bacteriological, Oxoid LTD

- Amino- and carboxyl functionalized polystyrene beads, Spherotech, Lake Forest, IL, USA.
- Bacterial peptone, Oxoid LTD
- PLL-g-PEG (PLL(20)-g[3.5]-PEG(2)), powder, SuSoS AG
- Soluble β-1,3/1,6-glucan from *S. cerevisiae*, 18 mg/mL, Biotec Pharmacon AS (http://www.spherotech.com/)

4.2 *S. cerevisiae* cells

The strains BY4741 (wild type) and Δmnn9 of *S. cerevisiae* were kindly provided by Hélène Martin-Yken, LISBP, Université de Toulouse, CNRS, INRA, INSA, 31400 Toulouse, France. The Δmnn9 mutant has defects in the synthesis of the cell wall component mannan, resulting in an altered cell wall composition [78]. The composition of the cell wall of the mutant strain compared to the wild-type (WT) is presented in table 4.1

Table 4.1: The composition of the cell wall of *S. cerevisiae* strains BY4741 (wild type) and mutant Δmnn9 [78].

Strain	Mannans (µg/mg)	β-1,3-glucan (µg/mg)	β-1,6-glucan (µg/mg)	Chitin (µg/mg)	Protein (%)
BY4741	304 ± 36	357 ± 11	138 ± 4	45 ± 5	14.4 ± 1.0
Δmnn9	170 ± 38	299 ± 21	123 ± 1.5	62 ± 2	43.2 ± 4.6

WT yeast cells were subjected to protease treatment and heat shock, to investigate if the resulting changes in the cell wall composition improved their ability to interact with fumonisin B1.

4.2.1 Cultivation of *S. cerevisiae*

Cells of the strains BY4741 (wild-type) and Δmnn9 were cultivated on agar plates containing YPD medium and further stored in a cooled storage room with a temperature of 4°C. Instructions for preparation of YPD medium is presented in appendix B.

Before experiments, cells were inoculated overnight in 25 mL of liquid YPD medium at 30°C and with constant agitation at 130 rpm. Yeast cells were isolated from the overnight culture by a washing procedure, resulting in a up-concentrated solution of yeast cells. 1 mL of overnight culture was centrifuged in an eppendorf tube at 4000 rpm for 5 min. The supernatant was discarded and cells re-suspended in 1 mL of distilled water, before further centrifuged at 4000 rpm for 5 min. The cleaning step was repeated two more times and the remaining pellet was re-suspended in buffer. For the optical tweezers experiments, the cells were suspended in 200 µL of HEPES buffer, while 1 mL of PBS (pH 7.5) was applied for the flow chamber experiments.

4.2.2 Protease treatment of *S. cerevisiae* cells

Yeast cells were subjected to a protease treatment, in order to reduce the amount of mannose peptides in the cell wall. This protease mixture from *Streptomyces griseus* is highly nonspecific, but prefers to hydrolyze peptide bonds on the carboxyl side of glutamic or aspartic acids (Product Information from Sigma-Aldrich). The effect of the protease treatment was investigated using optical tweezers. The protease was kindly provided by Marion Schiavone, LISBP, Université de Toulouse, CNRS, INRA, INSA, 31400 Toulouse, Lallemand SAS, Blagnac, France. A 20 mg/mL stock solution was prepared by dissolving 20 mg of protease in 1 mL acetate buffer (pH 5). 20 µL of the stock solution was added to yeast cells dissolved in HEPES, with a total volume of 200 µL, and the cells were incubated at 37°C for at least 2 hours. After incubation, the yeast cells were spinned down at 3000 rpm for 3 min at room temperature. The supernatant was removed, and the remaining pellets were washed two times with 200 µL of acetate buffer. The washing procedure ensures removal of the protease and cleaved off mannose peptides. After the cleaning step, the supernatant was removed and the pellet was dissolved in 200 µL of HEPES buffer.

4.2.3 Heat treatment of *S. cerevisiae* cells

In order to introduce a structural change to the cell wall, WT yeast cells were exposed to heat stress by boiling the cells in buffer at approximately 80°C for 1 hour. Heat treated cells were investigated using both optical tweezers and flow chamber, where the cells were suspended in HEPES and PBS, respectively.

4.3 Covalent immobilization of fumonisin B1 and yeast cell wall components onto polystyrene beads or glass surfaces

In order to study the ability of *S. cerevisiae* cells to interact with fumonisin B1, the isolated cell wall components mannan and β-glucan, as well as fumonisin B1, were immobilized on polystyrene beads. The polystyrene beads (Amino/Carboxyl Polystyrene Particles, 5% w/v) were purchased from Spherotech, Inc and the β-glucans were provided by Biotec Pharmacon AS. The boric acid used in functionalization of the polystyrene beads was prepared by Gjertrud Maurstad. All the other chemical used were purchased from Sigma-Aldrich.

4.3.1 Functionalization of polystyrene beads

Immobilization of fumonisin B1

Fumonisin B1 was immobilized on both amino- and carboxyl-functionalized polystyrene beads, with respective sizes of 2.18 µm and 2.10 µm, in order to investigate if the free amino-group on C2 did participate in the interaction. The fumonisin B1 molecules were covalently attached to the beads using the water soluble coupling agent EDC, which introduces a covalent bond between a carboxyl group and an amino group (figure 4.1) [79].

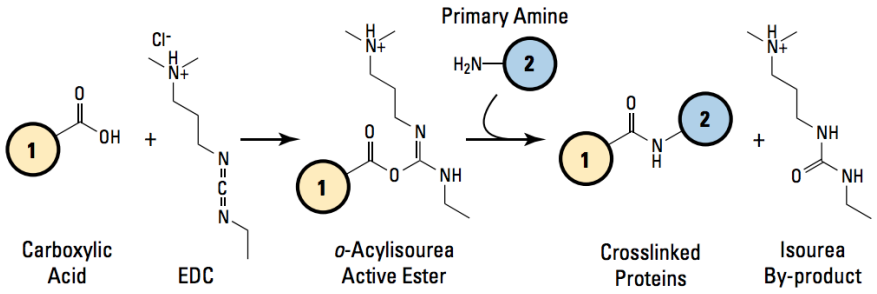

Figure 4.1: Working principle the EDC (N-(3-Dimethylaminopropyl)-N'-ethylcarbodiimide hydrochloride) coupling agent. EDC is able to introduce a covalent bond between carboxyl- and amino groups. Molecules (1) and (2) can be peptides, proteins or other chemicals with available carboxyl or primary amine groups. Figure reproduced from Thermo Scientific Crosslinking Technical Handbook [79].

If carboxyl-functionalized polystyrene beads were applied, then fumonisin B1 was immobilized through its amino-group, while using amino-functionalized beads, one of the propane-

tricarboxylic acid moieties on the side arms participated in the covalent bond. The amount of fumonisin B1 needed to achieve a sufficient coverage of the polystyrene beads was also investigated. Experiments were performed with both 10 µL and 1 µL of fumonisin B1 (5 mg/mL in acetonitril) for 1.0 µL of NH_2-functionalized beads. The reaction was performed in 100 µL of boric acid (50 mM, pH 5.8) with approximately 0.5 mg EDC. After mixing by vortexing, the sample was placed in a rotary shaker overnight. Before use, the fumonisin B1-coated polystyrene beads were washed to remove excess reactants and free fumonisin B1 molecules. The beads were then spinned down at 6000 rpm for 1 min at 23°C. The supernatant was removed and the beads were resuspended in 200 µL HEPES. The cleaning step was repeated, and the desired final concentration of beads was achieved by dissolving the beads in 200 µL of HEPES. The coated polystyrene beads were sonicated for 10 min in an ultrasonic bath prior to experiments, in order to reduce the amount of aggregated beads.

Immobilization of β-glucan and mannan

The polymers β-glucan and mannan were immobilized on 3.36 µm amino-functionalized polystyrene beads through the process of reductive amination. A final concentration of 1 mg/mL of polymer was to be immobilized on 10 µL of polystyrene beads, using 25 µL of 40 mg/mL picoline-borane (Sigma-Aldrich) in 96% ethanol. The solution was adjusted with MQ water until a final volume of 500 µL. The solution was incubated on a rotary shaker for 48 hours at room temperature. To remove free polymer chains and excess reactants, the polysaccharide coated polystyrene beads were washed with HEPES buffer as described for fumonisin B1 beads in the previous section. The beads were suspended in a final volume of 200 µL HEPES, and further sonicated as described for fumonisin B1-coated beads.

4.3.2 Coating of glass slides

For the flow chamber experiments with fumonisin B1 against viable and heat treated BY4741 cells, the glass coupons were coated with fumonisin B1. Additionally, the circular coverslips used in optical tweezers experiments were coated with bovine serum albumin (BSA) to prevent beads and cells from adhering to the glass surface.

Immobilization of fumonisin B1 on glass coupons

The coupon surface was first functionalized by silanization, using 6 µL of N-[(3-Trimethoxysilyl)-propyl]ethylenedamine triacetic acid trisodium salt in 500 µL of 1 mM acetic acid. The structure of the silane is illustrated in figure 4.2. The glass coupons were incubated with the silane-solution for 20-30 min. After incubation, excess solution was pipetted off and the coupons were further washed in MQ water. The carboxyl-silane-functionalized surface was then incubated for 1 hour with a solution of 0.25 mg/mL fumonisin B1 in boric acid (50 mM, pH 5.8), with 5 mg/mL EDC. A volume of approximately 500 µL was needed to completely cover the coupon surface. Excess fumonisin B1 solution was removed and the surface cleaned with MQ water and dried with N_2 gas.

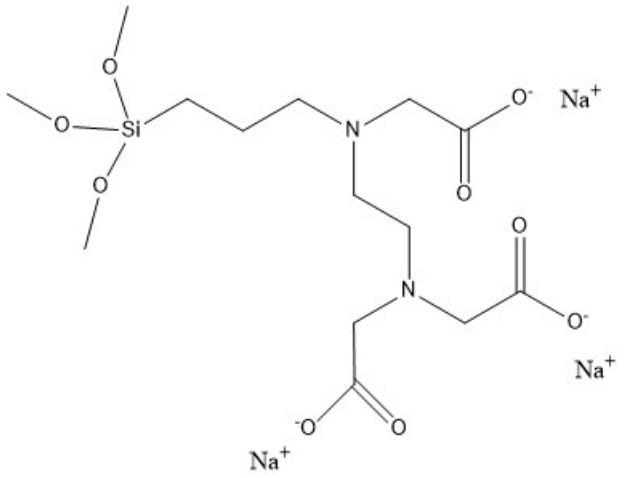

Figure 4.2: Chemical structure of N-[(3-Trimethoxysilyl)-propyl]ethylenedamine triacetic acid trisodium salt. Figure modified from PubChem Compound Database.

Bovine serum albumin (BSA) coating

The coverslips used in the optical tweezers experiments were coated with a solution of bovine serum albumin (BSA) to prevent adhesion of functionalized beads and yeast cells to the glass surface. Prior to the BSA-treatment, the glass slides were washed with MQ and dried with N_2 gas in order to remove dust and other contamination on the surface. The slides were incubated with a 1 mg/mL solution of BSA in MQ water for 20 min, and further washed in MQ and dried with N_2 gas. The BSA molecules are able to adhere to the glass surface by electrostatic interactions. New BSA-coated glass slides were prepared for each day performing experiments.

4.4 Quantification of interactions by the use of optical tweezers

4.4.1 Instrument set up of JPK optical tweezers

The dual trap optical tweezers used in these experiments are NanoTracker from JPK (figure 4.3), with an integrated Zeiss Axio Observer inverted optical microscope. The device allows the use of two independently controlled traps, due to a polarized beam splitter. Absolute light intensity and power ratio distributed between the two traps can be altered continuously. Trapping is performed using a high-intensity 3W laser operating at a wavelength of 1064 nm and with a Gaussian beam profile. The laser light is coupled into the Zeiss microscope, which contains two objectives; one for trapping and one for detection. These are both water immersion objectives, with a magnification power of 63x and 1.20 numerical aperture. A LED light source illuminates the sample, which is further imaged by a CCD camera. Ultra fast steering of the laser beam, both in the x and the y axis, is offered by galvanic mirrors. Control of the laser beam in the z direction in achieved by a movable lens attached to a linear motor. The sample holder is controlled by a motorized sample position system, consisting of both a long-distance XY translation stage and a closed-loop piezo stage [80]. To dampen the interference of vibrations in the building, the optical tweezers platform is positioned on an air vibration isolation table.

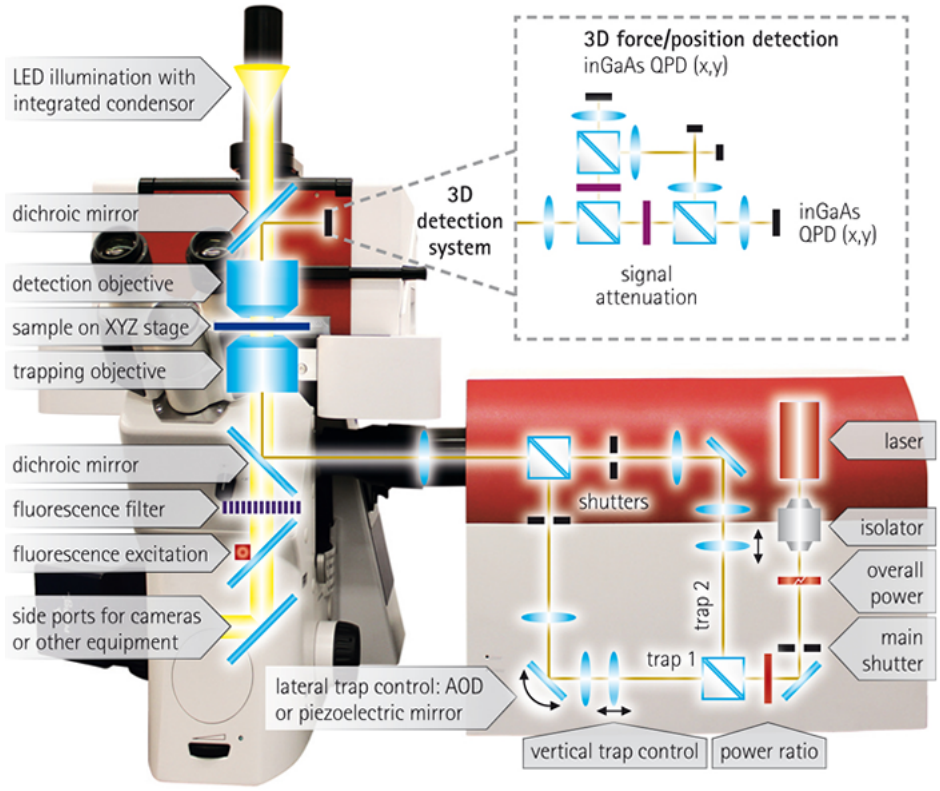

Figure 4.3: Schematic diagram of the JPK NanoTracker Optical Tweezers. Figure achieved from JPK Instruments.

4.4.2 Preparation of sample chamber

The sample was prepared in a closed chamber, referred to as a liquid cell. The housing consists of a circular coverslip (30 mm diameter, thickness number 1), two strips of double-sided tape used to create a channel and a rectangular 20 x 50 mm coverslip (Figure 4.4). Before mounting the liquid cell, the circular coverslip was pre-coated with bovine serum albumin (BSA, Sigma) as described in section 4.3.2. The liquid cell was prepared before each experiment. The width of the channel can be altered, but is usually set to approximately 4 mm. The precise sample volume depends on the size of the channel, but with this set-up a sample size of about 14 µL is inserted into the channel. By using a pipette, the sample drop was placed on one edge of the channel and further dragged into the channel by capillary forces. To prevent the sample from drying out during the experiment, a drop of nail polish was placed at both ends of the channel to seal it off. The sample solution contained 5 µL from two different polystyrene beads solutions (section

4.3.1) in 200 µL HEPES. For experiments performed with cells, the sample solution contained 5 µL of polystyrene beads solution and 5 µL of yeast solution (section 4.2.1).

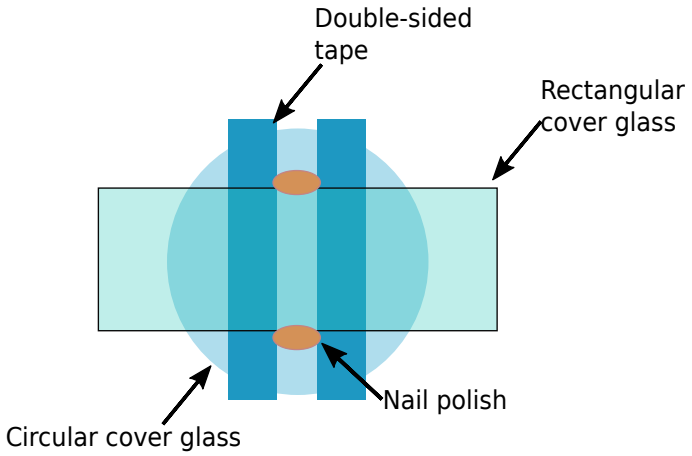

Figure 4.4: Liquid cell used in optical tweezers experiments.

4.4.3 Force measurements using the optical tweezers

After turning on the instrument, followed by the software, the laser power requires about 1-2 hours to stabilize. Performing measurements on the sample must therefore wait until the stabilization of the laser is completed. The liquid cell was prepared as described above and loaded in the sample holder, and further placed in the sample chamber. A drop of Zeiss oil was placed on both sides of the liquid cell, in the center of the sample channel. The trapping and detection objectives were adjusted to get the sample in focus. The microscope was further adjusted to Köhler illumination, achieving both sample and blender in focus. This involves closing the field diaphragm and further adjusting the height of the detection objective to obtain clear edges of the octagonal light source. The field diaphragm was then opened, and the optical tweezers are ready for initiating measurements. Two beads with different functional surface, or one functionalized bead and one yeast cell, were trapped by each of the two lasers. The beads representing different functional surface are chosen to have different size, to be able to discriminate between the two types of beads.Figure 4.5 illustrates optical traps with two trapped beads.

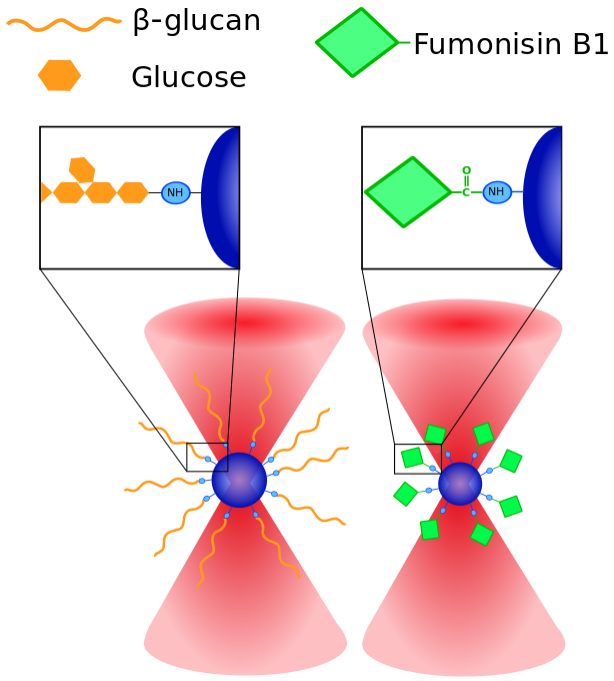

Figure 4.5: A schematic drawing of optical traps with two trapped beads. One trap contains a β-glucan coated amino bead, while the other contains a fumonisin B1-coated amino bead. Fumonisin B1 is covalently bound through one of its carboxylic acid moieties, while β-glucan is attached by its reducing end through reductive amination.

Calibration

The size of the trapped cell was determined by the JPK NanoTracker software. The measured diameter of the cell, as well as the manufactured size of the beads, was used as input for the Calibration Manager. Every time new beads or cells are trapped, the stiffness and sensitivity of both traps must be calibrated by the software. The calibration is based on measuring Brownian motions for 8 seconds, resulting in 8 parallel measurements. The Lorenzian function is further fitted to the measured power spectrum of Brownian motion, where the stiffness and sensitivity is calculated based on the corner frequency, also referred to as the roll-off frequency (equation 3.10 in section 3.2.3), of the fitted Lorenzian. The calculated fit must then be marked off to be used in the experiment. The calibration of the stiffness is based on a temperature of 25°C. The room temperature was approximately 21°C, but due to heating of the sample by the laser, the temperature of the sample was estimated to be a bit higher.

Parameter settings

The location of the beads in the z-axis was adjusted so that the two beads were located at the same height. This was achieved by placing the small bead a little lower than the larger bead. By gently moving them up and down, it was estimated that the small bead should be placed at approximately - 0.1 µm to - 0.25 µm, and the larger bead in the range of 0.3 to 0.45 µm.The trapped beads were further aligned on a horizontal line. The smallest bead was usually chosen as the movable bead, while the other was kept stationary. The distance between the beads was reduced until the two polystyrene beads were in contact and gently pushes each other out of the laser focus, which can be observed as an increase in the force acting on the beads. The separation distance was generally kept at maximum 2 µm, due to a larger distance generating a bigger data file, as well as resulting in more time consuming measurements. During the measurements, the speed of movement can be regulated, in addition to the time period of contact, also referred to as the hold-time. A speed of 1 µm/sec and a hold-time of 0.5 sec was found to be most efficient.

The forces acting on the beads are measured during the displacement. If there is any interaction it will be detectable when the beads are moving apart from each other. The pulling force required to move the bead to its equilibrium position increases as more of the bead is displaced from the center of the optical trap.

4.4.4 Data analysis

For each observed rupture event, the bond strength and corresponding force loading rate were determined based on the magnitude and slope of the force jump, respectively. The JPK OT-instrument generates a text-file, which contains a large amount of information about the rupture events, including the calibration parameters. The corresponding values of f^*, k_{off} and x_β can be obtained from the text-file using the programs iNanoTrackerOT3D and ForceSpecAnalyse, both developed using IDL Data Visualization Software and written by Bjørn Torger Stokke, Professor at the Department of Physcis at NTNU. In a pre-process and pro-process program, the recorded change in force in X, Y and Z direction for both trapped objects are combined and further analyzed.

iNanoTrackerOT3DPreProcess3.pro

This program integrates information from the text-file provided by the OT. Several graphs are generated for both trapped objects in the X, Y and Z position, where each graph contains information about one of the objects in one of the three dimensions. The obtained data is further combined into a single position-coordinate. Since both trapped objects are displaced during interaction, the change in force of both objects are combined into a single force-value using equations 4.1 and 4.2

$$\Delta F = F(retract) - F(approach) \tag{4.1}$$

where Δ F refers to the change in curves, and *F(retract)* and *F(approach)* refers to the interaction forces for the retract curve and approach curve, respectively.

$$\sum F = \Delta Fx + \Delta Fy + \Delta Fz \tag{4.2}$$

Performing equation 4.2 for both trapped objects, and further adding the obtained values, generates a combined curve of the forces. Consequently, the baseline of the approach-retract-curves was evened out and a horizontal baseline was produced. A new ".txt" file was generated, which was further analyzed with iNanoTrackerOT3DPostProcess2.pro

iNanoTrackerOT3DPostProcess2.pro

The combined curve of the forces provided by the pre-process program is used as input for the iNanoTrackerOT3DPostProcess program, in order to calculate the rupture force and loading rate. The loading rate, defined as the external force applied per time unit (df/dt), can be calculated from the slope of the force curve:

$$r_f = \frac{\Delta y}{\Delta x}\frac{\Delta f}{\Delta d} \tag{4.3}$$

where f is the force and d is the distance. The area of the force curved used for fitting of the loading rate is indicated by the red line in figure 4.6a. The unbinding force is estimated by fitting a vertical line from the baseline to the top of the force jump, which is indicated by the yellow line

in figure 4.6a. A good estimation is achieved if the vertical line is fitted to a coherent vertical line of the force-curve. It is possible to obtain several rupture events when an interaction curve presents multiple interactions. The force and loading rate estimations are further written to an "out.txt" file.

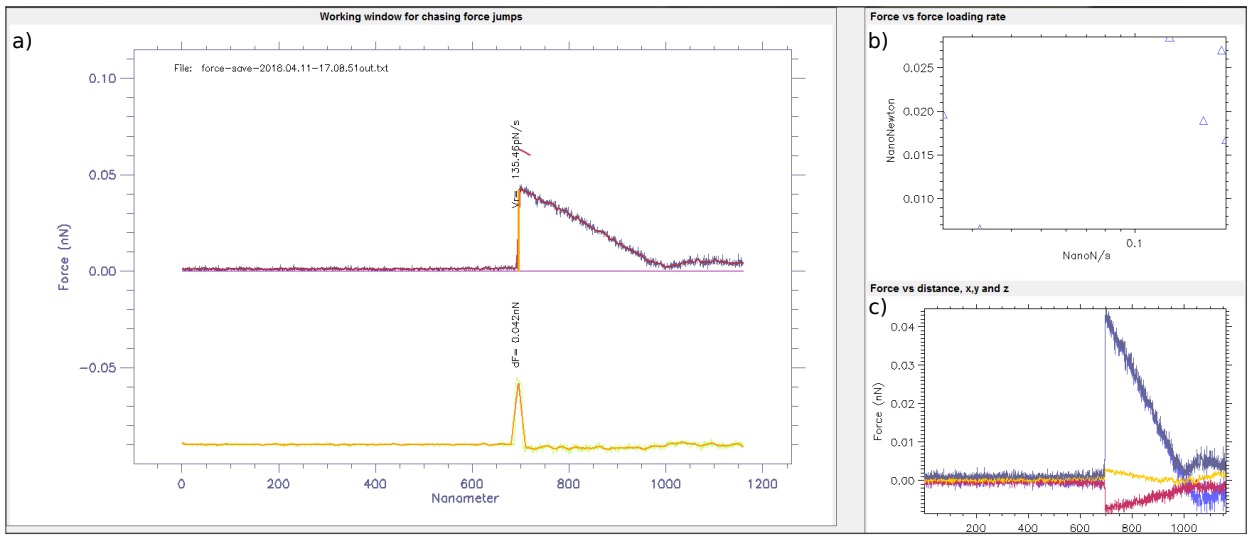

Figure 4.6: Screen print of interaction analysis in the iNanoTrackerOT3DPostProcess program. (a) The purple curve is the combined curve obtained from the iNanoTrackerOT3DPreProcess program. The yellow line estimates the unbinding force, while the red line indicates the area of the force curve used for fitting of the loading rate. The orange and green curve presents the second derivative of the purple curve, where the peak indicates the force of the rupture event. (b) Overview of the distribution of unbinding forces relative to the loading rate. (c) A combined "Force vs distance" plot of the graphs generated for both trapped objects, indicating the relationship between force and distance in the x, y and z-direction.

ForceSpecAnalyse

The program ForceSpecAnalyse divides the data set of force and loading rate into suitable distributions. A histogram is generated for each of the distributions and a fit of *P(f)* (equation 3.16) is added to each histogram. By maximizing equation 3.16, the most probable unbinding force is obtained for each distribution. The fitting also provides the parameters x_β, k_{off} and τ_0. The number of histograms is manually set by the user, and is based on the number of data points and the spread in the data. A large data set is required, in order to obtain sufficient data points for each histogram so that the fit of *P(f)* produces a peak.

SigmaPlot

All figures presenting data related to DFS, such as histograms and galleries of force-jumps, were processed and presented using Sigma Plot, a mathematical and statistical software.

4.5 Preparation of samples for AFM imaging

The effect of immobilizing fumonisin B1 onto a glass slide using silanization was investigated by AFM imaging of the glass surface. The fumonisin B1-treated surfaces were exmamined by Nina Bjørk Arnfinnsdottir (Department of Physics, NTNU).

The glass slides were silanized as described for the flow cell coupons in section 4.3.2. The glass slides applied in AFM experiments are quite smaller than the coupons, and a volume of approximately 50 µL was needed to cover the entire glass surface. For investigating the difference between simple adhesion of fumonisin B1 and covalent immobilization, a control surface was also investigated where the glass slide was immersed in a fumonisin B1 solution (0.25 mg/mL in 50 mM boric acid, pH 5.8). The control sample was incubated with the fumonisin B1 solution for 30 min, before washed in MQ water and let to dry in a petri dish on a parafilm cover. The AFM imaging of the glass slides was performed in the tapping mode. The AFM images were processed and presented using IGOR pro software, which also calculated the mean surface roughness of the obtained images. The program controlling the AFM in the IGOR software has been produced by Asylum Research, and the current version is AR15. The surface roughness can give a qualitatively evaluation of the deposition of fumonisin B1 on the differently treated surfaces.

4.6 Shear stress flow chamber experiments

4.6.1 Assembly of flow cell

The flow cell applied in this study consisted of a rectangular flow channel (12 mm width, 25.2 mm length and 200 µm thickness). All equipment for the flow cell was cleaned with 70% ethanol before use. A small screw with O-ring was positioned under the coupon housing chamber, in the flow cell. After the experiment, this screw is removed and a small screwdriver is used to push

the coupon out of the chamber. To avoid possible leakage, all screws are covered with a small amount of grease. The flow cell chamber was placed on a plaque support, which was mounted onto a plexiglass plate, and further fixed by inserting a screw in each of the four corners of the chamber. The glass coupon (~ 1 mm thick) was positioned on top of a small metal plate in the coupon housing chamber, where a small amount of grease was used to keep the coupon in place. The metal plate allows the coupon to be leveled with the bottom of the flow channel, creating a gap of 200 μm between the coupon surface and the cover glass.

The coupon had been treated with fumonisin B1, as described in section 4.3.2. A cover glass, cleaned with 70% ethanol and further dried, was placed in the notch of the chamber, on top of the coupon. A thin layer of grease was added on the rest of the surface of the chamber, in addition to around the edge of the glass slide. This is to prevent leakage of buffer from the flow cell and to further establish laminar flow. The silicon seal was positioned, and a black top clamping plate was placed on top. The plate was fastened by 10 screws in a quincunx order. The procedure for the assembly of the flow cell is demonstrated in figure 4.7.

4.6.2 Procedure for shear-stress flow chamber experiments

The buffer supply tank was filled with 20 L of PBS buffer. Instructions for preparation of PBS buffer is presented in appendix B. All the tubes were checked if connected properly, and the tubes connected to the flow cell were secured by the use of white strips, two on each side of the chamber and one on the side facing the next tube. The tubes were further filled with PBS solution, and both the tubing and the flow chamber were checked for leakage. The remaining air bubbles in the tubes were also removed through the bubble trap and the outlet tube. The injection loop was also filled with PBS solution.

S. cerevisiae cells were prepared as described in section 4.2, and PBS was added to obtain an optical density of about 5, which gave approximately 200 cells per sample area at 40x magnification. Experiments were conducted with both viable and heat treated cells. A 1 mL suspension of *S. cerevisiae* cells was slowly injected through the injection loop and further into the flow chamber using a 1 mL syringe. The suspension was let to attach to the coupon surface for 50 min under static conditions. During injection, the valve on the bubble trap must be open. The flow cell was further mounted onto a Nikon eclipse LV100 microscope sample stage. The cor-

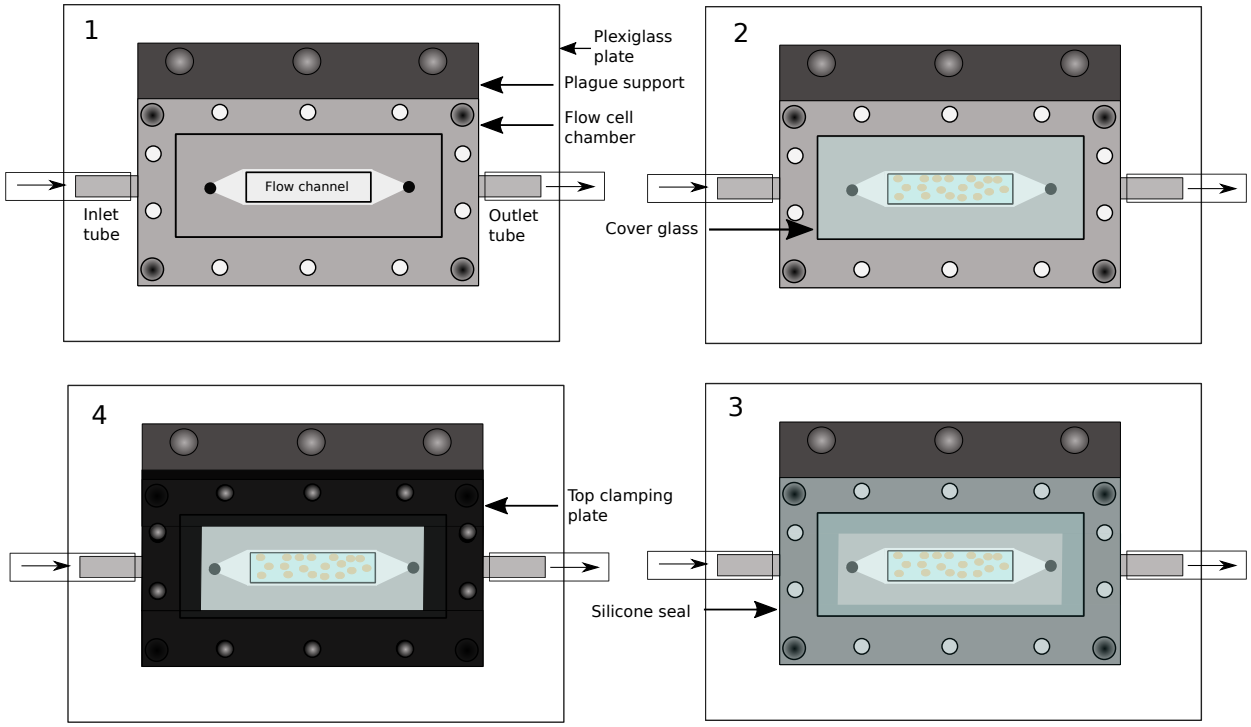

Figure 4.7: Stepwise procedure for assembly of the flow cell. 1) A screw with O-ring is positioned under the coupon housing chamber, which is not demonstrated. The flow cell chamber is mounted on a plaque support, which is further attached to a plexiglass plate. 2) A coupon covered with a molecule of interest is positioned in a the coupon housing chamber, and a cleaned cover glass is further placed on top of the coupon. The remaining surface of the chamber is covered with a thin layer of grease, especially around the edges of the cover glass. 3) The silicon seal is positioned so that it covers the outer edges of the cover glass. 4) The black top clamping plate is positioned and fastened by 10 screws in a quincunx order.

responding Nikon software was used to capture images of the chosen sample area. The sample area must be located at the end of the coupon, near the output tube. This is due to the laminar flow still establishing at the upstream part of the coupon. When an area of the coupon was in focus, an image was taken and the number of single cells were counted and registered in a custom made excel sheet.

After 50 min of adhesion, a rinsing step with PBS was performed for 10 min at a height of 28 cm of the constant-level tank. This height corresponds to a flow rate of 0.001 mL/s, which ensures a rinsing procedure at a low rate, to obtain a stabilized system and remove unbound or loosely-adhered cells. Laminar flow was then initiated by further increasing the flow rate every third min, and the corresponding weight of run trough PBS buffer was measured and registered in the excel sheet.

Images were collected using the optical microscope Nikon Eclipse LV100. The microscope contains a 40x ultra-long working distance objective, and the images were recorded by a camera (digital STGHT DS-2MBW, Nikon) and presented by the NIS-Elements F3.0 video acquisition software. Every third min, the image collected was used to manually count the number of cells present.

The flow rate was first adjusted by hydrostatic pressure, by increasing the height of the constant-level tank, resulting in rates ranging from 0.001 to 0.3 mL/s. When the rack had reached the maximum height of 80 cm at the rack, the flow rate was further increased by using the volumetric pump. Maximal obtained Reynolds number was equal to laminar flow conditions. The wall shear stress (τ_w) during the experiments was in the range 0-80 Pa.

A schematic diagram for the setup of a shear stress flow cell experiment is presented in figure 4.8. The experiments were performed at least in triplicates for each different condition, with different FB1-coated or only silanized coupons and independently grown *S. cerevisiae* cultures.

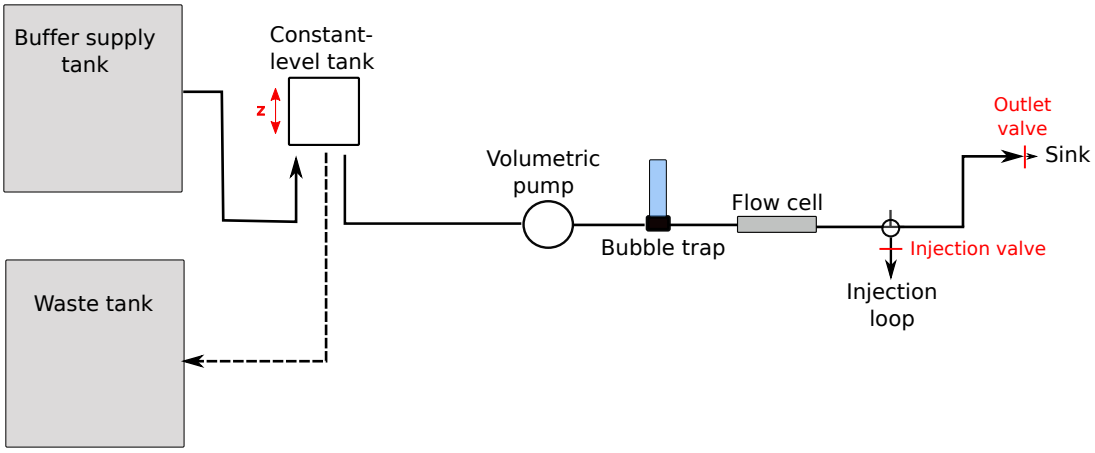

Figure 4.8: Schematic diagram for the setup of shear stress flow chamber experiments.

4.6.3 Cleaning procedure of coupons

The coupons were cleaned by first removing the visible contamination by ethanol and by rubbing with some paper. The coupons were then transferred to a 2% (v/v) solution of RBS liquid detergent at 50°C for about 1 hour and further at room temperature overnight. Traces of the detergent on the coupon surface was washed off by a rinsing procedure, in which the coupons were dipped into first five baths of MQ water at 50°C and then in five baths of MQ water at room

temperature. The coupons were then dried by the use of N_2 gas and further placed in a petri dish on a sheet of parafilm. The coupons were further cleaned by plasma cleaning, to remove remaining traces of contamination. The plasma cleaning was performed by Cécile Formosa-Dague, LISBP, Université de Toulouse, CNRS, INRA, INSA, 31400 Toulouse, France.

4.6.4 Data analysis

The number of cells present at each measurement, as well as the amount of run through buffer were recorded in a custom made excel sheet. For each measurement, the buffer flow rate (mL/s), shear stress (Pa) and the percentage of remaining cells were calculated. The shear stress was obtained from equation 3.18, which is presented in section 3.4. How the different parameters were calculated is explained in the appendix D.

4.7 Preparation of microarray of yeast cells

4.7.1 Fabrication of PDMS stamp

The PDMS stamp used for microcontact printing was produced in a clean room at NTNU by Kertu Liis Krigul. The pattern of the PDMS stamp was designed by using the software CleWin. The fabrication procedure of a PDMS stamp is demonstrated in figure 4.9.

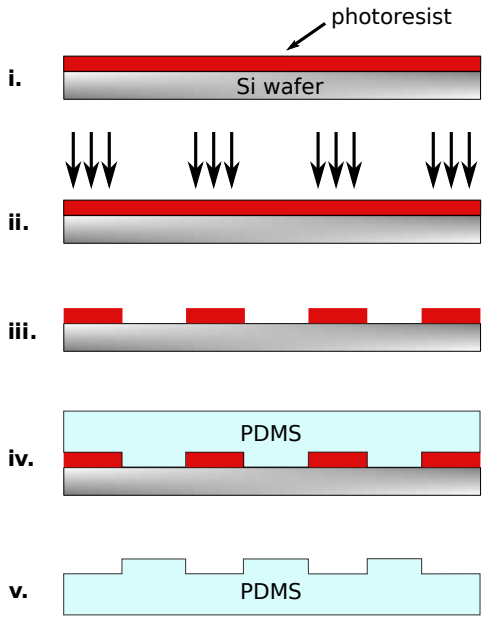

Figure 4.9: (i) A silicon wafer is used as the substrate, which is further coated with the photoresist mr-DWL 5 through spin coating. (ii) The photoresist is exposed to UV light using a maskless aligner, allowing direct exposure of the desired pattern without the need of a mask. (iii) A developer is used to remove unexposed photoresist, resulting in the formation of a 3D patterned surface. (iv) The PDMS pre-polymer and its curing agent is mixed and poured onto the patterned silicon wafer. (v) The polymer is hardened through thermal curing and can be pealed off from the mold. The PDMS is then ready to be applied for microcontact printing.

Photolithography

A 2" silicone wafer (University Wafers) was cleaned by soaking it in acetone and further rinsing it with isopropanol, ethanol and DI water. To remove any traces of the solvent, the wafer was dried with N_2 gas. The wafer was further placed in an ozone cleaner for 3 min to improve resist adhesion. Remaining solvents were removed by a 20-min dehydration bake at 180°C.

The cleaned wafer was then covered with the chosen photoresist, mr-DWL 5, which was applied by spin coating. 2 mL of mr-DWL 5 was added and further spinned for 33 seconds, with an acceleration of 1000 rpm/s and a maximum speed of 3000 rpm, resulting in a thickness of approximately 5.5 µm. The resist coated wafer was further pre-baked at 90°C for 2 min, by placing the wafer on a cold hotplate and gradually increasing the temperature until 90°C was reached. The temperature of the hotplate was then decreased to 50°C, and the wafer was let to cool down on the hotplate. When 50°C was reached, the wafer was moved onto a clean room wipe and let to relax for 10 min.

The substrate was exposed to UV light at 405 nm, with an exposure dose of 300-500 mJ/cm^2, using the maskless aligner MLA150. The exposure was performed following the MLA150 User Guide by Heidelberg Instruments.

After exposure, the substrate was subjected to a post-exposure bake at 90°C for 2 min. The same procedure as for the pre-bake was repeated for the post-exposure bake. The wafer was placed on a clean room wipe for a relaxation period of 1 hour.

The substrate was developed by placing the wafer in a beaker containing mrDEV-600 for 1.5-2 min under constant agitation. Fresh developer was pipetted onto the wafer surface, before incubating the wafer in a beaker with isopropanaol for 1 min. While removing the sample from the beaker, the sample was rinsed with fresh isopropanol and then dried with N_2 gas. A post bake was performed at 120-140°C for 30 min.

Replica moulding

In a 1:10 ratio, the PDMS pre-polymer Sylgard-184 (Dow Corning) was mixed with the curing agent (Dow Corning). The ratio was determined by weight, where approximately 10 g of PDMS mixture was enough for a 2" wafer. The two components were mixed by gently stirring with a plastic spoon, and the bubbles generated during stirring were removed by de-gassing in a vacuum chamber for 5-7 min. The mixture was then gently poured onto the wafer placed in a holder made by aluminum foil, and the PDMS was cured in a curing oven for 3 hours at 65°C. After curing, the PDMS stamp was carefully peeled off the wafer using tweezers.

4.7.2 Microcontact printing

A PDMS stamp produced by Kertu Liis Krigul, with a 4.6 µm thickness and features of 6 µm diameter with 12 µm spacing, was used for the microcontact printing procedure.

Microcontact printing of PLL-FITC

In order to characterize the stamp pattern, the fluorescent PLL-FITC was used to deposit the pattern onto a glass slide. Dust and other contaminants on the surface of the stamp were removed by gently attaching a piece of tape on the surface and then removing it. Depending on

the size of the PDMS stamp used, a drop of approximately 200 µL of PLL-FITC (0.5 mg/mL in MQ water) was added to the surface and let to react for about 15 min. Excess solution was pipetted off and the remaining PLL-FITC solution was removed by drying the surface with N_2 gas. A glass slide cleaned with ethanol and MQ water was placed on top of the stamp, with the pattern side facing up. The tip of a tweezers was used to gently push the glass against the tamp, so that the stamp pattern was visible by the naked eye. A weight of approximately 100 g was placed on top of the glass slide for about 15 min. The deposited pattern was investigated using the FITC filter on a Zeiss Axiobserver Z.1 microscope.

Immobilization of *S. cerevisiae* on PLL-treated glass

Since *S. cerevisiae* cells were able to attach to glass surfaces cleaned with ethanol and MQ water, the cover glasses were further treated with PEG to prevent adhesion. Cleaned glass surfaces were covered with 1 mg/mL PLL-g-PEG solution (200 µL, 60 min incubation). After incubation, excess solution was pipetted off and the slides were gently washed in MQ water and further dried with N_2 gas.

In order to verify the ability of PLL to immobilize *S. cerevisiae* cells on glass surfaces, the entire cover glass was functionalized with 0.01% PLL (200 µL, 15 min incubation). Excess solution was pipetted off and the glass slide was dried with N_2 gas. A solution of *S. cerevisiae* cells suspended in HEPES, 1:2 diluted from stock solution, was added to the slide.

Different time periods of incubation were investigated, where 5 min was established as the optimal incubation period to prevent the formation of large cell aggregates. After incubation, the slides were gently washed with MQ water. A gentle washing procedure is required, since the interaction between PLL and cells can be mechanically interrupted. Different types of washing procedures were tested, including gently moving the slide in a petri dish with MQ water, dipping the slide into MQ water and pipetting on and off MQ water on either a flat or slightly tilted glass slide. No optimal procedure was established. The immobilized *S. cerevisiae* cells were studied using a Zeiss Axiobserver Z.1 microscope, using both bright field and phase contrast. Some fresh HEPES was added to the slide surface, to prevent the cells from drying out.

Microarray of *S. cerevisiae*

The same procedure used for depositing a pattern of PLL-FITC was repeated for PLL (0.01%), which was deposited on a pegylated glass slide. Since the pattern would be more difficult to locate, due to the lack of a fluorescent tag, the stamp area was marked on the glass slide. The patterned surface was investigated using a Zeiss Axiobserver Z.1 microscope.

The PLL patterned side of the glass slide was further applied with a 200 µL solution of *S. cerevisiae* cells, 1:2 dilution of the stock solution, and incubated for 5 min, before washing with MQ to remove unattached cells. All the washing procedures mentioned above was also applied, however, no clear difference was observed. The immobilized *S. cerevisiae* cells were studied using a Zeiss Axiobserver Z.1 microscope, using both bright field and phase contrast. Some fresh HEPES was added to the slide surface to prevent the cells from drying out. Figure 4.10 demonstrates the experimental procedure for immobilization of *S. cerevisiae* on a PLL-patterned glass surface.

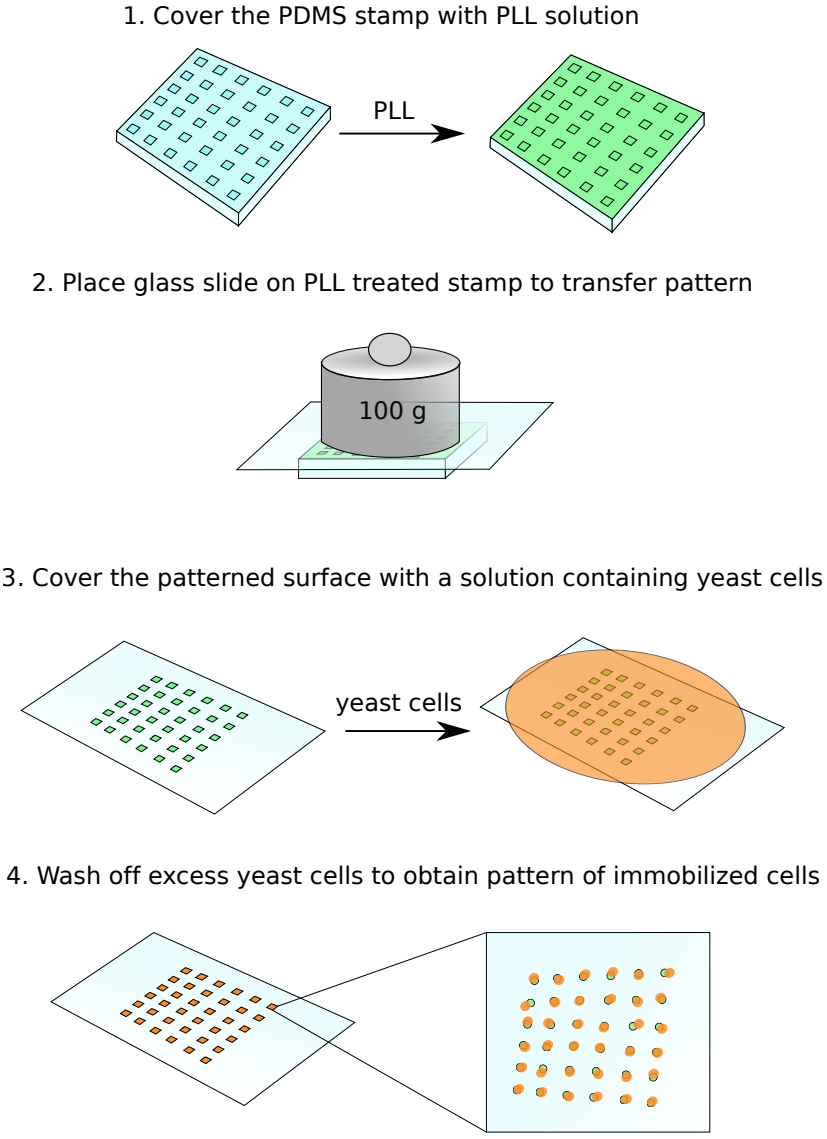

Figure 4.10: Schematic overview of the microcontact procedure for obtaining a PLL-patterned glass surface, and further immobilization of *Saccharomyces cerevisiae* cells. 1) The PDMS stamp was covered with a PLL (0.01%) solution for 15 min, before excess solution was pipetted off and the surface dried with N_2 gas. 2) A 100 g weight was positioned on top of the glass slide, in order to transfer the PLL-pattern onto the glass surface. 3) A 1:2 diluted cell suspension (in HEPES, pH 7.4) was added to the surface and let to react for 5 min at room temperature. 4) The yeast solution was removed by gently washing in MQ water. The glass surface had HEPES added to prevent the remaining cells from drying out.

5. Presentation and evaluation of results

This chapter presents the experimental data obtained as part of this master thesis, and constitutes the basis of the conclusions drawn. Some evaluation of the obtained results during the experimental work are also presented, which lead to small alterations in the experimental procedure.

5.1 Quantification of interactions between *S. cerevisiae* and fumonisin B1 by the use of shear stress flow chamber

A shear stress flow chamber was used to investigate the adhesiveness of *S. cerevisiae* cells on fumonisin B1 coated glass slides. Prior to coating the glass coupons with fumonisin B1, they were silanized in order to cover the glass slides with functional carboxyl groups. Fumonisin B1 was covalently immobilized on the coupons by the use of the coupling agent EDC. The coupling agent introduces a covalent bond between the carboxyl-group on the glass surface and the amino group on fumonisin B1 [79].

The cell suspension was injected through the injection loop and the cells were allowed to attach to the coupon surface during a 50 min waiting time, under static conditions. For the wild-type BY4741, all cells were washed away during the rinsing step. Based on this observation it was concluded that the wild-type cells were not able to adhere to the fumonisin B1 coated surface, or the carboxyl-silanized control surface. However, it was also investigated if subjecting the yeast cells to heat shock might improve their adhesiveness. The wild-type BY4741 cells were boiled in a PBS buffer for 1 hour at 80°C prior to the experiment. These heat treated cells presented improved adhesiveness, which was observed for all three replicas. The adhesiveness of viable and heat treated cells was investigated for both fumonisin B1 coated surface and carboxyl-silanized control surface. The shear stress (τ_w) required in order to detach the cells from the surface is presented in table 5.1.

Table 5.1: Shear stress calculated at the wall of the flow cell channel when 10, 50 and 90 % of the cells were washed away, denoted as $\tau_{w10\%}$, $\tau_{w50\%}$ and $\tau_{w90\%}$, respectively. The measurements were obtained in a shear stress flow chamber for viable and heat treated wild-type BY4741 cells attached to fumonisin B1 (FB1) coated glass in PBS buffer. As a control sample, shear stress was recorded for heat treated cells attached to a carboxyl-silanized surface.

	Viable cells on FB1 coated surface[1]	**Heat treated cells on FB1 coated surface**	**Heat treated cells on COOH-silanized surface**
$\tau_{w10\%}$ **(Pa)**	No adhesion	0.50 ± 0.02	0.34 ± 0.07
$\tau_{w50\%}$ **(Pa)**	No adhesion	4.14 ± 2.12	0.36 ± 0.10
$\tau_{w90\%}$ **(Pa)**	No adhesion	10.67 ± 1.08	0.37 ± 0.14

[1]No adhesion observed for viable cells on COOH-silanized surface.

For the heat treated cells, about 4% remained after the rinsing step, which constitutes the cells with successful adhesion to fumonisin B1. The detachment profile for the three replicas is presented in figure 5.1. Two of the replicas presented a similar detachment profile (light orange and orange in figure 5.1), where all cells were washed away at approximately 12 and 15 Pa of shear stress. The third replica deviated from this profile, and presented a more rapid detachment, where all cells had detached before 5 Pa of shear stress.

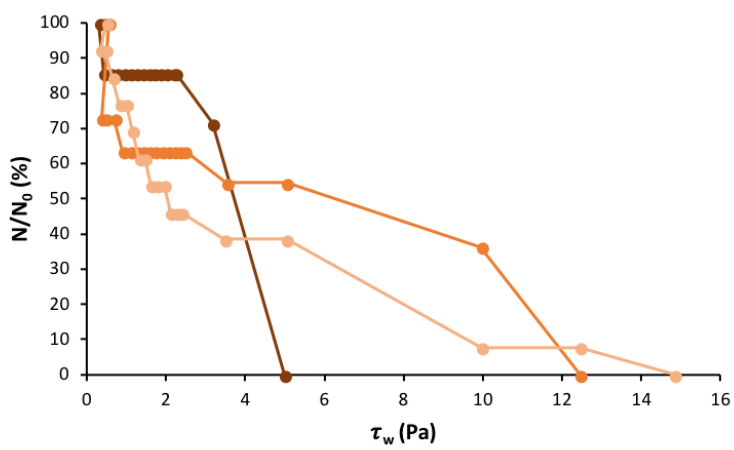

Figure 5.1: Detachment profiles of the three replicas of heat treated wild-type BY4741 cells attached to fumonisin B1 coated glass surface in PBS, induced by shear flow. About 4% of the cells remained after the rinsing step, which denoted the number of cells with successful adhesion to the fumonisin B1 coated surface and was therefore regarded as the population size (100 %) for the first measurement.

The heat treated cells also presented some ability to adhere to carboxyl-silanized glass surface, but a lower shear stress was required in order to detach all cells compared to the fumonisin B1 coated surface (table 5.1). Figure 5.2 shows images of the chosen sample area before and after

the rinsing step, for both carboxyl-silanized glass and fumonisin B1 coated glass. The number of cells present in the sample area before the rinsing step was about 200 cells. An image of the sample area was collected for every measurement, in order to count the number of cells present.

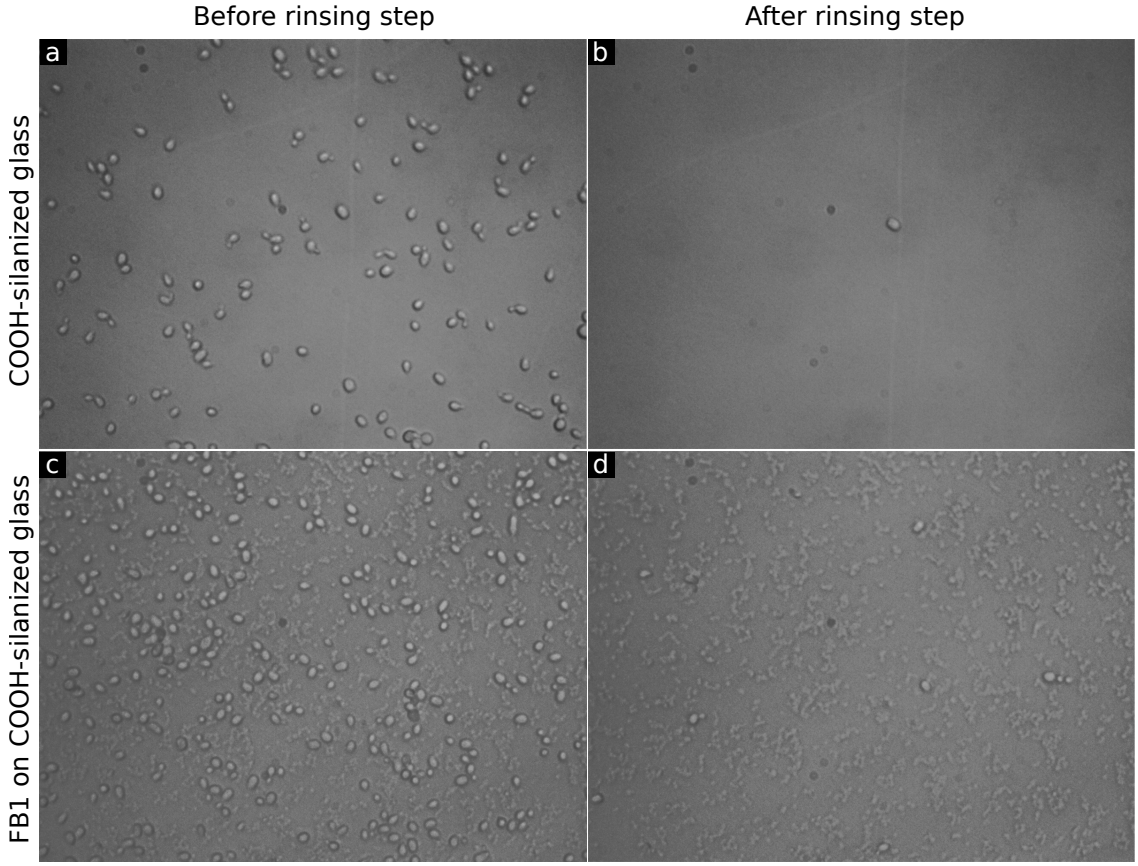

Figure 5.2: Images of chosen sample area of the coupon before and after performing the rinsing step. The number of cells present on the carboxyl-silanized glass surface, before and after rinsing, is presented in (a) and (b) respectively. The same is illustrated for the fumonisin B1 coated glass surface, in (c) and (d). Images are obtained using the optical microscope Nikon Eclipse LV100, with 40x magnification.

5.1.1 Sensitivity of the shear stress flow chamber measurements

Cleanness of the coupon

In order to achieve reliable results from the shear stress flow chamber, it is important to have a clean coupon surface. This was observed when first performing a negative control experiment with wild-type cells and an untreated glass coupon in November 2017. The coupon had been used before and was cleaned using a RBS detergent and further washed in MQ water. The results

indicated that yeast cells were able to adhere quite strongly to the untreated surface, where 193 out of 250 cells where still present after the rinsing step. A shear flow of 28 Pa was required in order to detach all cells from the glass surface. Visual inspection of the cleaned coupon, prior to the experiment, indicated the presence of contamination. This was confirmed when imaging the coupon in the optical microscope Nikon Eclipse LV100.

Due to suspected contamination of the coupon surface, a new cleaning procedure was introduced, which involved cleaning the coupon with ethanol immediately after performing an experiment. The coupon was subsequently immersed in RBS at 50°C for about 1 hour and then at room temperature overnight. The last step of the cleaning procedure involved plasma cleaning, which was performed by Cécile Formosa-Dague, LISBP, Université de Toulouse, CNRS, INRA, INSA, 31400 Toulouse, France.

The experiment with the wild-type cells and an untreated glass coupon was repeated, using a coupon cleaned with the new procedure. The obtained results differed from the first experiment, where all cells were washed away during the rinsing step. It was therefore determined that RBS was not able to remove all contamination from the coupon surface. Based on these results, previous experiments performed with a coupon washed only with RBS were excluded.

Furthermore, the new cleaning procedure enabled discrimination of the results obtained for a fumonisin B1 coated surface versus a carboxyl-silanized surface. The observed adhesion is thus believed to result from the surface coating, and not remnants of vacuum grease or other contaminants. However, some uncertainty remains regarding the ability of the improved cleaning procedure to remove all traces of functionalization from the glass surface. The possibility of contaminating vacuum grease or surface functionalization can be avoided by applying a new coupon for each experiment.

Instrumental setup

The instrumental set up of the shear stress flow chamber, demonstrated in figure 4.8, also presented some challenges regarding the reliability of the results. It was discovered that accidentally touching the tubes attached to the flow chamber induced a disturbance in the PBS that could result in detachment of the cells. This problem was mainly due to the position of the balance, located in the center of the instrumental setup. In order to reach the balance, one had to

lean over the outlet tube, which is attached to the flow cell chamber.

Such disturbance can be avoided by relocating the balance to a position were it does not interfere with the instrumental setup of the flow chamber. The measurements must be performed at precise time points, which leads to a time pressure on the researcher. Hence, the balance should be positioned close to allow rapid measurements, while reducing the stress and risk of touching the tube.

Correct estimation of the shear stress and adhesiveness of the cells were also challenging to obtain. The estimation of the shear stress is based on the amount of PBS buffer that runs through the system at a given interval in time, and calculated every 3^{rd} min. By exceeding the 3 min time period by just a couple of seconds, a larger volume of buffer is recorded than what is correct, which will further result in a higher shear stress. A correct estimation of shear stress was aimed for by carefully timing each measurement. However, an automatic registering of run through buffer would make it easier to obtain correct measurements and thus a correct estimation of the shear stress in the flow cell.

For each measurement, the number of cells present in the sample area had to be counted manually, which was a time consuming process. The number of cells could be obtained using a MATLAB program, which can count the number of cells in the recorded images. However, it is important to distinguish cells that have moved and reattached within the sample area from those that were able to maintain their initial position throughout the measurements. Furthermore, cells that were initially part of aggregates prior to the rinsing step were not registered, and should not be included if they were represented as single cells later in the experiment. It was also observed that cells from other locations on the coupon surface could reattach within the sample area. Such cells should not be recorded. However, keeping track of these cells during the measurements was experimentally challenging. Identifying such occurrences was not possible for the available MATLAB program, and thus the recording of cells present in the sample area was concluded to be more accurately determined when performed manually.

Distribution of fumonisin B1 on the coupon surface

Another factor that might impact the reliability of the results is the distribution of fumonisin B1 on the coupon surface. A homogenous coverage of fumonisin B1 is favorable in order to ob-

tain equal conditions for each measurement. A concentration of 0.25 mg/mL fumonisin B1 was found to provide a sufficient coverage. However, some aggregates were observed, as demonstrated in figure 5.3.

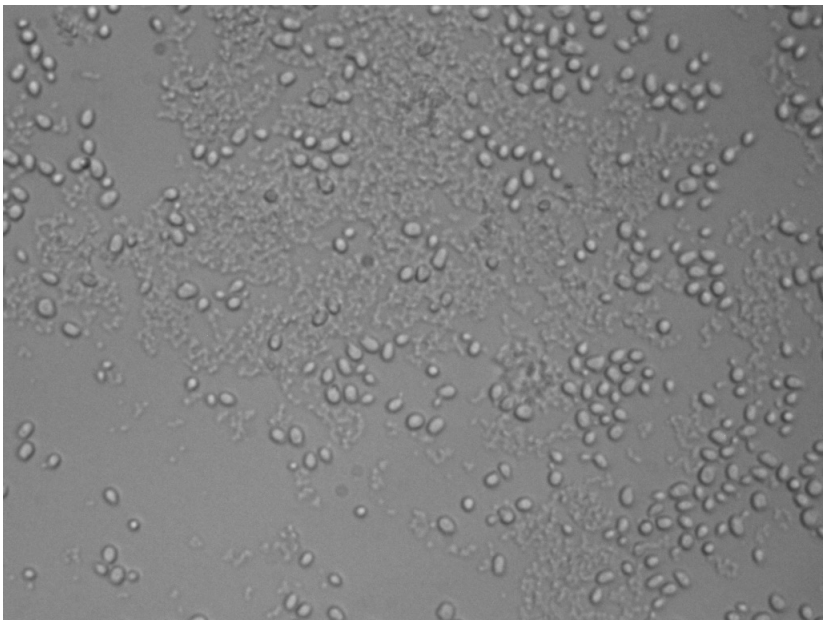

Figure 5.3: Demonstration of uneven coverage of fumonisin B1 on carboxyl-silanized glass surface used for shear stress flow chamber experiments. The image is captured before performing the rinsing step. Image is obtained using an optical microscope Nikon Eclipse LV100, with 40x magnification.

5.1.2 AFM height images of fumonisin B1 coated glass

The distribution of fumonisin B1 on the glass coupon was investigated by the use of AFM imaging. The surface topography of the glass coupon was characterized using tapping mode AFM. This procedure was performed by Nina Bjørk Arnfinnsdottir (Institute of Physics, NTNU). Glass slides with covalently immobilized fumonisin B1 were compared with glass slides where fumonisin B1 had been adsorbed on the surface (figure 5.4). AFM images of glass with adsorbed fumonisin B1 illustrated areas with a homogenous coverage (c and d), but also areas with aggregates (b) and empty spots (a). The surfaces with covalently immobilized fumonisin B1 generally showed a homogenous coverage (e), but included some areas showing aggregates present on top of the fumonisin B1 film (f).

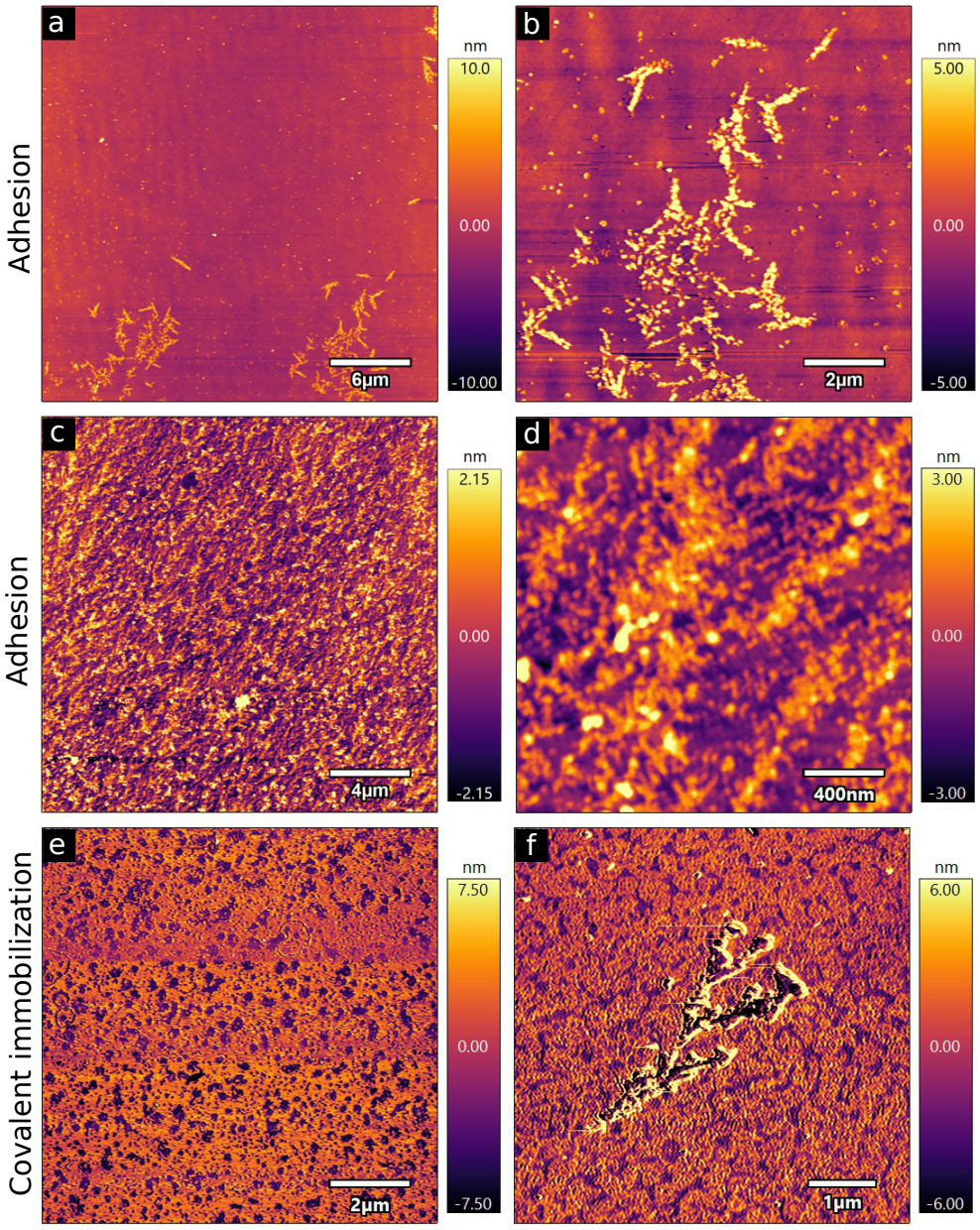

Figure 5.4: AFM height images of fumonisin B1 adsorbed (a-d) or covalently immobilized (e-f) on glass slides. The images were recorded by the use of tapping mode.

In order to compare the topography of the adsorbed and covalently immobilized fumonisin B1 covered glass slides, the surface roughness (R_a) was calculated for each of the images presented in figure 5.4. The obtained value is the mean surface roughness calculated for the entire image. In figure 5.4a, there are some regions with aggregates, but also areas without any visible fumonisin B1. By the use of the mask function in the IGOR pro software, the surface roughness was calculated for the region without any visible fumonisin B1 (figure 5.5i). The same procedure

was repeated for figure 5.4f, and the chosen region for determination of the surface roughness is illustrated in figure 5.5ii.

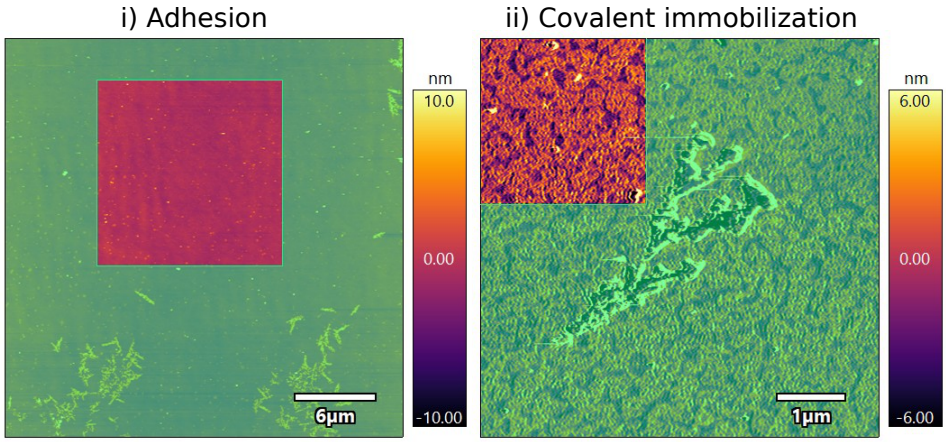

Figure 5.5: Marked region of AFM height images of fumonisin B1 adsorbed (i) or covalently immobilized (ii) on glass, for determination of surface roughness

The obtained R_a values for figures 5.4 and 5.5 are presented in table 5.2, as well as the measured R_a for a clean glass slide. The R_a values obtained for the glass slides with adsorbed fumonisin B1 were lower than the ones obtained for fumonisin B1 covalently immobilized on glass. The marked region (i) in figure 5.5 had a lower surface roughness than the entire image (figure 5.4a). This was also observed for the marked region (ii) of image f in figure 5.4.

Table 5.2: Surface roughness (R_a) of the AFM height images of a clean glass slide and fumonisin B1 adsorbed or covalently immobilized on glass presented in figure 5.4, as well as the marked region in figure 5.5.

	Sample[1]	**R_a (nm)**
Clean glass	-	0.597
FB1 adsorbed on glass	a	1.242
	b	1.640
	c	1.155
	d	1.142
	i	0.745
FB1 covalently immobilized on glass	e	3.203
	f	3.127
	ii	2.394

[1]The letters refer to the different images included in figure 5.4 and 5.5

The obtained results presented a more even coverage of fumonisin B1 when it was covalently

immobilized on the glass compared to only adhesion of the fumonisin B1 molecules (figure 5.4). Based on the roughness values of the glass surfaces, it can be concluded that fumonisin B1 can successfully adhere to glass, as well as be covalently immobilized to carboxyl-silane using EDC. However, covalently immobilizing fumonisin B1 on the surface seems to be a better option than adhesion, due to a more even coverage and a stronger attachment to the glass. Applying glass with fumonisin B1 adsorbed to the surface might risk the removal of the fumonisin B1 molecules during the experiments, due to the weak interaction with the glass surface.

5.2 Quantification of interactions between *S. cerevisiae* and fumonisin B1 by the use of optical tweezers

The ability of *S. cerevisiae* cells to interact with the mycotoxin fumonisin B1 was also investigated using the dual beam optical tweezers. Both the wild-type BY4741 and the mutant Δmnn9 strains of *S. cerevisiae* were studied. Furthermore, the two strains were subjected to a protease treatment and heat shock to investigate if this improved their adhesiveness. The molecular mechanism behind the interaction was investigated by coating polystyrene beads with the cell wall components β-glucan and mannan. The adhesiveness of the polysaccharide-coated beads with fumonisin-coated beads was examined, and the obtained results are presented in section 5.2.2.

5.2.1 Interaction capacity of different strains of *S. cerevisiae* and the effect of treatments affecting the cell wall structure

Fumonisin B1 was tested against viable wild-type BY4741 and genetically modified Δmnn9 cells of *S. cerevisiae*. The Δmnn9 mutant strain possesses a defect in the synthesis of mannan, resulting in aberrations in the cell wall structure. This altered cell wall composition should result in more exposed cell wall proteins, as well as increased access to the β-glucan layer, which is hypothesized to participate in an interaction with fumonisin B1. Neither strains were able to interact with fumonisin B1.

Wild-type and Δmnn9 were further subjected to a protease treatment, in order to reduce the mannose peptides in the cell wall. This protease mixture from *Streptomyces griseus* is highly

nonspecific, but prefers to hydrolyze peptide bonds on the carboxyl side of glutamic or aspartic acids (Product Information from Sigma-Aldrich). This could improve the access to the β-glucan layer and thus promote the ability to interact with fumonisin B1. The first experiment with protease treated cells was performed in June 2017, where the cells were incubated with the protease for 2 hours. However, the protease treatment demonstrated no visible effect on the frequency of interactions. The experiment was repeated in March 2018, with a much longer incubation period, of 6 hours. The increased incubation time did not influence the interaction capacity.

The wild-type cells were also subjected to heat shock by boiling the cells in a buffer for 1 hour at 80 °C. The heat shock was hypothesized to induce a change in the cell wall structure which would result in access to binding sites for fumonisin B1. The treatment did result in visible interaction with fumonisin B1, where about 29 % of the curves obtained interactions when fumonisin B1 was immobilized on amino beads. The heat treated cells were able to interact with amino and carboxyl beads, both with and without immobilized fumonisin B1.

An overview of the ability of *S.cerevisiae* cells to interact with fumonisin B1, as well as the effect of the two treatments, is presented in table 5.3. The frequency of interaction for heat treated cells and fumonisin B1, as well as the corresponding negative controls, are presented in figure 5.6.

Table 5.3: The ability of *S. cerevisiae* cells to interact with fumonisin B1 (FB1). Fumonisin B1 was immobilized on either amino- or carboxyl-functionalized polystyrene beads for the experiments. Therefore, the interaction capacity between yeast cells and untreated amino- and carboxyl-functionalized beads was investigated as a negative control.

	COOH beads	**FB1 on COOH beads**	**NH_2 beads**	**FB1 on NH_2 beads**
Heat treated WT cells	YES	YES	YES	YES
Untreated WT cells	NO	NO	NO	NO
Δmnn9 cells	NO	NO	NO	NO
Protease treated WT cells	NO	NO	NO	NO
Protease treated Δmnn9 cells	NO	NO	NO	NO

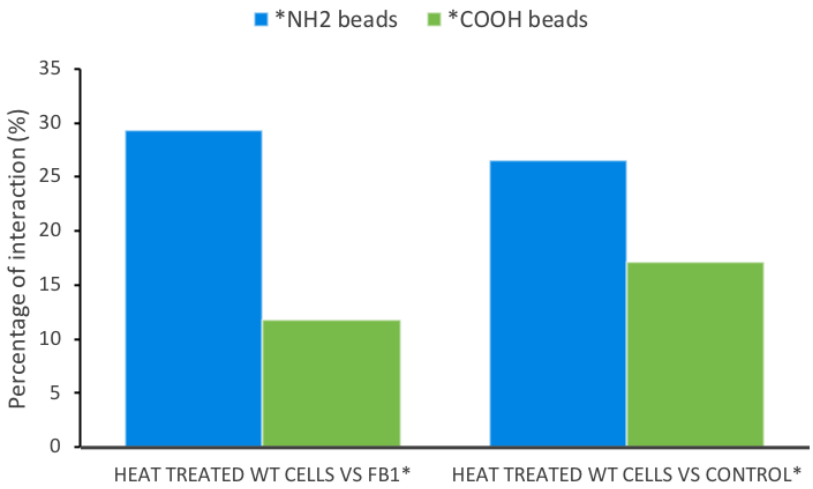

Figure 5.6: Frequency of interaction for heat treated wild-type (WT) *S. cerevisiae* cells and fumonisin B1 (FB1) on either amino- or carboxyl-beads, as well as the corresponding negative controls.
*Functionalization of the bead: amino or carboxyl.

The frequency of interaction for fumonisin B1 immobilized on amino beads was more than two times higher compared to fumonisin B1 immobilized on carboxyl beads. However, the interaction between heat treated cells and untreated amino beads was almost the same as for fumonisin B1 treated amino beads, 29 and 27% respectively. For the untreated carboxyl beads 17% of the curves obtained interactions, while the fumonisin B1 treated carboxyl beads displayed an interaction frequency of about 12%.

In order to elaborate on the role of fumonisin B1 in the interaction with heat treated cells, the force curves were analyzed using the IDL program described in section 4.4.4. The generated data of rupture force and loading rate for each recorded interaction was further used to compare the dynamic power spectra of the different interactions. Some of the force curves are also presented to demonstrate the typical shape of the curves observed for the different interactions.

Interactions between heat treated wild-type *S. cerevisiae* cells and fumonisin B1 on carboxyl-functionalized beads

The force curves of the interaction between heat treated cells and fumonisin B1 on carboxyl-beads presented a linear increase in force with low level of background noise, as demonstrated by the examples in figure 5.7. For the interaction between heat treated cells and uncoated carboxyl-beads, some of the curves had a similar shape to those obtained for fumonisin B1-

coated beads (figure 5.7c). Whereas other curves presented a more convex or horizontal curve, as demonstrated in figure 5.7d.

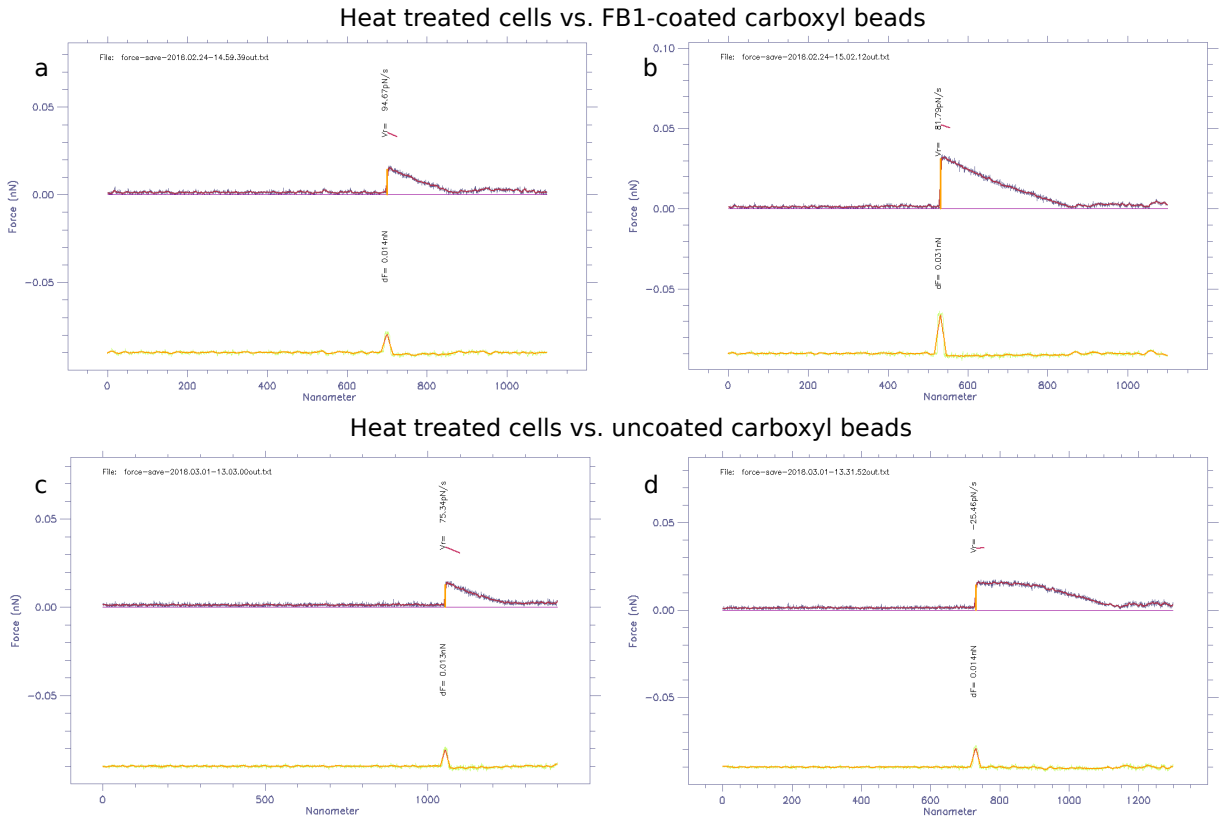

Figure 5.7: Examples of force curves obtained for the interactions between heat treated wild-type *S. cerevisiae* cells and (a,b) fumonisin B1 (FB1) coated or (c,d) uncoated carboxyl-functionalized polystyrene beads. The loading rate has not been fitted for the presented force curves.

A histogram of the distribution of unbinding forces between heat treated wild-type BY4741 cells and fumonisin B1 on carboxyl beads was made based on data gathered in February 2018 (figure 5.8). The distribution is based on 130 data points. A fit of the Bell-Evans curve (equation 3.16) yields the value of the most probable unbinding force (f^*) as the peak of the curve. The interaction between heat treated cells and fumonisin B1 on carboxyl beads resulted in measurements with a rupture force up to 70 pN.

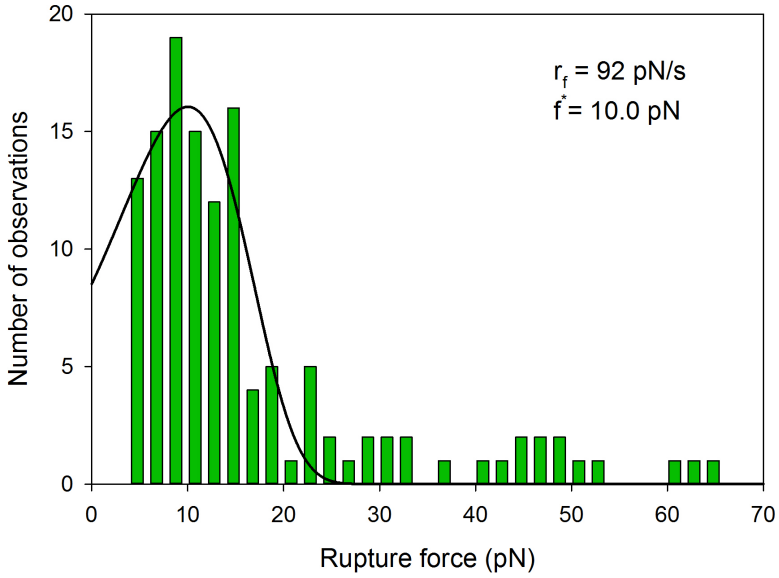

Figure 5.8: Histogram demonstrating the distribution of rupture forces between heat treated wild-type *S. cerevisiae* cells and fumonisin B1 on carboxyl beads (2.10 µm). The histogram is based on 130 data points.

The dynamic force spectrum of the interaction between heat treated cells and fumonisin B1 is presented together with the dynamic force spectrum of the interactions between heat treated cells and untreated carboxyl beads (figure 5.9). Both spectra were obtained using 2.10 µm carboxyl beads. The interactions with fumonisin B1 and untreated carboxyl beads are based on 130 and 184 data points, respectively. The two data sets presented a similar dynamic force spectrum.

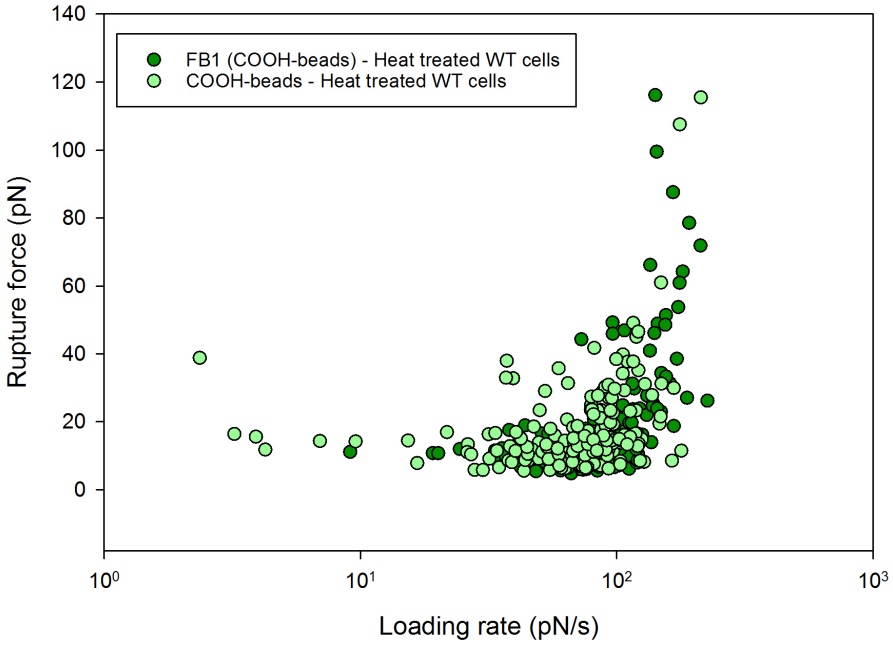

Figure 5.9: A comparison of the dynamic force spectra of heat treated wild-type (WT) *S. cerevisiae* cells - fumonisin B1 (FB1) on carboxyl beads, and heat treated cells - untreated carboxyl beads. Both sets of spectra were obtained using 2.10 µm beads, and are based on 130 and 184 data points for the interactions with FB1 and untreated carboxyl beads, respectively.

Interactions between heat treated wild-type BY4741 yeast cells and fumonisin B1 on amino-functionalized beads

Force curves obtained for the interaction between heat treated cells and fumonisin B1 on amino-beads presented a long and gradual increase in force before the force jump, as demonstrated by the force curves presented in figure 5.10. The same shape was also observed for the interaction with uncoated amino-beads. However, some of the curves presented a higher level of background noise (figure 5.10c).

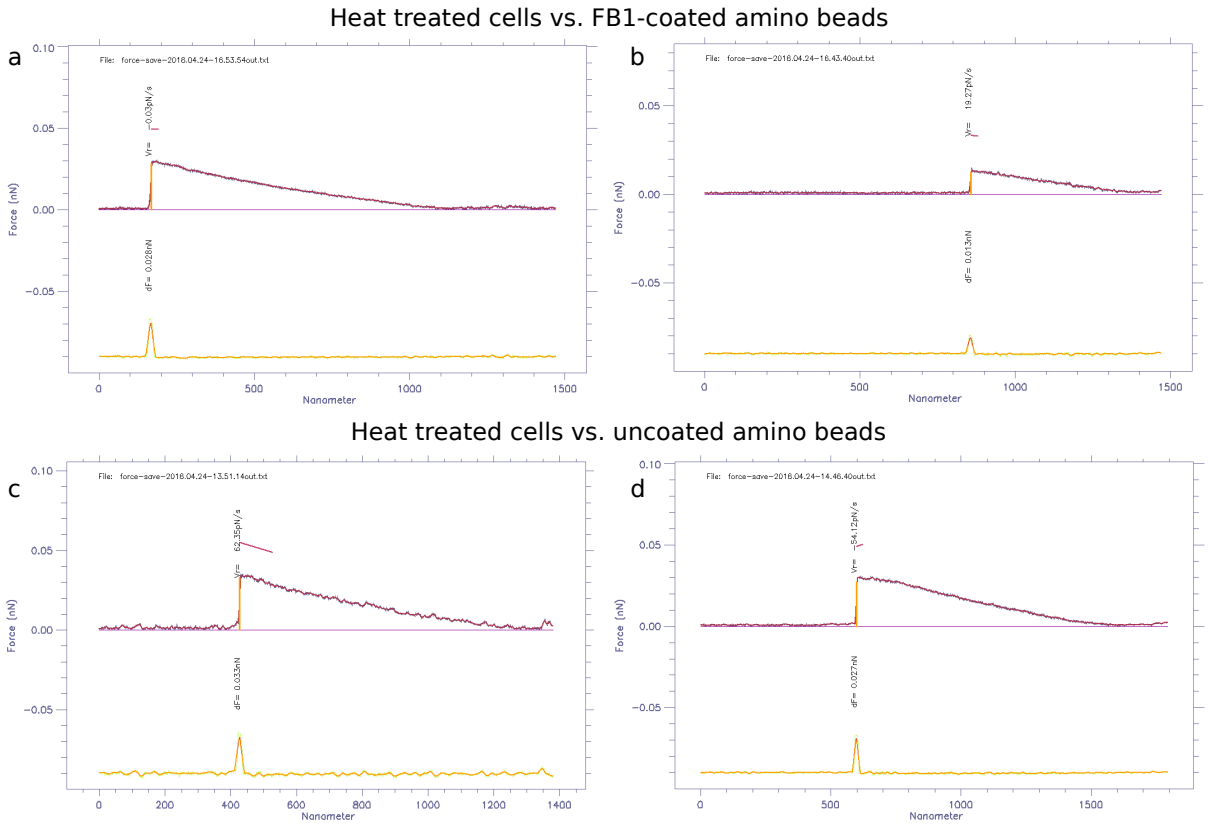

Figure 5.10: Examples of force curves obtained for the interactions between heat treated wild-type *S. cerevisiae* cells and (a,b) fumonisin B1 (FB1) coated or (c,d) uncoated amino-functionalized polystyrene beads. The loading rate has not been fitted for the presented force curves.

The interaction between heat treated wild-type BY4741 cells and fumonisin B1 on amino beads was illustrated in two histograms, which are obtained for rupture forces in two sub-distributions of loading rate (figure 5.11). The two sub-distributions were generated based on a total of 174 data points gathered in April 2018. A fit of the Bell-Evans curve (equation 3.16) yields the value of the most probable unbinding force (f^*), determined based on the maximum in the histogram distribution. The histogram located to the left in figure 5.11 is based on the data points in the lower region of the loading rate. Due to the shape of this distribution, a good Bell-Evans fit was not obtained, resulting in a unrealistically low f^* value. The histogram located to the right in figure 5.11 is based on the data points of higher loading rate. Also for this distribution it was challenging to obtain a good fit of equation 3.16, and the f^* determined based on the fitting procedure appears unrealistically low. None of the two sub-distributions presented rupture forces above 30 pN.

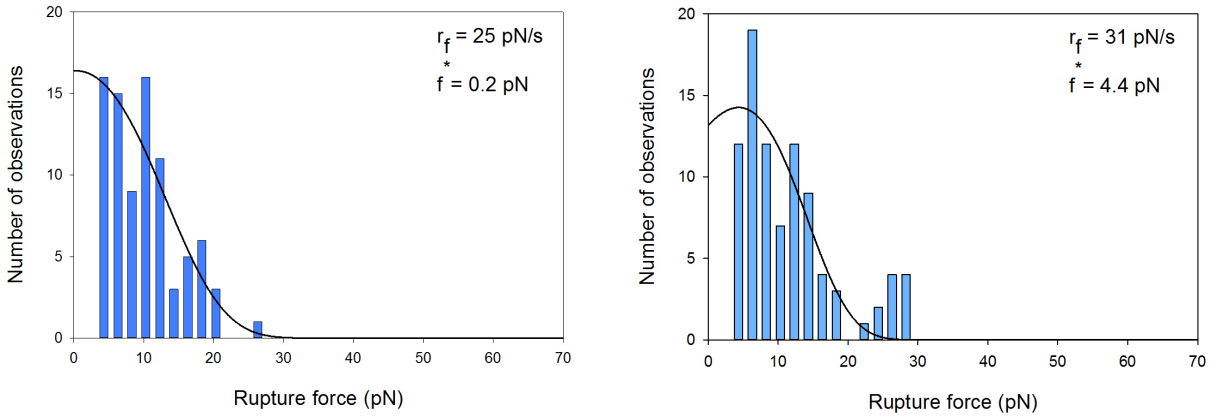

Figure 5.11: Histograms obtained for rupture forces in two sub-distributions of loading rate, for interactions between heat treated wild-type *S. cerevisiae* cells and fumonisin B1 on amino beads (2.18 µm). The two sub-distribution is based on 85 and 89 data points, respectively.

The dynamic force spectrum of the interaction between heat treated cells and fumonisin B1 is presented together with the dynamic force spectrum of the interactions between heat treated cells and untreated amino beads (figure 5.12). Both spectra were obtained using 2.18 µm amino-functionalized beads. The dynamic power spectra showed that the interactions for heat treated cells - fumonisin B1 on amino beads were generally of lower strength and obtained at lower loading rate than the interactions with untreated amino beads. The data points for the fumonisin B1 interactions were also mostly concentrated in the lower region of loading force, while the untreated amino beads generated more scattered data points, also in the higher regions of loading rate. The interactions with FB1 and untreated amino beads are based on 174 and 164 data points, respectively.

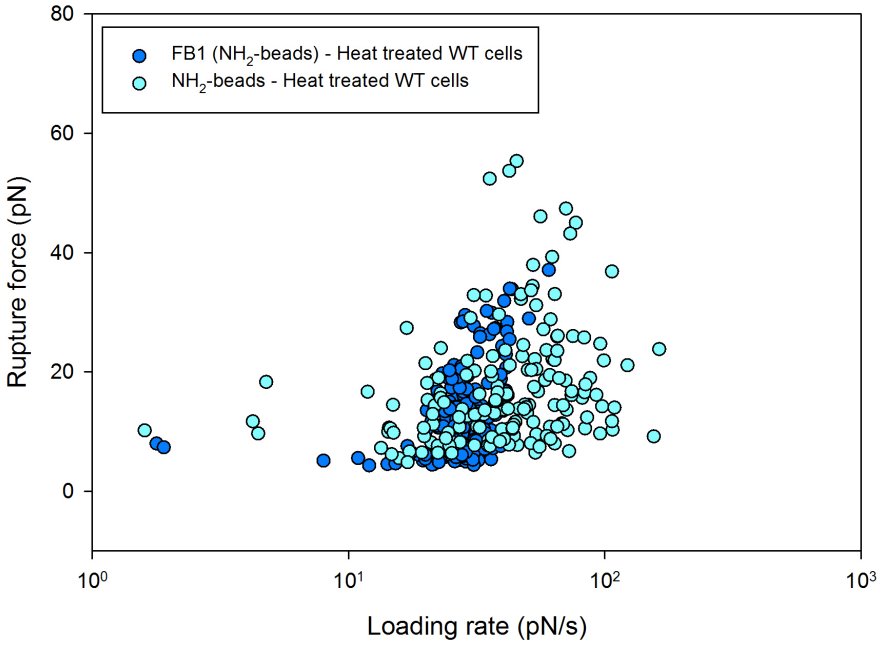

Figure 5.12: Dynamic power spectra for the interactions between heat treated wild-type (WT) *S. cerevisiae* cells and fumonisin B1 (FB1) on amino beads, as well as the interactions with untreated amino beads as a negative control. Both sets of spectra were obtained using 2.18 µm beads, and are based on 174 and 164 data points for the interactions with FB1 and untreated amino beads, respectively.

Dynamic force spectrum for heat treated cells and fumonisin B1 interactions is presented in figure 5.13. The spectra obtained by fumonisin B1 immobilized on amino beads is compared with the spectra of fumonisin B1 on carboxyl beads. When fumonisin B1 was immobilized on amino beads, the interactions with heat treated cells resulted in force curves with a rupture force in the range of 0-40 pN. The data points are also located in the lower region of loading rate compared to what is observed for fumonisin B1 immobilized on carboxyl beads. The interactions for the carboxyl beads generated data points with higher loading rates, as well as rupture forces as high as 120 pN. The data sets were obtained using 2.10 µm carboxyl beads and 2.18 µm amino beads, and are based on 130 and 174 data points, respectively.

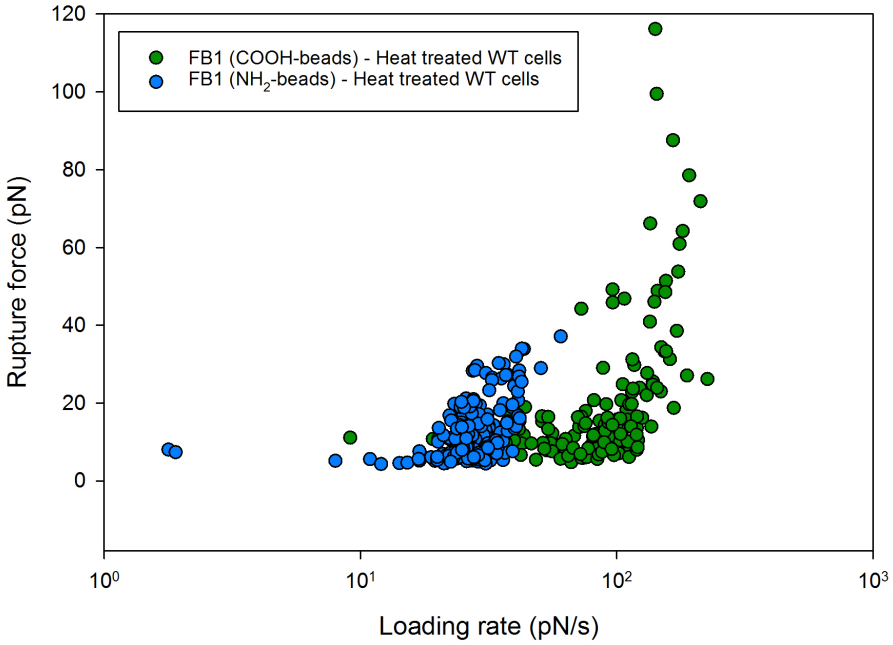

Figure 5.13: A comparison of the dynamic power spectra of heat treated wild-type *S. cerevisiae* cells and fumonisin B1 on either amino- or carboxyl-beads.

5.2.2 Interactions between the cell wall components of *S. cerevisiae* and fumonisin B1

To elaborate on which component in the cell wall of *S. cerevisiae* that was able to interact with fumonisin B1, both mannan and β-glucan were immobilized on polystyrene beads. For the first experiments, mannan and β-glucan was subjected to a reductive amination process, which should introduce an amino-group at the reducing end of the polysaccharides. The modified polysaccharides could then be covalently attached to carboxyl beads by the coupling agent EDC. However, the reductive amination process failed due to the lack of an amine donor. As a result, these beads were assumed to not contain any polysaccharides on the surface and the experiments performed with these beads were excluded. The reductive amination process was repeated with amino-functionalized beads (3.36 µm) acting as the amine donor, as described in section 4.3.1.

When investigating the interaction capacity between mannan and fumonisin B1, less than 5% of the curves contained signatures of the rupture of intermolecular interactions. This was

observed for the interactions with fumonisin B1 immobilized on both amino and carboxyl beads, as well as for untreated beads. On the other hand, β-glucan presented a frequency of interaction equal to about 16% when fumonisin B1 was immobilized on amino beads. However, the control experiments showed that β-glucan coated beads were also able to interact with untreated amino-functionalized beads, where 6% of the curves obtained interaction. The frequency of interaction for the cell wall components with fumonisin B1, as well as the corresponding negative controls are presented in figure 5.14.

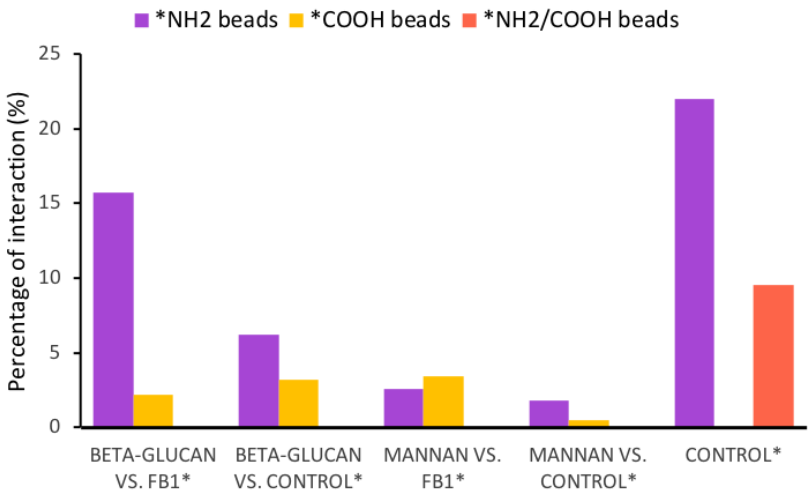

Figure 5.14: Frequency of interactions for the cell wall components of *S. cerevisiae* with fumonisin B1, immobilized on either amino- or carboxyl-functionalized polystyrene beads. The frequency of interaction is also stated for the corresponding negative controls, consisting of self-interaction between amino beads and the interaction between uncoated amino- and carboxyl beads.
*Functionalization of the bead: amino or carboxyl.

Due to the low frequency of interaction observed between mannan and fumonisin, it was decided to further focus on the interaction between β-glucan and fumonisin B1, which presented more promising results.

Interactions between β-glucan and fumonisin B1 on carboxyl-functionalized beads

The force curves of the interaction between β-glucan and fumonisin B1 on carboxyl-beads presented a linear increase in force with some level of background noise, as demonstrated by the examples in figure 5.15. For the interaction between β-glucan and uncoated carboxyl-beads, the force curves presented a similar shape to those obtained for fumonisin B1-coated beads.

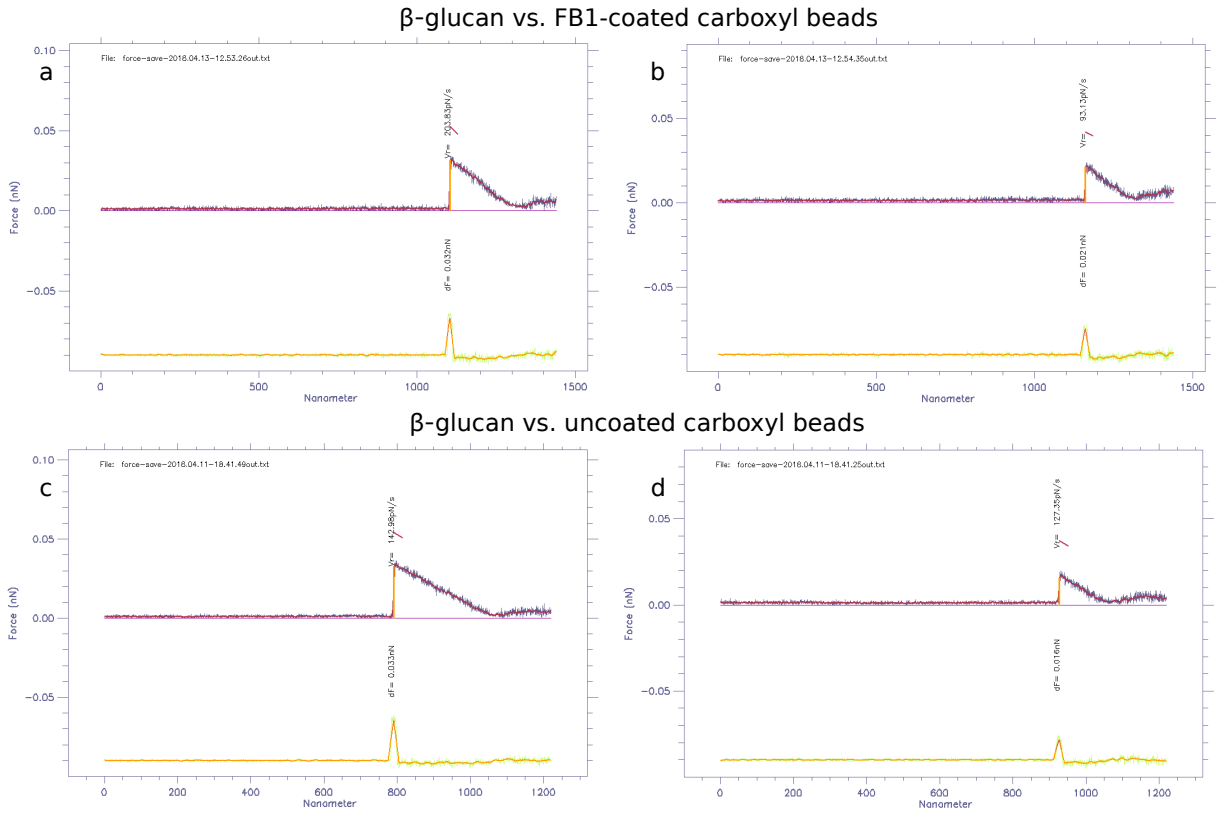

Figure 5.15: Examples of force curves obtained for the interactions between the cell wall component β-glucan and (a,b) fumonisin B1 (FB1) coated or (c,d) uncoated carboxyl-functionalized polystyrene beads. The loading rate has not been fitted for the presented force curves.

A histogram of the distribution of rupture forces for β-glucan and fumonisin B1 on carboxyl-functionalized beads (2.10 µm) was made based on the 13 data points gathered in April 2018 (figure 5.16). A fit of the Bell-Evans curve (equation 3.16) yields the value of the most probable unbinding force (f^*) as the peak of the curve. Due to the small data set, a good Bell-Evans analysis was difficult to obtain. However, the calculated f^* value of 22.7 pN seems to be located in the centre of the distribution, and thus is believed to be accurate.

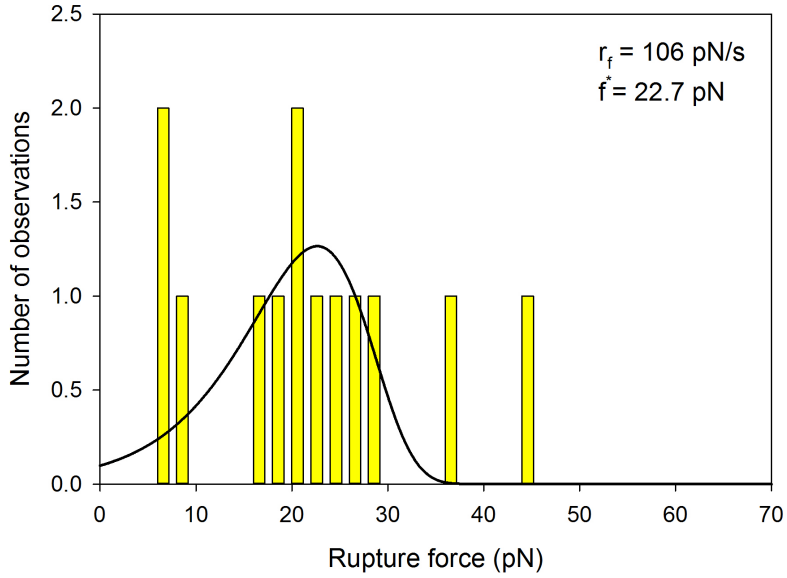

Figure 5.16: Histogram demonstrating the distribution of unbinding forces between the cell wall component β-glucan and fumonisin B1 on carboxyl-beads (2.10 µm), based on 13 data points. β-glucan was immobilized on 3.36 µm amino beads.

The dynamic force spectrum of the interaction between β-glucan and fumonisin B1 was presented together with the dynamic force spectrum of the interactions between β-glucan and untreated carboxyl beads (figure 5.17). Fumonisin B1 was immobilized on 2.10 µm carboxyl beads, and the same size was applied for the negative control. Both the dynamic force spectra for fumonisin B1-coated beads and untreated carboxyl beads are based on very few data points, 13 and 21 respectively, rendering it difficult to evaluate the distribution of rupture force.

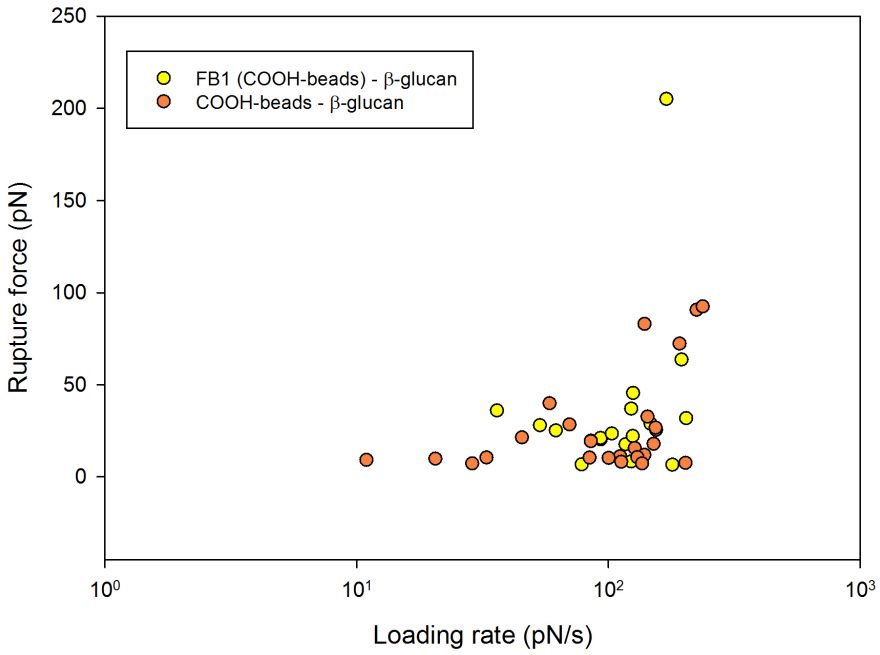

Figure 5.17: A comparison of the dynamic power spectra for the cell wall component β-glucan - fumonisin B1 (FB1) on carboxyl beads, and β-glucan - untreated carboxyl beads. Both sets of spectra were obtained using 2.10 µm carboxyl beads, and β-glucan was immobilized on 3.36 µm amino beads. The dynamic power spectra are based on 13 and 21 data points for the FB1-treated and untreated carboxyl beads, respectively.

Interactions between β-glucan and fumonisin B1 on amino-functionalized beads

The force curves obtained for the interaction between β-glucan and fumonisin B1 on amino-beads presented a rapid and linear increase in force before the force jump, as demonstrated in figure 5.18. The curve in figure 5.18a demonstrates a slightly jagged curve, which might indicate multiple interactions. A rapid and linear increase in force was also observed for the force curves obtained for the interaction with uncoated amino-functionalized beads. However, some of these curves presented a higher level of background noise (figure 5.18d).

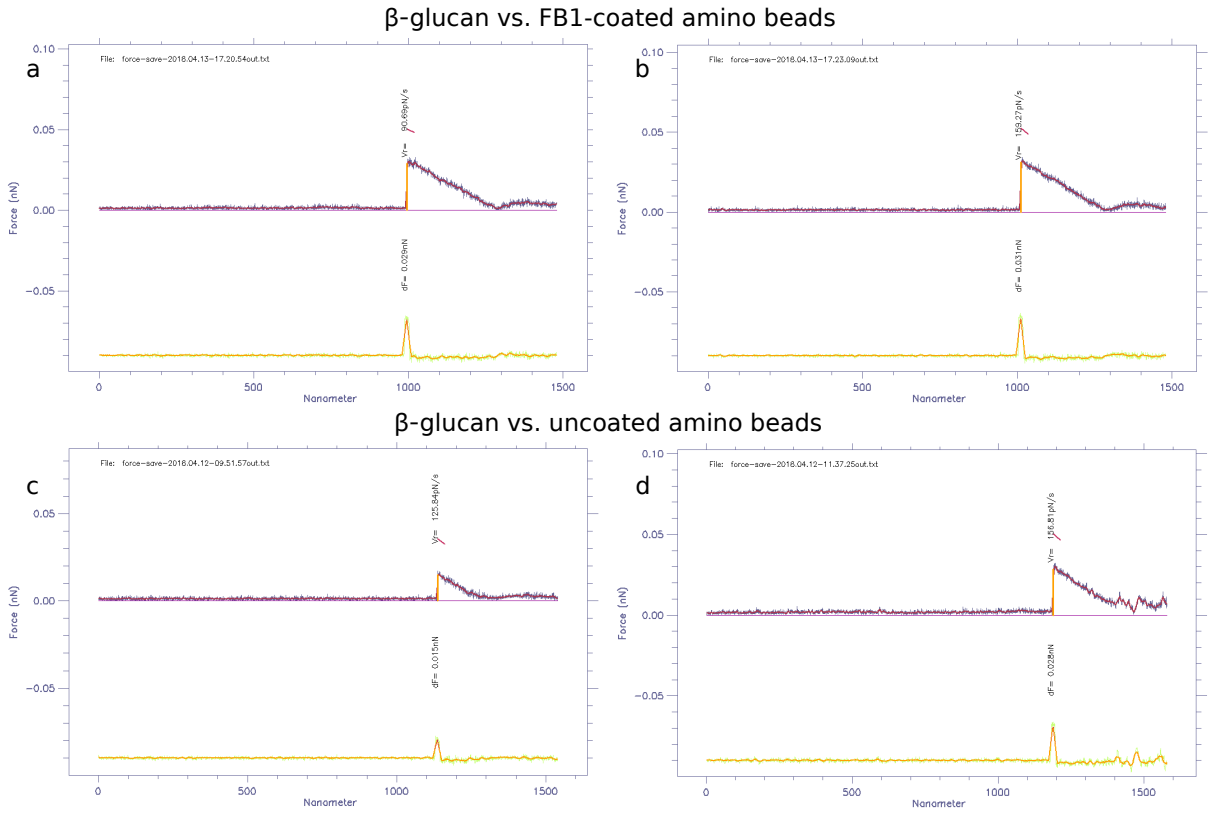

Figure 5.18: Examples of force curves obtained for the interactions between the cell wall component β-glucan and (a,b) fumonisin B1 (FB1) coated or (c,d) uncoated amino-functionalized polystyrene beads. The loading rate has not been fitted for the presented force curves.

A histogram of the distribution of rupture forces for β-glucan and fumonisin B1 on amino-functionalized beads (2.18 µm) was made based on the 118 data points gathered in April 2018 (figure 5.19). A fit of the Bell-Evans curve (equation 3.16) yields the value of the most probable unbinding force (f^*) as the peak of the curve. A large number of interactions creates a better foundation for achieving a good Bell-Evans analysis, and the generated curve corresponds well to the distribution of rupture forces. When fumonisin B1 was immobilized on amino beads, it was able to generate interactions with β-glucan with a strength up to 70 pN.

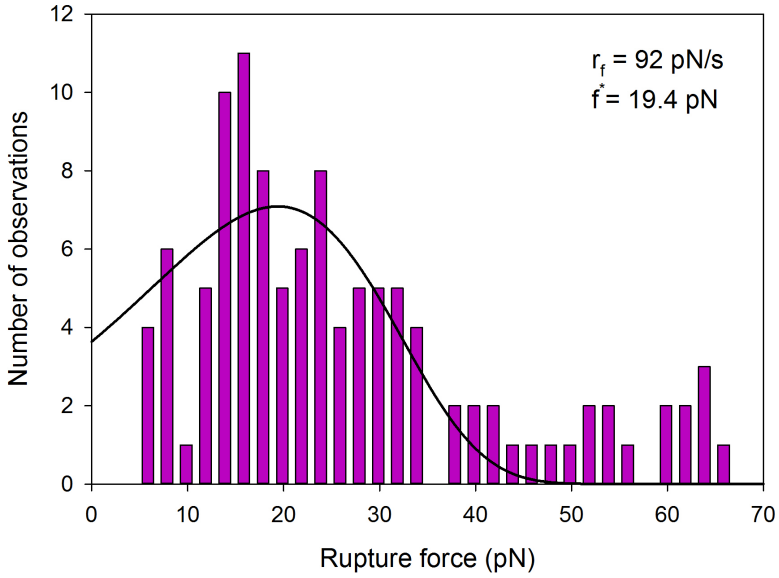

Figure 5.19: Distribution of unbinding forces between the cell wall component β-glucan and fumonisin B1 on amino beads (2.18 µm), based on 118 data points. β-glucan was immobilized on 3.36 µm amino beads.

The dynamic force spectrum of the interaction between β-glucan and fumonisin B1 was presented together with the dynamic force spectrum of the interactions between β-glucan and untreated amino beads (figure 5.20). Fumonisin B1 was immobilized on 2.18 µm amino beads, and the same size was applied for the negative control. The dynamic power spectra are based on 118 and 47 data points for fumonisin B1-coated beads and untreated amino beads, respectively. The dynamic power spectra illustrates that the interaction between β-glucan and fumonisin B1 coated amino beads generally generated rupture forces of higher strength than the interactions observed for untreated amino beads.

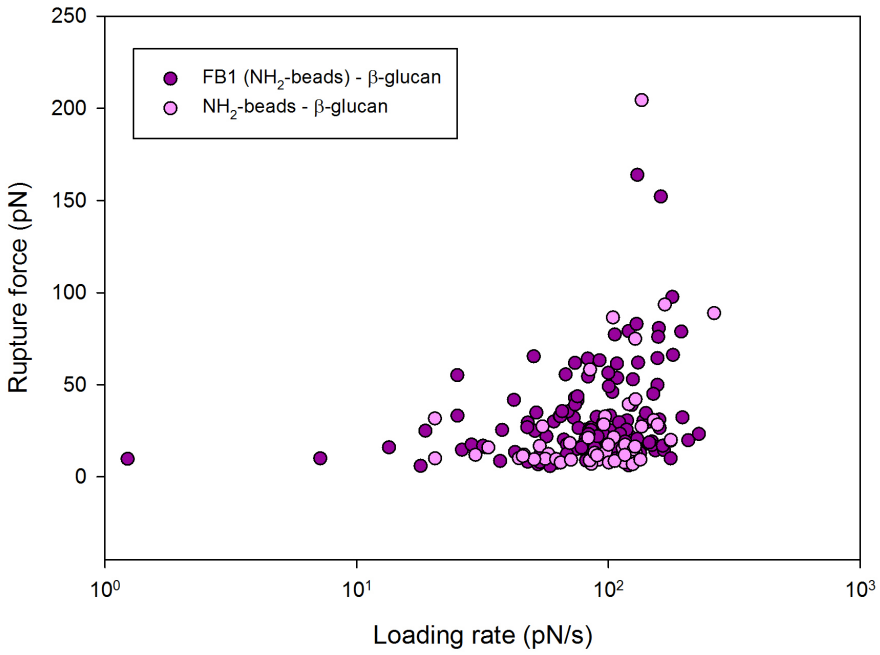

Figure 5.20: Dynamic power spectra for the interactions between the cell wall component β-gluan and fumonisin B1 (FB1) on amino beads, as well as the interactions with untreated amino beads as a negative control. Both sets of spectra were obtained using 3.36 and 2.18 µm amino beads, for β-glucan and FB1 respectively. The dynamic power spectra are based on 118 data points for the interactions with FB1 and 47 data points for the interactions with untreated beads.

Untreated amino-functionalized beads presented the ability to self-interact, where about 25% of the curves obtained interactions. The force curves presented a rapid and linear increase in force before the force jump figure 5.21). The curves had varying shapes, such as jagged curves and high levels of background noise.

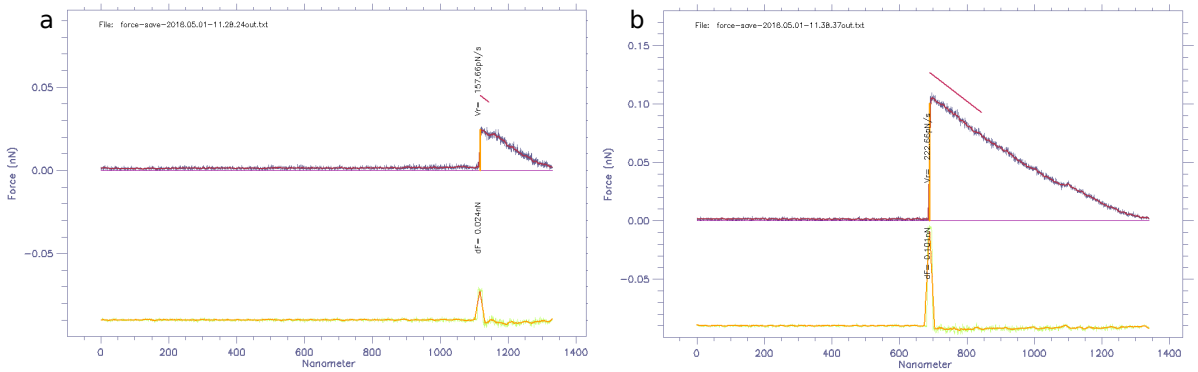

Figure 5.21: Examples of force curves obtained for the self-interaction between uncoated amino-functionalized beads.

In order to differentiate the interaction between untreated amino beads from the interaction between β-glucan and fumonisin B1, their respective dynamic power spectrum were presented together in figure 5.22. Both spectra presented rupture forces up to 200 pN, while the untreated amino beads displayed a few data points with even higher force, up to 400 pN. The investigation of the interactions between untreated amino-functionalized beads was performed using 2.18, 3.12 and 3.36 µm beads. Measurements were performed on bead pairs of equally sized beads, as well as for beads of different size. β-glucan and fumonisin B1 were immobilized on 3.36 and 2.18 µm sized amino beads, respectively, for all measurements.

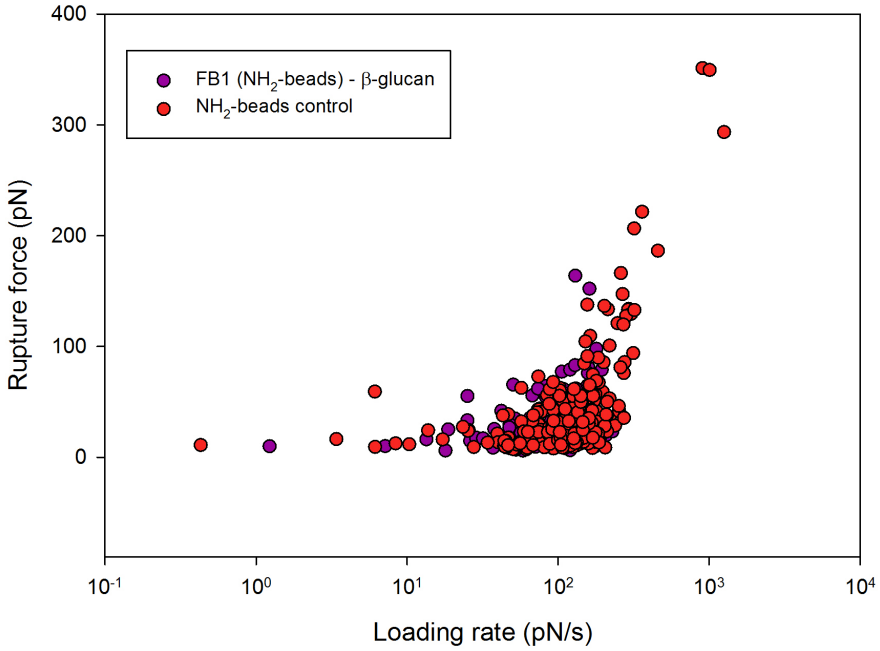

Figure 5.22: Dynamic power spectrum for the interactions between β-glucan and fumonisin B1, both immobilized on amino beads, compared with the dynamic power spectrum of interactions between untreated amino beads. The dynamic power spectra are based on 118 data points for the β-glucan - FB1 interactions and 342 for interactions between untreated amino beads.

The effect of fumonisin B1 immobilized on amino- or carboxyl beads

A dynamic force spectrum for β-glucan and fumonisin B1 interactions is presented in figure 5.23. The dynamic force spectrum compares the spectrum obtained by fumonisin immobilized on amino beads with the spectrum of fumonisin on carboxyl beads. The data sets were obtained using 2.10 µm carboxyl beads and 2.18 µm amino beads for immobilization of fumonisin B1,

and are based on 13 and 118 data points, respectively. Due to the small amount of available data points for the interactions with fumonisin B1 on carboxyl beads, the corresponding dynamic force spectrum does not provide sufficient information concerning the shape of the dynamic force spectra.

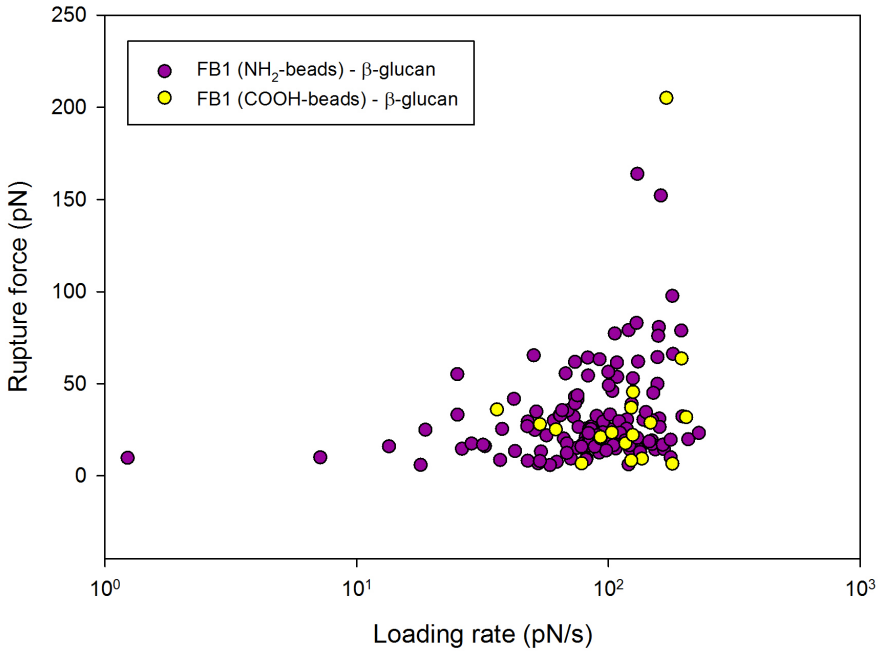

Figure 5.23: A comparison of the dynamic power spectra of β-glucan and fumonisin B1 on either amino- or carboxyl- beads. β-glucan was immobilized on 3.36 µm amino beads for both sets, while 2.18 µm amino beads and 2.10 µm carboxyl beads were applied for immobilization of fumonisin B1.

Summary of the cell wall components - fumonisin B1 experiments

A summary of the experiments involving the cell wall components of *S. cerevisiae* and fumonisin B1, including the control experiments, is illustrated in table 5.4. Mannan enabled a very low frequency of interactions with fumonisin B1, while β-glucan rendered more able to interact with fumonisin B1. However, several of the control experiments also presented interactions.

Table 5.4: Overview of the ability of the cell wall components of *S. cerevisiae* to interact with fumonisin B1, as well as the ability to interact with the corresponding control surfaces.

	COOH beads	**NH_2 beads**	**Fumonisin B1**	**β-glucan**	**Mannan**
COOH beads	NO	YES	N/A	NO**	NO**
NH_2 beads	YES	YES	NO**	YES	NO**
Fumonisin B1	N/A	NO**	N/A	YES	NO**
β-glucan	NO**	YES	YES	N/A	N/A
Mannan	NO**	NO**	NO**	N/A	N/A

**Some interaction was observed, but the frequency of interaction was less than 5 %.
N/A: the interaction was not investigated in this master thesis.

5.3 Force measurements by the use of optical tweezers

When the force-distance curves are generated, the loading rate is manually determined for each force jump. Fitting the loading rate for each force jump requires some training to be able to identify the shape of a force jump. When multiple bonds break within a small segment of the curve, it is difficult to fit the loading rate. This is due to a more flattened curve, than in the case of the rupture of a single bond. In cases where multiple bonds break one after the other, the loading rate determined will be lower than for single bonds. Forces below 4 pN were difficult to characterize as an unbinding force rather than an unspecific interaction or accumulation of noise. In some cases even greater forces were difficult to characterize due to high degree of noise.

5.4 Challenges associated with the optical tweezers

5.4.1 Identifying specific interactions

The shape of force curves of specific interactions should be identified to distinguish specific interactions from the unspecific ones. A specific interaction can be obtained by examining a positive control. However, no positive control was investigated in this master thesis. Identifying specific interactions was therefore challenging, and no clear difference was observed for the force curves obtained for the investigated samples and the negative controls.

There are many possible ways for two objects to interact, and identifying the molecular

mechanism behind the interactions is difficult. In this master thesis, specific interactions are characterized as the interactions between fumonisin B1 coated beads and either *S. cerevisiae* cells or its cell wall components. Consequently, self-interactions of uncoated polystyrene beads, or interactions between a coated and an uncoated bead, are defined as non-specific. However, it is not certain if these interactions characterized as unspecific might be due to a specific intermolecular binding event. These interactions can therefore be useful in determining the molecular mechanism behind the interaction of *S. cerevisiae* and fumonisin B1.

An example of the signature of a specific interaction is demonstrated below, which is obtained by measurements between β-glucan and fumonisin B1 on amino-functionalized beads (figure 5.24). The force curve presents a slightly increasing slope, from right to left, until there is a force jump upon rupture of the bond, and the curve drops to the horizontal baseline. In order to obtain a correct estimation of the loading rate, the curve should have a low noise level before the bond breakage. It is also important that the slope of the fitted loading rate corresponds with the slope of the area to which it is fitted. This can be obtained by adjusting the length of the red line, which indicates the area used for fitting the loading rate (figure 5.24).

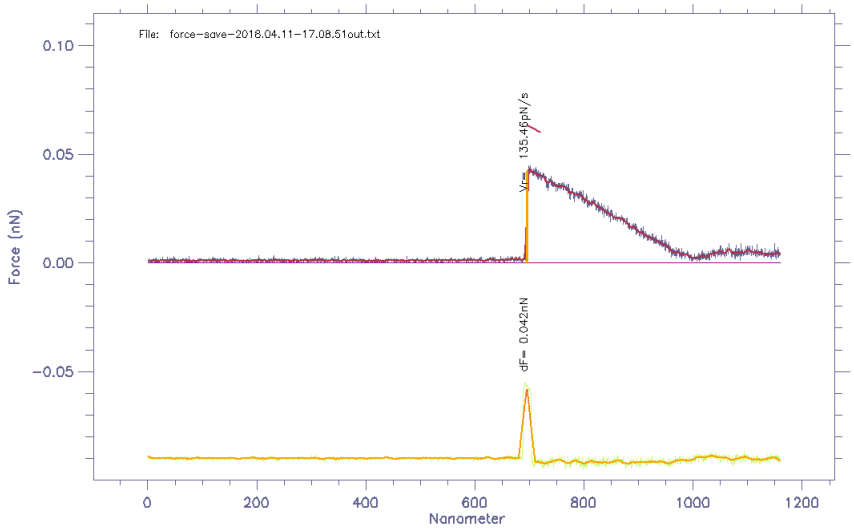

Figure 5.24: Demonstration of force curve with good estimation of loading rate. The force curve is obtained from measurements between β-glucan and fumonisin B1 on amino beads.

In some cases, fitting of the loading rate was difficult due to the appearance of the force curve. Some of the curves were excluded, since the loading rate could not be estimated correctly. High levels of random noise is one parameter that can cause difficulties for estimating

the loading rate. The random noise can be due to insufficient stabilization of the lasers. If random noise appears in the stretch of the curve immediately before the bond breaks, then it might result in an incorrect estimation of the loading rate. This can be avoided to some degree by adjusting the stretch of the curve used for fitting, by avoiding the areas with high level of noise. There can also be cases where two bonds rupture simultaneously or in close proximity in time. The force curves will then either appear as jagged or flattened. The loading rate can be correctly estimated for the first rupture if the appearance of the curve allows the two ruptures to be identified separately (figure 5.25).

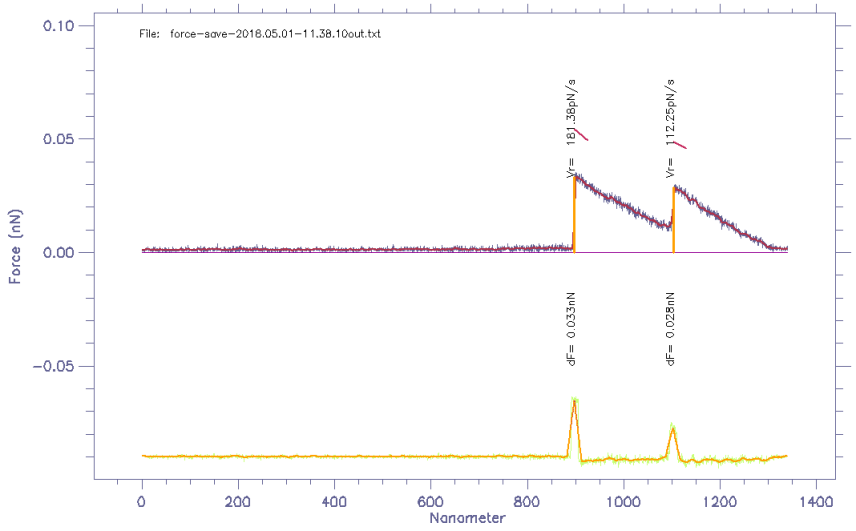

Figure 5.25: Demonstration of force curve with multiple bond ruptures. The loading rate can only be correctly estimated for the first rupture.

There was also recorded force curves without any force jump, where the curve linearly increased without dropping to the baseline during the measurement. This was due to the beads remaining connected during the measurement. Such force curves were excluded. Another source of an unspecific interaction can be when a polysaccharide is able to interact with the bead surface and is gradually peeled off when the beads are pulled apart. This can be observed as a horizontal force curve before the force jump, which is illustrated in a and b in figure 5.26.

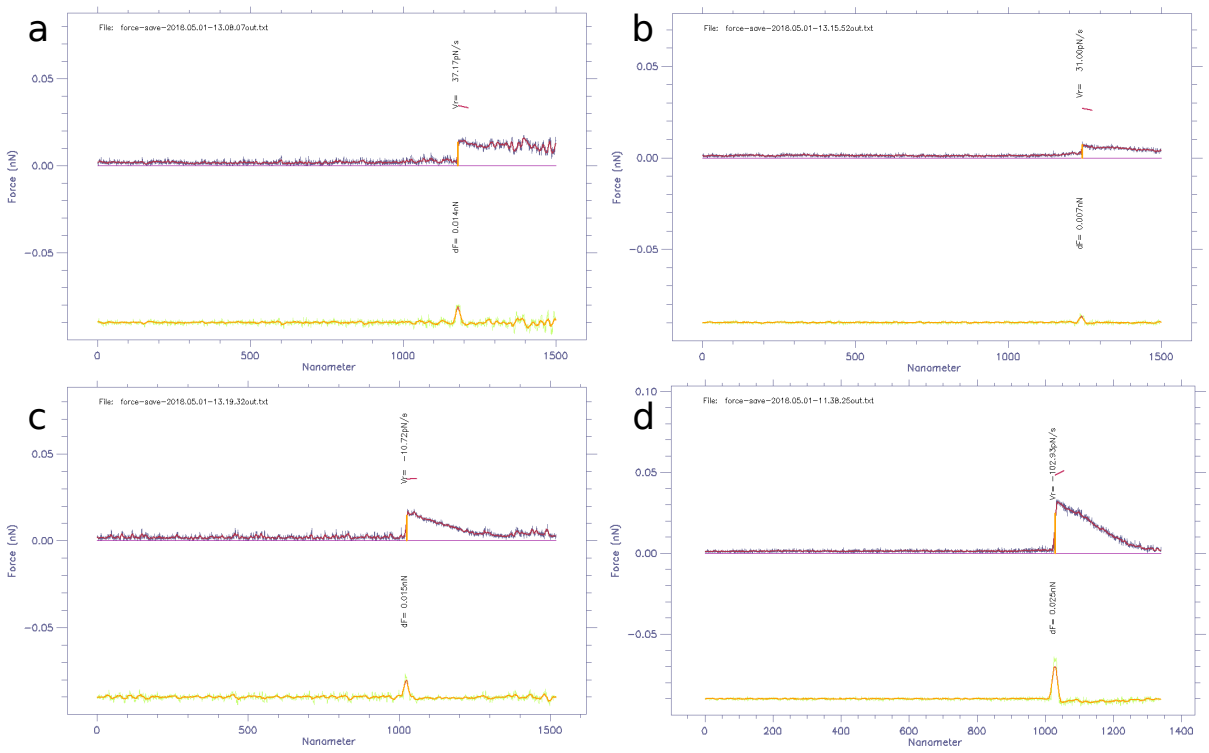

Figure 5.26: Demonstration of force curves that should be excluded due to difficulty in estimating the loading rate. (a,b) Illustrates force curves with a horizontal curve before the force jump, which can be obtained during peeling. (a) Also demonstrate force curves with a high level of background noise. (c) Indicates the rupture of two bonds within a short distance. (d) Illustrates incorrect estimation of the force.

The height of the vertical line, which is the force estimated by the PostProcessing software, is an important parameter when determining the loading rate. The force is estimated based on the height of the yellow line, demonstrated in figure 5.24. In some cases, the strength of the force is incorrectly estimated, which can be observed by the yellow line not reaching the top of the force curve (figure 5.26d). This will further affect the slope of the loading rate line.

5.4.2 Factors able to affect the frequency of interactions

The adhesiveness of two objects can be quantified based on the observed frequency of interaction. If an interaction is expected, then the observed frequency of interaction can be a good indication of the availability of the functional groups involved in the interaction. However, several factors are able to affect the measured interaction frequency, thus influencing the reliability of the obtained values. The presented values must therefore be carefully analyzed when evalu-

ating the results. On the other hand, they can give a small indication of the interaction ability of the different samples.

In this master thesis, the polysaccharides and fumonisin B1 are immobilized on polystyrene beads. By comparing the amount of observed interactions between two coated beads with the interactions observed for uncoated beads might give an indication of the interaction being specific or not. This can be used to distinguish between unspecific and specific interactions.

In order to achieve a frequency of interaction that is as reliable as possible, it is important to localize the correct position of the objects in the z-direction before starting the measurements. If the objects are not evenly leveled in the z-plane, then they might not be in direct contact during the measurements and therefore not able to interact properly. During the force measurements, the time and force should be approximately the same for each measurement. For instance, a higher frequency of interaction was observed when the objects were pressed together with a force that resulted in a small visible displacement of the stationary object compared to the interactions with no visible displacement. Each experiment was therefore conducted using 0.5 sec hold-time and the objects where pressed together with a force that resulted in a small visible displacement. Differences in surface coverage of the polysaccharides or the mycotoxin on polystyrene beads can affect the probability for the frequency of interactions. Several bead pairs (or bead-cell pairs) were investigated for each sample in order to compensate for such challenges.

Controlling the applied loading force

An increased frequency of interaction was observed when the beads were pushed together with a force resulting in a small displacement of the stationary bead. This can be explained by the larger contact area, which increases the possibility of achieving interactions. However, controlling the applied force is difficult. It was attempted to use an amount of force that resulted in a small visible displacement of the stationary bead for every experiment. The measurements were recorded only when the required separation distance was established. It would be favorable if the JPK NanoTracker software enabled a feedback loop in order to maintain a constant force.

Alignment of the optical traps in the z-plane

The importance of a correct alignment of the optical traps in the z-plane was experienced during the work of this master thesis. During an experiment performed with fumonisin B1 and β-glucan, no interactions were observed for about 500 measurements. When the traps were realigned, so that the smaller bead, immobilized with fumonisin B1, was positioned slightly lower in the z-plane than the larger bead, immobilized with β-glucan, the beads suddenly were able to interact. Among 839 attempts, 139 interactions were recorded from 10 pairs of beads, where all presented the ability to interact.

A proper positioning of the beads can be characterized by a visible displacement of the stationary bead when the beads are pressed together, as well as no visible change in contrast level of the beads upon contact. Positioning of the beads in the z-plane was based on noted locations which had provided interactions in previous experiments. The position was discovered to be dependent on the size of the bead, where small beads were positioned lower in the z-plane than larger sized beads. It was observed that when the smallest bead was trapped in trap 1, it should be positioned at approximately - 0.1 µm to - 0.25 µm, while the larger bead in trap 2 should be positioned in the range of 0.3 µm to 0.45 µm.

However, obtaining a good position was difficult and time-consuming. The position in the z-plane had to be adjusted for each bead pair, which could result in positions outside of the mentioned range. Even when trapping a bead pair with the same size as a previously trapped pair, the location had to be adjusted for that particular bead pair. A contributing factor can be the small variety in size of the polystyrene beads.

Trapping of yeast cells

When large yeast cells were trapped, approximately 4 µm and larger, it was observed that their movement was not fully constrained. During measurements, this resulted in altered separation distance between the fumonisin B1 coated bead and the trapped yeast cell. The separation distance was therefore constantly adjusted to avoid measurements without contact between the bead and the cell. However, this might have affected the frequency of interaction obtained for the experiments performed with larger yeast cells.

Some organelles within the cells possess a refractive index that allows the cells to be trapped, such as the nucleus. However, the rest of the cell structure might be able to move around these trapped organelles and thus move in the trap. It was observed that the movement of smaller cells was easier to restrain, and it was thus favorable to trap smaller cells (about 3 μm).

Distribution of polysaccharides or mycotoxin on the bead surface

An even distribution of the polysaccharides or the mycotoxin on the surface of the bead is favorable. It is also preferable to obtain an approximately equal amount of the polysaccharides or the mycotoxin on the beads. However, this is unfortunately not the case. Within a sample, some bead pairs presented a higher frequency of interactions than others. This is exemplified by the measurements performed on fumonisin B1 on amino-functionalized beads versus untreated amino-functionalized beads. In one sample, 4 out of 5 bead pairs did not present the ability to interact. It was also observed that a small adjustment of the position in the y-plane for one of the beads could result in increased frequency of interactions for a bead pair. In order to compensate for this variability, interactions were recorded for several bead pairs for each sample. In addition, small adjustments of their position in the y-plane were performed for each bead pair.

5.4.3 Impurities in the sample

During the experiments performed in April 2018, small impurities were discovered in the samples. These impurities either floated freely in the sample or were attached to the surface of the beads or to the bottom of the sample chamber. The refractive index of these impurities allowed them to be pulled towards and into the traps. During measurements, a pair of beads would not demonstrate any sign of interaction, but when some impurities were pulled into the traps, suddenly interaction between the beads was observed. For some of the observed interactions, the beads were able to move slightly apart before a jump in force was observed, indicating a bond rupture. It might indicate that the contaminants were able to act as a linker between the beads.

In an attempt to reduce the presence of these impurities, the different buffers applied in the experiments were filtered with a 0.1 μm filter syringe. In addition, the coverslips used for the sample chamber were washed in MQ and dried with nitrogen gas before BSA was applied to the

glass surfaces. After BSA treatment, the coverslips were again washed in MQ and blown clean with nitrogen gas. The amount of impurities present was slightly reduced, but the frequency of interaction was the same.

The contaminants were in particular present in the samples with uncoated amino beads, observed both for 2.18 µm and 3.36 µm beads. Some 3.12 µm sized amino-functionalized beads were borrowed from the Department of Physics at NTNU to investigate if the stock-solutions might have been the source of the contamination. During the measurements with the 3.12 µm beads, no impurities were observed. Despite the lack of visible impurities in the sample, the amino-functionalized beads still presented the ability to interact.

5.5 Microarray of *S. cerevisiae* cells

The fabrication of the PDMS stamp used for microcontact printing in this thesis was performed by Kertu Liis Krigul. Optimization of the fabrication procedure is not a part of this thesis, and therefore are not the challenges related to this procedure further elaborated. For information on the process of producing the PDMS stamp, it is recommended to read the Master's thesis by Kertu Liis Krigul.

The ability to form a microarray of *S. cerevisiae* cells on a PLL-patterned glass surface was investigated using a Zeiss Axiobserver Z.1 microscope. A PDMS stamp was used to transfer the PLL pattern onto the glass surface by microcontact printing. The patterned glass surface was further incubated with a cell suspension. Different concentrations of the cell suspension was investigated, as well as different periods of incubation.

5.5.1 Microcontact printing of PLL-FITC

The deposition of a PLL pattern by the use of the fabricated PDMS stamp was investigated using the fluorescent PLL-FITC. A PDMS stamp with features of 6 µm diameter with 12 µm separation distance was covered with a PLL-FITC solution (0.5 mg/mL) for 15 min. The stamp was further dried with N_2 gas, and then a cover glass was placed on top of the PLL-FITC treated PDMS surface in order to deposit the pattern onto the glass. By applying a FITC filer on the Zeiss Axiobserver Z.1 microscope, the deposited PLL-FITC would appear green, rendering it easier to

investigate the deposited pattern. Figure 5.27 demonstrates a successful deposition of the PLL-FITC pattern.

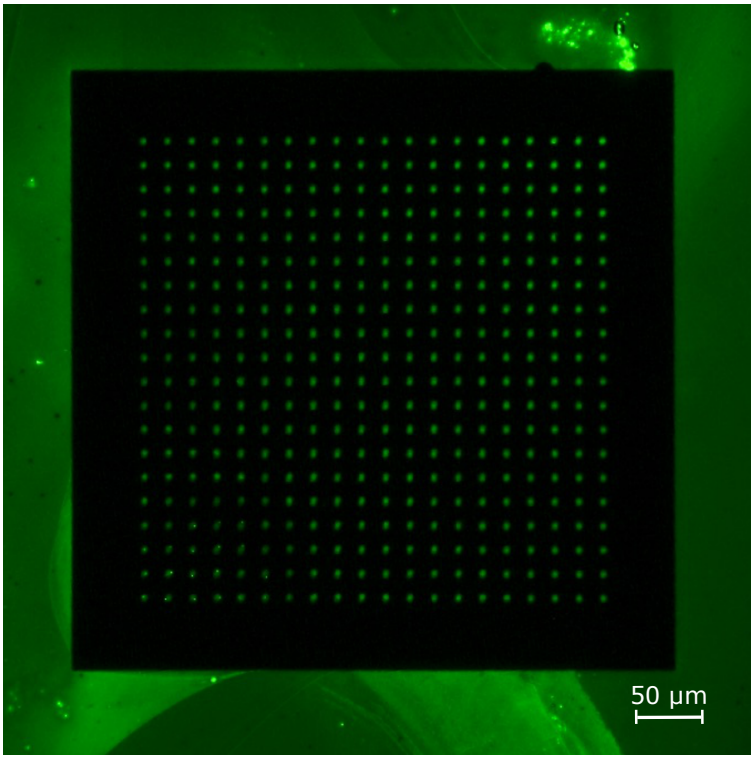

Figure 5.27: Microcontact printing of PLL-FITC (0.5 mg/mL) on cover glass. Demonstration of pattern obtained using a PDMS stamp with features of 6 µm diameter and 12 µm separation distance. Image obtained by bright field mode (20x) using the FITC filter on a Zeiss Axiobserver Z.1 microscope.

However, the deposition of the pattern was not always successful (figure 5.28). In some cases, the weight applied to the stamp was too high, resulting in the bottom of the stamp also touching the glass surface (a, b). If the weight applied to the stamp was unevenly distributed, then only parts of the pattern was deposited (c, d).

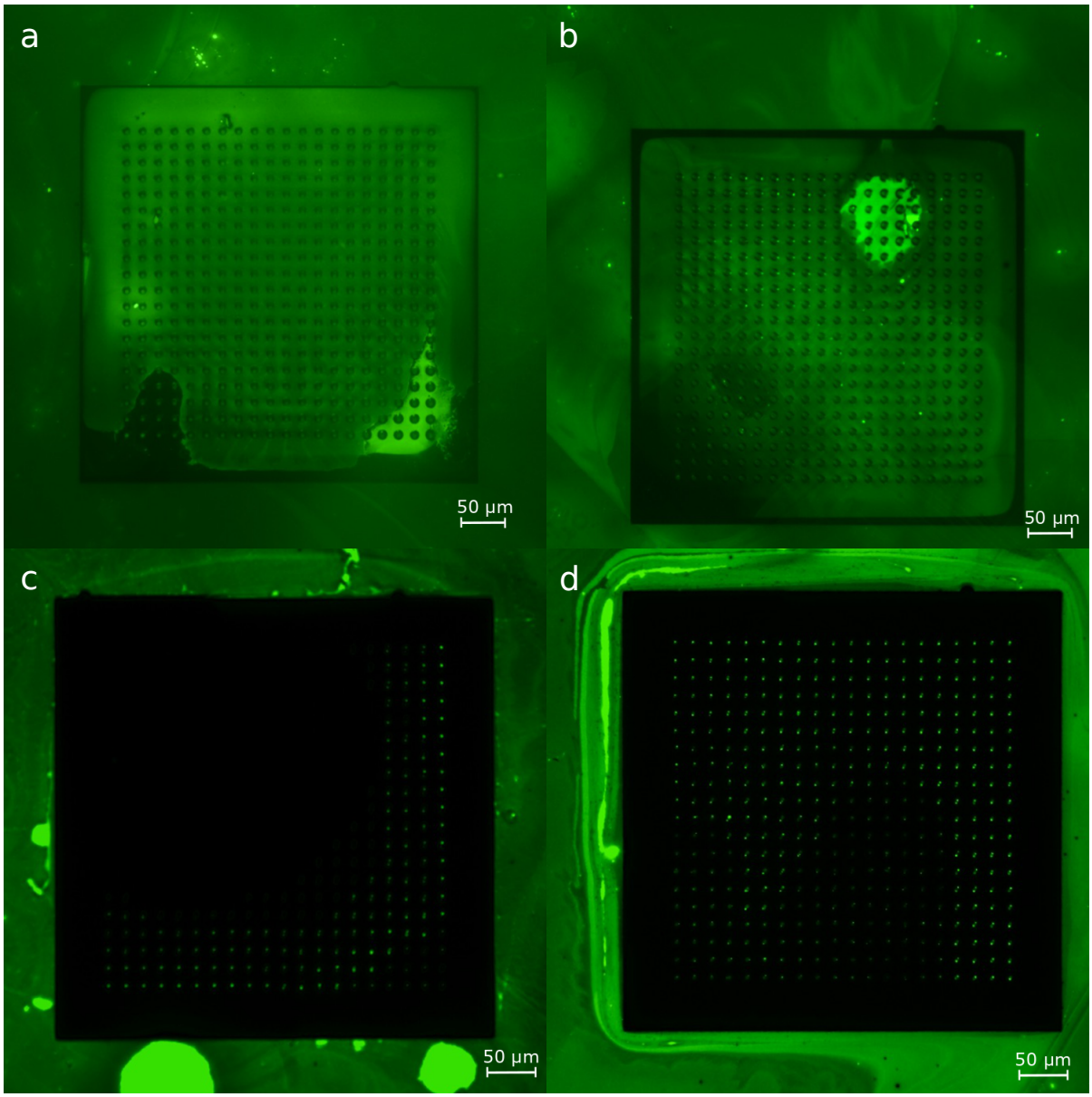

Figure 5.28: Demonstration of failed deposition of PLL-FITC (0.5 mg/ml) pattern on cover glass. Bright field images (20x) of pattern obtained when (a, b) applying too much weight on the stamp and (c, d) uneven distribution of weight on the stamp. Images obtained using the FITC filter on a Zeiss Axiobserver Z.1 microscope.

5.5.2 Microcontact printing of PLL

It was attempted to deposit a PLL pattern on a glass surface by the use of microcontact printing. The same procedure performed with PLL-FITC was repeated with a solution of PLL (0.01%). The area where the pattern had been deposited was marked with a pen, in order to locate the pattern

easier in the Zeiss Axiobserver Z.1 microscope. Despite the low amount of material deposited, the PLL-spots were visible on light microscope images (figure 5.29). The image presented in figure 5.29a demonstrates a larger area with the pattern, however, the appearance of the pattern indicates that the stamp has been moved slightly during the deposition. Compared to the round features visible in the image presented in figure 5.29b, the deposited pattern features in (a) have more of a rod-like shape.

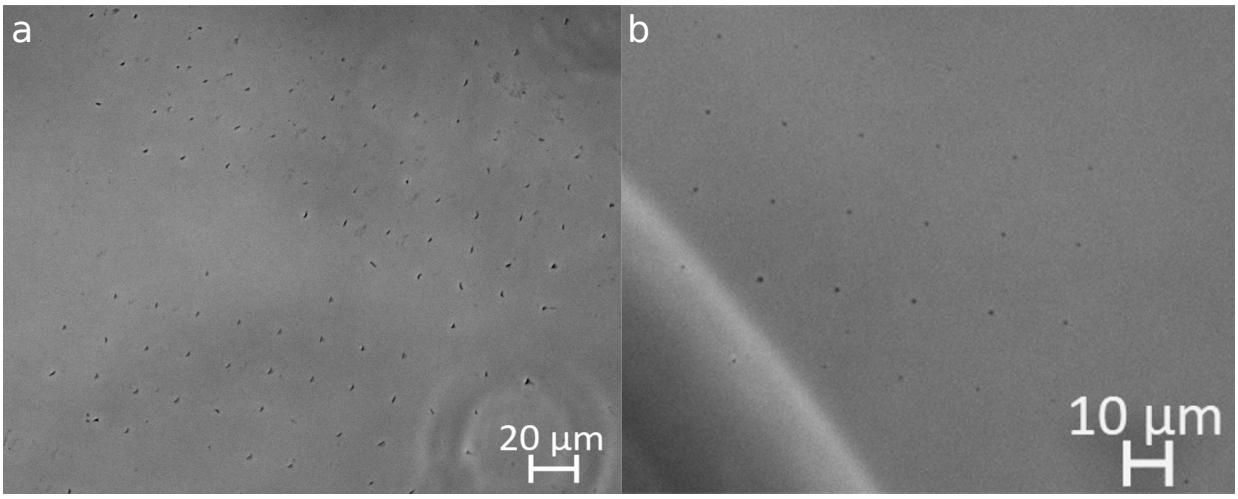

Figure 5.29: Pattern of PLL (0.01 %) deposited on cover glass, obtained by microcontact printing. A PDMS stamp with features of 6 µm diameter with 12 µm separation distance was used to deposit the pattern. (a) Phase contrast image (20x) and (b) bright field image (20x) of PLL pattern.

5.5.3 Immobilization of *S. cerevisiae* cells on PLL pattern

In order to fabricate a microarray of *S. cerevisiae* cells on glass, a 1:2 diluted cell suspension (in HEPES) was incubated on a PLL patterned glass surface for 5 min. This required that the cells would only adhere to the 6 µm sized PLL features, thus creating a micrroarray of cells with 12 µm spacing distance. The glass slide was subsequently washed by gently moving the glass slide around in a petri dish with MQ water. After performing the washing procedure, the glass surface had HEPES added to prevent the remaining cells from drying out. Figure 5.30 shows two areas (a, b) of the glass surface with a partly visible pattern of cells. Other areas of the glass surface contained large aggregates of cells (c, d).

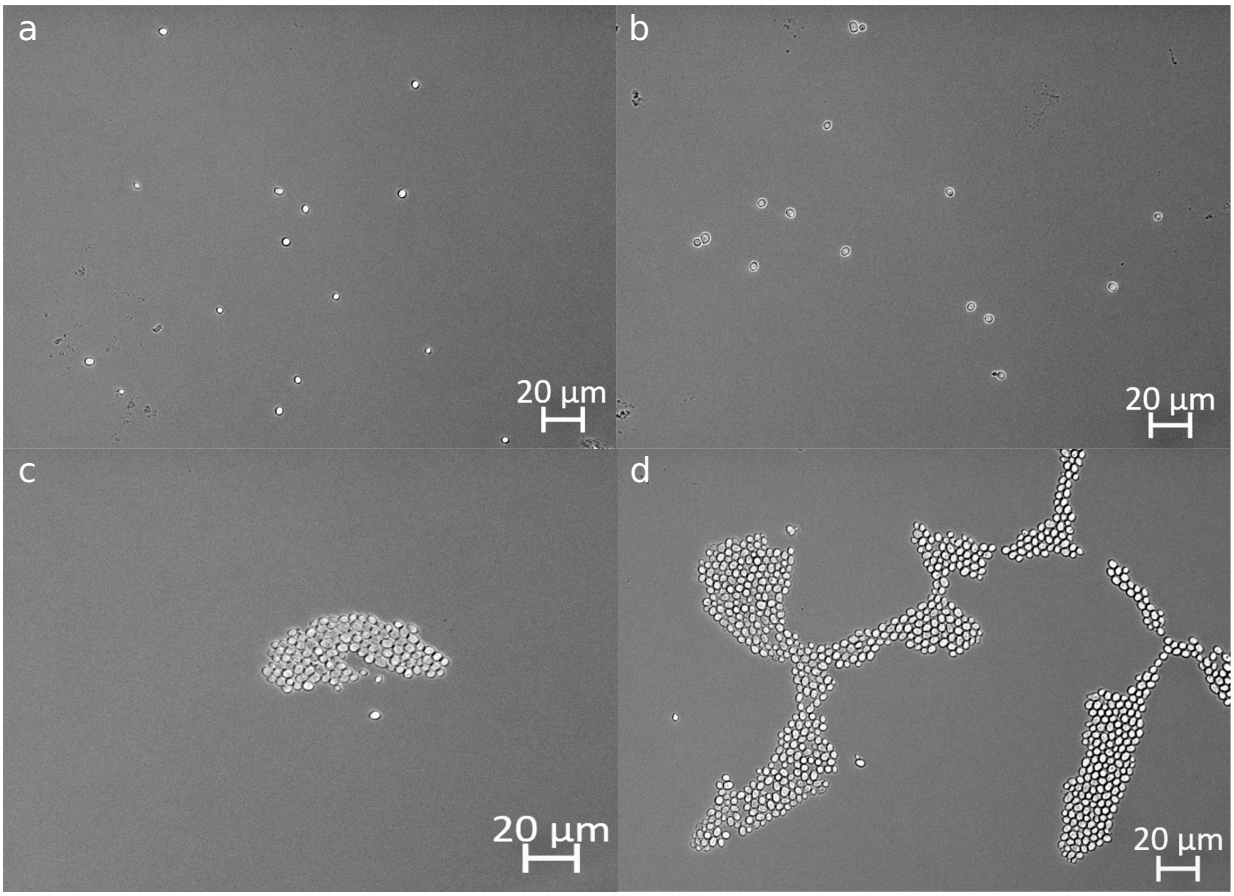

Figure 5.30: Immobilization of *S. cerevisiae* cells on PLL (0.01 %) patterned cover glass. The cover glass was functionalized with a pattern of PLL by microcontact printing, and further incubated with a cell suspension for 5 min. (a, b) Demonstration of a partly visible pattern and (c, d) areas with aggregates of cells. Images obtained by bright field mode, 20x magnification.

In order to prepare a microarray, one must not only assure high adhesiveness onto surface spots introduced using microcontact printing, but also assure that the adhesiveness of the surrounding areas is kept low. The following experiments were performed in order to document the adhesiveness of surface as a function of the surface functionalization as described.

Optimization of experimental factors

An aliquot of 1 mL from the stock solution of yeast cells in YPD medium was washed and re-suspended in HEPES buffer, as described in section 4.2.1. For the first experiment, the pellet of 1 mL stock solution was re-suspended in 1 mL of HEPES. Approximately 200 µL was required to cover the glass surface. When investigating the slide by the naked eye, this highly concentrated cell suspension created a light grey layer of cells on the surface. Several layers of cells were

identified when investigating the glass in a microscope, and the solution was regarded as too concentrated. A new experiment was performed with 1:2 dilution, where the pellet of 1 mL of stock solution was suspended in 2 mL of HEPES. This resulted in a slightly grey layer of cells, and was confirmed to give a good coverage of cells on the slide.

Three different incubation periods were tested; 30, 10 and 5 min. An incubation period of 30 min was regarded as too long, due to the high probability of the cells forming aggregates on the glass surface. The amount of large aggregates was to some degree reduced for an incubation period of 10 min, while 5 min resulted in mostly small aggregates.

After incubation, a washing procedure was performed in order to remove unbound cells. Four different washing procedures were tested. One consisted of gently moving the glass slide around in a petri dish with MQ water. Another procedure was based on pipetting MQ water onto the glass surface while laying flat, and then removing most of the liquid. Another version of this procedure was also investigated, where the glass slide was held slightly tilted over a petri dish. MQ water was added to the top of the glass, which flowed down the glass surface. The last procedure consisted of gently dipping the glass slide into a petri dish with MQ water, with the functionalized side facing down. It was attempted to keep the slide leveled with the water surface. The tested procedure was repeated three times for each glass slide. The different washing procedures presented relatively the same efficiency in removing unbound cells. However, all procedures depended on slow and gentle movements, in order to prevent strong forces that could result in detachment of adhered cells.

A 1:2 diluted cell suspension, 5 min of incubation period and a washing procedure consisting of gently moving the glass slide around in a petri dish with MQ was applied for the presented results. After performing the washing procedure, the glass surface had HEPES added to prevent the remaining cells from drying out.

Immobilization of *S. cerevisiae* cells on cleaned glass

The ability of *S. cerevisiae* cells to adhere to a clean glass surface was investigated in order to determine a good negative control. The glass slides were washed with ethanol and MQ water, and further dried with N_2 gas. A 1:2 diluted cell suspension (in HEPES) was incubated on the glass slide for 5 min. Figure 5.31 illustrates the number of cells present before and (a) after (b) wash-

ing. As illustrated, *S. cerevisiae* cells were able to adhere to a clean glass surface. Consequently, a clean glass surface did not constitute a good negative control.

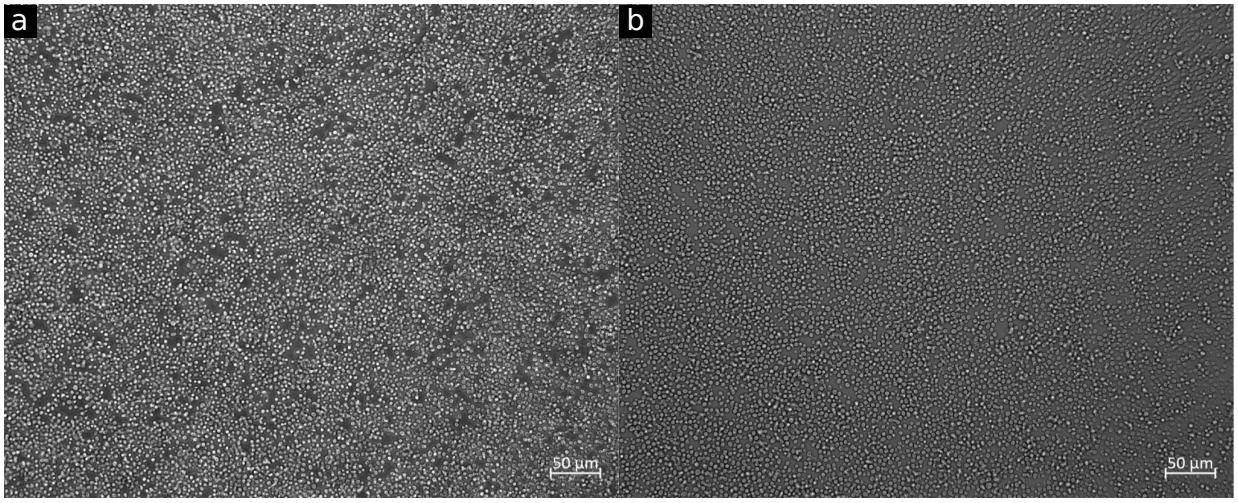

Figure 5.31: *S.cerevisiae* cells in HEPES buffer on cover glass cleaned with ethanol. The cell suspension was incubated on glass slide for 5 min before washed in MQ water. (a) Phase contrast image (20x) before washing and (b) bright field image (20x) bright field image after washing.

Immobilization of *S. cerevisiae* on pegylated glass

To prevent adhesion of *S. cerevisiae* cells to the glass surface, the cover glass was treated with PLL-g-PEG (1 mg/ml). The amphiphilic nature of PEG can provide a sterically induced exclusion zone, which will prevent the cells from adhering to the glass surface. The PLL-PEG treatment was able to reduce the amount of cells adhering to the glass. This is demonstrated in figure 5.32, where the glass slide contained almost no cells after washing in MQ water (b). Based on these results, it was decided to continue using PLL-g-PEG treated glass as a negative control.

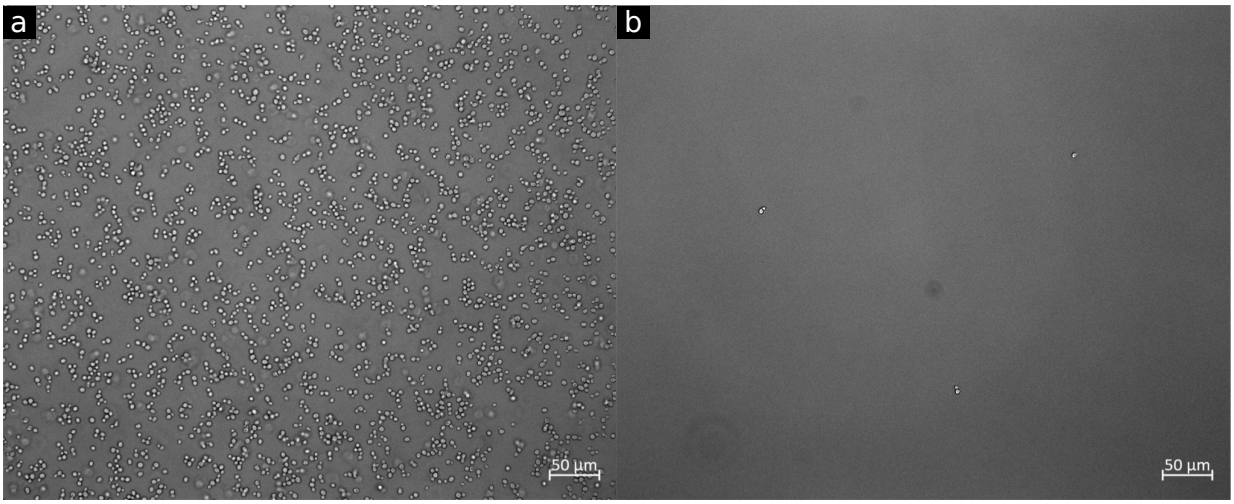

Figure 5.32: *S. cerevisiae* cells in HEPES buffer on cover glass cleaned with ethanol and treated with PEG. The cell suspension was incubated on glass slide for 5 min before washed in MQ water. Bright field image (20x) before (a) and after (b) washing.

Immobilization of *S. cerevisiae* cells on PLL coated glass

The adhesiveness of *S. cerevisiae* cells on PLL was investigated by coating the entire cover glass surface with PLL (0.01 %). The PLL-solution was added on top of the inert PLL-g-PEG cover, and was incubated for 15 min. A cell suspension was added to the PLL-coated glass surface, and further washed away using MQ water after 5 min of incubation. The glass slide was investigated before and after the washing procedure, which demonstrated a reduction in the number of cells present on the glass surface after washing (figure 5.33). Some cells were able to adhere to the PLL-coated glass surface, however, these were quite few compared to the number of cells present before washing the glass. The cells appeared both in aggregates and scattered as single cells. By investigating the entire PLL-coated surface, it was discovered some areas that did not contain any yeast cells at all. It was also observed a clear border between the areas with and without cell adhesion within the PLL-treated area (figure 5.34).

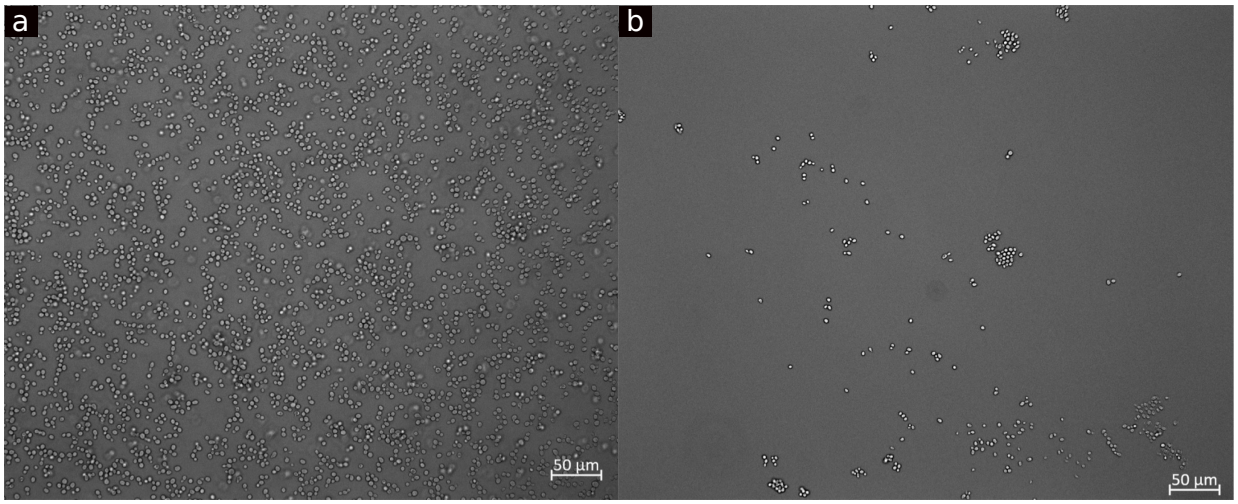

Figure 5.33: *S. cerevisiae* cells in HEPES buffer immobilized on pegylated cover glass functionalized with PLL (0.01 %). The cell suspension was incubated on glass slide for 5 min before washed in MQ water. Bright field image (20x) before (a) and (b) after washing.

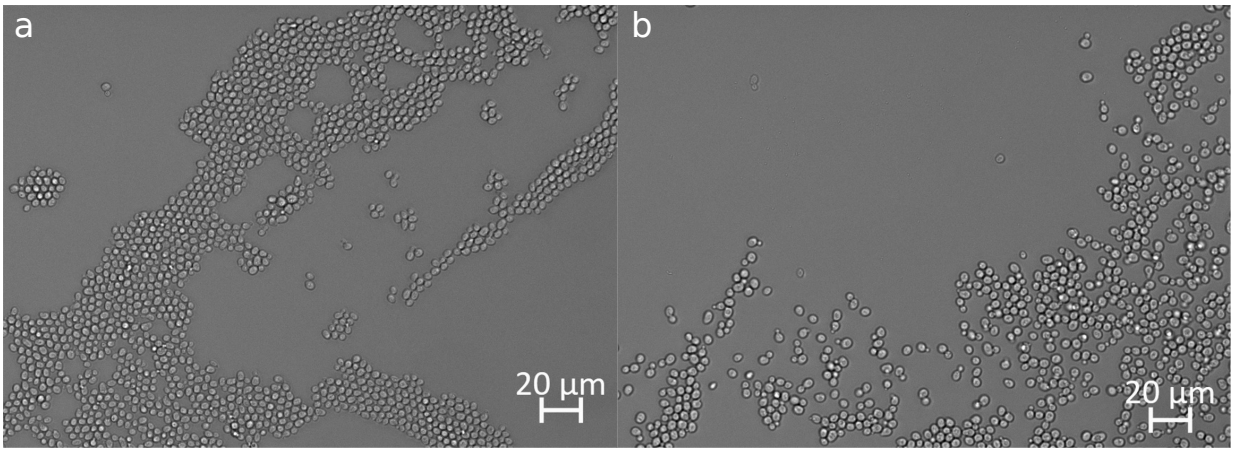

Figure 5.34: Demonstration of uneven coverage of *S. cerevisiae* cells immobilized on pegylated cover glass functionalized with PLL (0.01 %). (a) Demonstration of aggregates of cells and (b) clear border between areas with and without cells. Images obtained using bright field mode, 20x magnification.

These experiments thus indicate that the lack of success with obtaining a yeast microarray is due to the insufficient adhesiveness of yeast to the PLL spots, or insufficient adhesiveness of the PLL to the pegylated glass surface.

6. Comprehensive discussion of the information provided by the experimental work

Investigating cellular adhesion is of interest to a great diversity of applications within numerous fields, such as physiology, pathology and biotechnology. Several techniques are available for investigating this cellular adhesion at the single cell level [39]. However, the field of nanobiotechnology has presented new possibilities for experimental platforms that enables high throughput single cell analysis of cellular adhesion [37].

6.1 *S. cerevisiae* as an adsorbing agent of fumonisin B1

Applying *S. cerevisiae* as a adsorbing agent of mycotoxins in the gastrointestinal tract could be a promising method to protect against the toxic effects induced by these food contaminants [81]. *S. cerevisiae* has proven adhesiveness towards several mycotoxins in a suspension [4, 13, 82, 83]. However, in order to apply this microorganism for the removal of mycotoxins such as fumonisin B1, the underlying molecular mechanism of the interaction requires further investigation.

6.2 Interaction between *S. cerevisiae* cells and fumonisin B1

Viable wild-type *S. cerevisiae* cells did not present the ability to interact with fumonisin B1. This was indicated by both the flow chamber assay and the optical tweezers experiments. These results do not correspond with the study performed by Pizzolitto *et al.* (2012), which presented 60% removal of fumonisin B1 by *S. cerevisiae* cells in a suspension. Several other studies have also indicated the ability of *S. cerevisiae* to adsorb different mycotoxins in a suspension [3, 12–14]. A common feature with these experiments is that the adhesiveness was investigated in a suspension, where cells and mycotoxin molecules were able to move freely. The instrumental

setup of the flow chamber requires immobilization of the fumonisin B1 molecules on a coupon surface, while the fumonisin B1 molecules were immobilized on the surface of polystyrene beads for the optical tweezers. Consequently, the fumonisin B1 molecules were not able to move freely, which could have interfered with their ability to interact with *S. cerevisiae*. Attaching the fumonisin B1 molecules to the polystyrene beads might have offered a sterical hindrance, resulting in the fumonisin B1 molecules not being able to reach the inner layer of the cell wall. It was hypothesized that removing some of the outer mannan-layer might improve the access to the binding sites of fumonisin B1.

6.2.1 Identifying the *S. cerevisiae* cell wall component involved in the interaction with fumonisin B1

Investigating the role of the mannan-layer

The possible limited access to the binding sites offered by the mannan layer was investigated by examining the adhesiveness of the mutant Δmnn9. The cell wall of this mutant contains about 170 µg/mg mannan, compared to the 304 µg/mg in the wild-type BY4741 [78]. However, the reduced mannan content of Δmnn9 did not render it more able to interact with fumonisin B1 than the wild-type BY4741 cells. Neither did the protease treatment improve the ability of the BY4741 cells or Δmnn9 cells to interact with fumonisin B1. Consequently, reducing the mannan layer did not improve the adhesiveness of the cells, and the mannan layer was concluded to not provide any limitation of access to the fumonisin B1 binding sites. This is supported by the studies performed by Yiannikouris *et al.* (2004), which concluded that the mannan-layer presented no stereochemical blockage [12]. The ability of mannan to interact with fumonisin B1 was also directly investigated by the optical tweezers. With an interaction frequency of 3 %, the results support the assumption that mannan do not participate in the formation of a yeast-mycotoxin complex.

β-Glucan as the interacting cell wall component

On the other hand, β-glucan presented an interaction frequency of 16 %, when fumonisin B1 was immobilized on amino-functionalized beads. This supports the hypothesis of β-glucan be-

ing important in the formation of a yeast-mycotoxin complex, which has been indicated by previous studies of yeast-mycotoxin complexes [3, 12–14].

The strength of the measured rupture forces presented values below 70 pN, indicating a weak interaction between β-glucan and fumonisin B1. The interaction is assumed to consist of weak non-covalent bonds, such as hydrogen bonds and van der Waals forces. β-1,3-linked glucan is able to participate in both types of interactions, while β-1,6-linked glucan strengthens the van der Waals forces [13]. It can thus be assumed that β-1,6-linked glucan is not necessary for the formation of an interaction with fumonisin B1, but is able to strengthen and stabilize the interaction.

The β-glucan chains applied in this master thesis consisted of shorter chains and had reduced levels of β-1,6-linked glucan. The main content being β-1,3-linked glucan should promote an interaction with fumonisin B1. However, the length of the β-glucan chain might interfere with the ability to interact with fumonisin B1. Shorter chains result in closer contact between the beads in order to allow an interaction between the β-glucan chain and fumonisin B1. As elaborated in section 6.3.1, it was discovered that also the bead surface was able to promote an interaction, more specifically a self-interaction between amino-functionalized beads.

The obtained frequency of interaction for β-glucan and fumonisin B1 seems low compared to the percentage of adsorption presented by viable *S. cerevisiae* cells in the study performed by Pizzolitto *et al.* (2012). The *S. cerevisiae* cells presented the ability to adsorb approximately 60 % of the fumonisin B1 content in a suspension [4]. This might be due to the structural differences of β-glucan when immobilized on a polystyrene bead compared to the structure it possesses in the cell wall. It has been indicated that the alkali-insoluble β-glucan presents a higher adhesiveness than the simple alkali-soluble fraction [3, 13]. The alkali-insolubility of β-glucan results in the formation of single and/or triple helices. The cross-linking of β-glucan with chitin produces a fibrous network, consisting of alternating single- and triple helix regions, resulting in a structure where the adsorption sites for the mycotoxin is more available [12].

The partly soluble β-glucan obtained from Biotec Pharmacon AS can be structured as single- or triple helices, as well as random coils and aggregates in the stock-solution [84]. The β-glucan is attached through its reducing end to the surface of the polystyrene beads. Furthermore, the beads are subjected to several washing steps, as well as a sonication procedure prior to the ex-

periments. It is assumed that aggregates and triple helices will be dissolved during this process and that β-glucan will be structured as random coils or single helices on the surface of the bead. The β-glucan on the bead surface is thus considered to not present a complex structure, as the one it possesses in the cell wall. By subjecting the β-glucan solution to a dimethyl sulphoxide (DMSO) treatment, aggregates and other complex structures are dispersed into single chains [85]. Such a treatment will ensure the presence of only single chains on the surface of the polystyrene bead. However, a random coil or single helix structure of the β-glucan might result in less available adsorption sites for fumonisin B1. Consequently, the β-glucan chains might present a reduced adhesiveness towards fumonisin B1.

6.2.2 Improved adhesiveness of *S. cerevisiae* cells upon heat treatment

Some studies have presented promising results regarding heat treatment of the cells, which demonstrated an improved adhesiveness compared to viable cells [4, 86]. In order to investigate if the heat treatment improved the adhesiveness of the cells, the wild-type BY4741 cells where boiled in buffer for 1 hour. This was first investigated with the flow chamber assays, where 4 % of the initial amount of cells were able to adhere to the fumonisin B1-coated glass surface. A shear stress of about 10 Pa was required in order to remove all cells. This indicates a weak interaction between the heat treated cells and fumonisin B1, which corresponds with the assumption that the interaction is based on weak non-covalent bonds. The interaction capacity was investigated further with the optical tweezers, which presented 29 % frequency of interaction when fumonisin B1 was immobilized on amino-functionalized beads.

It can be assumed that the heat treatment results in a structural change in the cell wall, that makes the adsorption sites on β-glucan more available. The heat treatment initiates a cell response which acts to strengthen the cell wall, including increased levels of chitin [23, 87, 88]. The level of cross-linkages is also increased, such as the complex CWP-GPIr $\rightarrow$ β-1,6-linked glucan $\leftarrow$ chitin, as well as increased cross-linkages between chitin and β-1,3-linked glucan [23, 88]. This results in an increased fraction of alkali-insoluble β-glucan, which can be an important factor promoting interactions in the heat treated cells.

However, the increased levels of chitin and cross-linkages will increase the cell wall stiffness, which have been indicated to negatively affect the availability of the adsorption sites. Yian-

nikuris *et al.* (2004) discovered that the fraction of alkali-soluble β-glucan is actually more significant in mycotoxin adsorption than the insoluble fraction due to its cooperative process, allowing the mycotoxin molecules to move inside the cell wall structure and access the adsorption sites [3]. On the other hand, the heat treatment is also assumed to result in denaturation of the cell wall proteins [89]. Reduced levels of cell wall proteins may result in openings in the cell wall structure, allowing the fumonisin B1 molecules to access the adsorption sites. This remodelling of the surface topography was confirmed by the study performed by Adya *et al.* (2006), which demonstrated an increase in cell surface roughness as a result of a heat treatment (90°C, 1 hour) [90]. It can be assumed that the removal of cell wall proteins participate in the formation of cracks and holes in the cell wall. These openings in the cell wall structure might enable the fumonisin B1 molecules to access the adsorption sites in the complex three dimensional β-glucan structure.

Fumonisin B1 molecules are quite large compared to other mycotoxins, with a molecular weight of 721.838 g/mol compared to an average of about 300 g/mol for toxins such as zearalenone, ochratoxin A and deoxynivalenone (values obtained from PubChem Compound Database). A larger structure requires a bigger inner helical space in order for the fumonisin B1 molecules to reach the adsorption sites. It can thus be assumed that the complex cell wall structure in viable viable BY4741 cells might be too compact in order to let fumonisin B1 reach the adsorption sites, when their movement is restricted by being immobilized on a coupon surface or polystyrene bead.

6.2.3 Evaluating the specificity of the recorded interactions

The distribution of rupture forces obtained for the interactions between β-glucan and fumonisin B1 indicated the presence of multiple interactions. These are illustrated by the tails in the histogram presented in figure 5.19. This was confirmed by the appearance of the force curves, where some presented jagged curves, indicating the rupture of several bonds (figure 5.18a). This might be due to several fumonisin B1 molecules interacting with one or several β-glucan chains, which can indicate a too dense coating in order to investigate single-molecule interactions. It has been indicated that the interaction of one mycotoxin molecule promotes a small change in the helicoidal structure of β-glucan, and thus allowing more mycotoxin molecules to attach

until the adsorption sites are saturated. This discovery is based on the interaction between *S. cerevisiae* and zearalenone [3], however, if fumonisin B1 can initiate the same event, then this phenomenon can provide an explanation for the multiple interactions observed.

The specificity of the observed interaction between β-glucan and fumonisin B1 is however difficult to determine, as the negative controls also presented interactions. Since uncoated amino-functionalized beads were able to self-interact, it was questioned if the observed interaction was due to β-glucan and fumonisin B1 or the functional groups on the bead surface. The uncoated amino-functionalized beads presented curves where about 25 % obtained interaction, and thus a greater adhesiveness than the one observed for β-glucan and fumonisin B1 (figure 5.14). However, the recorded interaction frequency dropped to 6 % and 4 % when one of the amino-functionalized beads were coated with either β-glucan or fumonisin B1, respectively. This indicates that β-glucan and fumonisin B1 have been successfully immobilized on the bead surface. If the observed interaction is between the amino bead and free amino-groups on the coated bead, or between the uncoated amino bead and either β-glucan or fumonisin B1 is still unclear. One possible explanation is the sterical hindrance offered by the polysaccharide and mycotoxin molecules on the bead surface, resulting in reduced accessibility to the free amino-groups on the bead surface and thus a reduction in recorded interaction frequency.

However, the heat treated cells also presented the ability to interact with an uncoated amino-functionalized bead. This indicates that one or several of the cell wall components are able to interact with an amino-group. As the interaction between β-glucan and fumonisin B1 is presumably based on hydrogen bonds and van der Waals forces, then β-glucan can be assumed to be able to form hydrogen bonds with a free amino-group. When examining the distribution of rupture forces, the interactions obtained for heat treated cells and fumonisin B1 generated a more clustered distribution of data points with low rupture force and low loading rate (figure 5.12). The more scattered distribution observed for the interaction with uncoated amino-beads might indicate a more unspecific interaction. The force curves presented high levels of background noise, which would have affected the distribution of rupture force. Both sets of data had force curves with a long and gradual increase in force before the force jump, indicating multiple interactions (figure 5.10). The observed interaction between heat treated cells and amino-functionalized beads might be due to an electrostatic interaction. The heat treatment might

affect the surface charge of the cells, rendering them more able to form an electrostatic interaction with the amino-groups. This can be investigated by measuring the zeta potential of the heat treated cells.

When further examining the self-interaction of amino-functionalized beads, it was discovered some high levels of background noise during the force measurements. This may have impacted the estimation of rupture force and loading rate, and thus affected the reliability of these results. The amino beads presented rupture forces up to 400 pN, however, these were probed at high loading rates (figure 5.22), which is assumed to be a contributing factor to the high values. Furthermore, it can be assumed that the high loading rates and rupture forces are obtained due to multiple interactions. This has been indicated by previous studies performed by Friddle *et al.* [91, 92].The ability to self-interact can be due to the formation of hydrogen bonds, as the amino group is able to act both as a hydrogen donor and acceptor. However, the samples with untreated amino beads were also later discovered to be contaminated, where the observed impurities could have affected the interactions. The actual role of these impurities in the interaction between uncoated amino-beads is elaborated in section 6.3.1.

Based on these results, it can be assumed that the interaction observed for beads coated with β-glucan and fumonisin B1 is due to the coating of the beads and not the functional amino groups on the bead surface. The specificity of the interaction can be confirmed by applying free β-glucan chains in the solution, which will compete with the β-glucan on the bead surface to form an interaction with the fumonisin B1 molecules. However, the ability of β-glucan to interact with amino-groups on the bead surface can not be excluded. The force curves followed the baseline for about 200 nm before initiating a linear increase in force, this was observed for the interactions between β-glucan and fumonisin B1, as well as the interactions with uncoated amino-beads (figure 5.18). This might indicate the distance required to stretch the polysaccharide chains, before an interaction was detected. The force curves obtained for the uncoated amino beads presented an increase of force immediately when the beads started to move apart (figure 5.21), and thus implying an interaction between the bead surfaces.

6.2.4 The effect of the choice of functional group used for immobilization of fumonisin B1

The fumonisin B1 molecule contains several functional groups that are able to participate in a hydrogen bond, such as the hydroxyl-, carboxyl- and amino-groups. It has been indicated that the amino-group enhance their toxic activity, and can thus be important in the formation of a yeast-mycotoxin complex. The interaction frequency recorded when fumonisin B1 was immobilized on carboxyl-functionalized beads was much lower than for amino-functionalized beads (figure 5.14). This was observed both against β-glucan and heat treated cells.

This might indicate that the amino-group enhances the ability to form a yeast-mycotoxin complex. When investigating the strength of the interaction, the recorded rupture forces for fumonisin B1 on amino beads versus heat treated cells were generally lower and probed at lower loading rate than the rupture forces obtained for fumonisin B1 immobilized on carboxyl-beads (figure 5.13). The force curves for the amino-coated beads presented overall an almost horizontal slope, indicating several bond ruptures (figures 5.10). The appearance of such force curves results in a lower estimation of the loading rate. The force curves of carboxyl-coated beads had a more rapid increase in force, presenting a more steeper slope and thus a higher estimation of loading rate (figure 5.7).

The flow chamber experiments were performed with fumonisin B1 immobilized on a carboxyl-silanized surface. The amount of cells capable of adhering to the surface could have been higher if fumonisin B1 was immobilized on an amino-silanized surface, based on the results obtained from the optical tweezers. However, it can be questioned if the amino-functionalized surface constitutes a good negative control. Hence, the specificity of an interaction with fumonisin B1 on an amino-functionalized surface has to be investigated further.

6.3 Quantification of interactions by shear stress flow chamber and optical tweezers

Both techniques presented the ability of quantifying the interactions between *S. cerevisiae* and fumonisin B1. The optical tweezers offer controllable conditions, where the position of the

trapped objects, separation distance and force applied to the trapped objects can be adjusted during the measurements. This allows re-positioning of the trapped cell, in order to probe a larger area of the cell surface. The flow chamber assay acts to mimic a more natural environment, by subjecting the cells to fluid shear stresses. The cells are able to move freely within the flow cell. However, this might result in unavailable adsorption sites, if they are located on the part of the cell pointing away from the fumonisin B1 coated surface. The restricted movement of the fumonisin B1 molecules might also prevent the molecules from reaching the adsorption sites if they are located slightly inside the cell wall. The optical tweezers can apply force in order to reach such unavailable adsorption sites. Increasing the contact force also results in a larger contact area, which increases the probability of cell adhesion. However, when applying *S. cerevisiae* cells for adsorption of fumonisin B1 in the gastrointestinal tract, applying force in order to achieve an interaction will not be possible. Thus, the flow chamber might be regarded as a more realistic model for measuring the adhesiveness since the cells can move freely. However, different challenges are associated with both techniques, and these challenges may have affected the obtained results.

6.3.1 Establishing a good negative control

The negative controls are applied to indicate the purity of the sample. If they present a notable number of interactions, then the samples should be reproduced with cleaned equipment and filtered solutions. If the observed interactions are due to impurities in the sample, then the number of recorded interactions should be decreased.

For the optical tweezers experiments, impurities were observed floating freely in the sample, but also attached to the bottom of the sample chamber or to the surface of the beads. The impurities were able move and presented a refractive index that enabled them to be trapped by the laser beam. It was hypothesized that these impurities might be bacteria, which had a diameter of about 1 µm. Further investigation of the identity of these impurities is needed, which can be achieved by for instance fluorescent staining of bacteria and investigating the sample in a fluorescent microscope.

The actions introduced in order to reduce the amount of impurities did present lower levels of observed impurities. The impurities were in particular observed in the negative control

sample containing only amino-functionalized beads. Even at reduced levels of impurities, the beads presented an interaction frequency of 25 %. It was hypothesized that these impurities might be responsible for the interaction. This was further investigated by repeating the experiment with 3.12 µm amino beads from the Department of Physics. These amino-functionalized beads presented curves with interactions in about 20 % of the measurements, without the presence of any visible impurities. This might indicate that the interaction between the uncoated amino-functionalized beads is due to the amino-groups, and not the impurities. The role of the functional groups in initiating an interaction can be further investigated by reducing the pH of the sample to around 5, which will inhibit the interaction between the amino-groups. If the amino-functionalized beads are still able to interact it might be due to the surface properties of the polystyrene beads. The bead surface can also be treated with PEG or zwitterions, in order to make the amino-groups inert.

6.3.2 Importance of the density and homogeneity of the surface functionalization

A high density of the surface functionalization can prevent unspecific interactions with the surface. However, a very dense layer of coating can result in multiple interactions, which is unfavorable when detecting single-molecule interactions. If applying a less dense layer of surface functionalization, an inert linker can be used in order to distinguish specific interaction from the unspecific ones.

For the optical tweezers experiments, an inert linker can be applied between the bead surface and the molecule of interest. This will result in interactions between the molecules of interest happening further away from the bead surface, which could enable the discrimination of unspecific and specific interactions. Interactions with the bead surface can be excluded during analysis, where the distance of the bond rupture should exceed the length of the applied linker. A linker also enables the use of a greater variety of functionalized polystyrene beads. For immobilizing fumonisin B1 on the bead surface, an amino- or carboxyl-functionalization of the bead surface was required. However, when the fumonisin B1 molecule is attached to a linker, presenting the required functional group, the other end of the linker can be custom made to

match a variety of surfaces. This opens new possibilities, which can for instance include a biotin/streptavidin complex. As previously mentioned, establishing a good negative control was challenging. Applying a linker introduces the possibility of applying differently functionalized beads, which could enable the establishment of a proper negative control.

The importance of achieving a dense and homogenous surface functionalization was demonstrated for the flow chamber assay. Images of the coupon surface indicated areas of the coupon that had varying degrees of coverage of fumonisin B1 (figure 5.3). This would be a challenge when determining the sample area, due to a variable amount of attachment points for the *S. cerevisiae* cells. The surface should preferably contain single molecules and not large aggregates of the surface functionalization. The large aggregates and webs formed by fumonisin B1 molecules on the coupon surface might result in cells being trapped within these webs. Consequently, the measured adhesiveness might be due to the cells being physically restrained, rather than a specific interaction.

The required concentration of the surface functionalization has to be optimized for the molecule of interest. The formation of large aggregates and webs on the surface can be reduced by subjecting the solution to a sonciation treatment prior to the functionalization procedure.

For the optical tweezers, the density and homogeneity of the surface functionalization can be investigated by coupling a fluorescent tag to the molecule of interest. By applying a super-resolution microscope, such as the stimulated emission depletion (STED) microscope, the distribution of the molecule on the bead surface can be identified. The same principle can also be applied for the coupon surface, in order to give a more detailed characterization of the surface functionalization.

6.4 Microarray of *S. cerevisiae* on PLL patterned glass surface

The formation of a microarray of cells provides new possibilities for high throughput study of single cell events, or the investigation of interactions between pairs and triplets of cells [6]. Furthermore, it allows investigation of the cell response upon adhesion to different surfaces [38]. However, the immobilization of cells on the surface needs to be stable in order to obtain a reliable microarray platform. This requires an accurate deposition of patches of a chemical pro-

moting cell adhesion, on an otherwise cell-repellent surface.

6.4.1 Microcontact printing of PLL

The deposited PLL-pattern was successfully identified (figure 5.29), even though locating the pattern proved to be challenging. The pattern was also successfully deposited with PLL-FITC. However, some abnormalities of deposited pattern were observed, which were more clearly demonstrated by the deposition of PLL-FITC (figure 5.28). It was assumed that the weight had been applied inaccurate during deposition of the pattern. If the stamp is slightly moved during deposition, the deposited features will have more of a rod-like shape than round spheres. This can be a result of applying too much force when using the tweezers to push the glass against the stamp. It is thus important to be very gentle when applying the tweezers. The weight is important for obtaining sufficient contact between the stamp and glass surface, however, it must be deposited directly on top in order to prevent smearing on the glass surface. It is also important that the weight has a flat bottom, so that the weight is evenly distributed.

6.4.2 Adsorption of *S. cerevisiae* on a clean glass surface

The observed ability of *S. cerevisiae* cells to adhere to a clean glass surface does not correspond with the results obtained in the master theses by Åshild Samseth [93] and Karen Dunker [94]. If the glass slides applied in this master thesis were not completely clean after washing with ethanol and MQ water, then impurities on the glass surface may be responsible for the adhesion of the cells. This can be further investigated by applying different cleaning procedures, such as methanol and HCl.

6.4.3 Immobilization of *S. cerevisiae* on PLL-treated surface

S. cerevisiae was not successfully immobilized on a glass surface functionalized with PLL (0.01%). The results obtained by Åshild Samseth [93] and Karen Dunker [94] were thus not replicated.

The glass surface was pegylated in order to obtain an inert surface, since the *S. cerevisiae* cells were able to adhere to a clean glass slide. The pegylation was successful in preventing the adhesion of the *S. cerevisiae* cells 5.32. The attachment of PLL-g-PEG onto the glass surface

blocks the negatively charged glass surface from initiating electrostatic interactions with the PLL. If the PLL-g-PEG layer interfered with the attachment of PLL on the glass surface, then the surface will still present PEG side chains. As demonstrated, a pegylated surface will prevent cell adhesion, which could explain the removal of cells during washing.

However, the demonstrated PLL-pattern obtained by microcontact printing, confirms the deposition of PLL on a pegylated glass surface. It can thus be assumed that the PLL-covered glass surface also contains PLL. Furthermore, weight is applied when depositing the PLL-pattern, while the surface is just covered with the PLL solution for the PLL-covered glass slide. The applied weight might help PLL attach more strongly to the surface, while the PLL molecules are loosely attached on the PLL-coated glass. A weak interaction between the pegylated glass and PLL might result in removal of the PLL molecules during the wahsing procedure. Further investigation is required to determine the strength of the interaction between PLL and the pegylated surface.

It was hypothesized that the washing procedure applied was too strong, resulting in the detachment of cells. Several washing procedures were investigated, but they all achieved the same results. The interaction between PLL and *S. cerevisiae* cells is based on electrostatic interactions, which might be ruptured by the generated forces during washing. The assumption of the washing procedure being responsible for not obtaining immobilization of *S. cerevisiae* cells on PLL can be further substantiated by the observed aggregates, as well as the incomplete patterns formed by attached cells (5.30). If the washing procedure resulted in detachment of some cells, then they might have been moved during washing, and further formed aggregates with cells that were able to maintain their attachment to the PLL-surface.

Another possible factor affecting the immobilization of *S. cerevisiae* is the pH. The cells were suspended in HEPES, which has a pH of approximately 7.4. This is higher than the pH of MQ water (pH of $\sim$ 5.5). The increase in pH will result in a conformation change of PLL into α-helix due to the deprotonation of the amino groups [73]. This change in structure of PLL might affect the strength of interaction with the *S. cerevisiae* cells, rendering it weaker.

7. Recommendations for further work

7.1 Further investigation required in order to apply *S. cerevisiae* as an adsorbing agent

In order to apply *S. cerevisiae* as an adsorbing agent of fumonisin B1, the interaction must be characterized as specific. This is to prevent the possible adsorption of essential nutrients or other important compounds present in the gastrointestinal tract. The adsorption procedure also has to be optimized, in order to achieve an efficient adsorbing agent.

7.1.1 Further investigation of the effect of heat treatment

The effect of the heat treatment on the cell wall structure has to be further investigated, in order to understand the mechanism behind the increased adhesiveness. Biochemical measurements can be performed in order to characterize the carbohydrate composition of the cell wall. The amount of cell wall proteins should also be determined, which can be obtained based on the nitrogen content of the cell wall, as described in the study performed by Schiavone *et al.* (2014) [78]. It would be interesting to evaluate the context of the amount of cell wall proteins with the adhesiveness of the *S. cerevisiae* cells. The heat treatment also needs to be optimized, by testing different temperatures and incubation periods, in order to investigate the effect on the adhesiveness.

7.1.2 Investigate the role of the functional groups on fumonisin B1 in the formation of a yeast-mycotoxin complex

The role of the free amino group on fumonisin B1 in the formation of a yeast-mycotoxin molecule can be investigated by chemically removing or blocking the amino group. Examining the interaction capacity of fumonisin B1 with and without a free amino group can indicate the role of the amino group in forming an interaction with *S. cerevisiae*. This should also be investigated

for the acid moieties. The amino group and acid moieties can be removed through deamination and decarboxylation, respectively.

7.1.3 Identify the optimal structure of the polysaccharide chains

As indicated, a complex structure of β-glucan has been indicated to present more available adsorption sites [12]. It has also been demonstrated that the alkali-insoluble fraction of the β-glucan plays a major role in the formation of a yeast-mycotoxin complex [3, 13]. It would thus be interesting to repeat the experiments with β-glucan and fumonisin B1, where applying an insoluble fraction of β-glucan.

7.1.4 Alternative techniques for investigating the adhesiveness

The effect of immobilizing β-glucan and fumonisin B1 on their ability to interact should be further investigated. Restraining their ability to move can affect their interaction capacity, by not being able to reach the adsorption sites. The interaction capacity should therefore be further investigated in an aqueous solution, where both β-glucan and fumonisin B1 moves freely. This might allow the presence of different structures of β-glucan, which can promote an adsorption of fumonisin B1. Such an experiment should also be performed with viable and heat treated *S. cerevisiae* cells, in order to investigate if viable cells possesses the ability to adsorb fumonisin B1, which has been indicated by previous studies [4, 82, 83]. By measuring the amount of fumonisin B1 molecules added to the solution, the percentage of adsorbed molecules can be obtained by recording the amount of free molecules left after a certain time period.

Before the adhesiveness of *S. cerevisiae* can be investigated *in vivo*, several obstacles has to be solved. However, a possible experimental platform, which acts to mimic the *in vivo* environment, is the lab-on-a-chip (LOC). This can be obtained by creating a channel of epithelial cells from the gastrointestinal tract, which is surrounded by moving liquid, mimicking the blood flow. As mentioned, the formation of a yeast-mycotoxin complex is to prevent the adsorption of the mycotoxin molecules into the circulatory system. The adhesiveness can be measured by recording the percentage of adsorbed fumonisin B1 molecules, as described above. It also allows the investigation of the amount of fumonisin B1 molecules that might be able to cross the epithelial

cell layer and move over into the circulatory system. This can give an indication of the efficiency of *S. cerevisiae* as an adsorbing agent. The effect of different pH on the yeast-mycotoxin complexes can be investigated by changing the pH in the channel. This is relevant since the complex will be exposed to varying pH during its travel in the gastrointestinal tract.

7.1.5 Other applications of the investigated cellular adhesion

Investigation of the adsorption mechanism between *S. cerevisiae* and fumonisin B1 can offer other applications within the field of biology, immunology and pharmaceutics. Further understanding of cell behavior and cell interaction can be beneficial for other applications as well, such as the immunological effect of β-glucans.

7.2 Further work for obtaining a microarray of cells

Different chemicals promoting cell adhesion, such as other polycations, proteins or protein fragments [95], can be investigated for the fabrication of a microarray by the use of microcontact printing. As demonstrated in this master thesis, a successful immobilization of *S. cerevisiae* was not obtained on a PLL-treated surface. The interaction between PLL and *S. cerevisiae* should be investigated further, to determine the strength of this interaction. It would also be interesting if an inert glass surface could be obtained without applying PLL-g-PEG, by for instance an improved cleaning procedure. This could enable a direct attachment of PLL to the glass surface, which may have improved the stability of the deposited pattern and thus an improved immobilization of *S. cerevisiae*.

8. Conclusion

Optical tweezers offers the detection of weak interactions, like the interactions observed between *S. cerevisiae* and fumonisin B1. However, this technique was not able to give a reliable estimation of the frequency of interaction for the interacting pairs. Several factors were discovered to affect the estimation of the frequency of interaction. This includes the distribution of the polysaccharides and mycotoxin molecules on the bead surface, the amount of force applied to the beads in order to push them together, as well as the alignment of the traps. Another challenge was establishing a good negative control, since the amino-functionalized beads presented the ability to self-react. Consequently, it was difficult to identify specific interaction.

The flow chamber assay offered conditions that mimic the natural environment of cells, by introducing the *S. cerevisiae* cells to increased shear stress. However, determining the strength of the interaction was challenging, and the procedure for data collection should be improved to increase the reliability of the obtained data. A good cleaning procedure of the substrate surface was established, which improved the reliability of the results.

It was discovered that viable wild-type *S. cerevisiae* cells were not able to present interactions with fumonisin B1, when the adhesiveness was examined with the optical tweezers and flow chamber assay. Reducing the amount of mannan in the outer layer of the cell wall did not improve the adhesiveness of *S. cerevisiae*. Furthermore, the mannan and mannoprotein layer was concluded to not limit the access to the adsorption sites. The results indicated that β-glucan is the responsible cell wall component in an interaction with fumonisin B1. It was also indicated that the instrumental setup, which required immobilization of the polyssaccharides and mycotoxin molecules on either a glass surface or polystyrene beads, might have interfered with their ability to interact. The structure of β-glucan was assumed to be important for its ability to interact with fumonisin B1.

Subjecting *S. cerevisiae* cells to a heat treatment improved their adhesiveness of fumonisin B1. The treatment was assumed to interfere with the cell wall structure, which promoted the availability of the adsorption sites on β-glucan.

PLL-FITC enabled verification of successful deposition of PLL in a microscale pattern, by the use of microcontact printing. However, the immobilization of *S. cerevisiae* cells on a glass surface functionalized with a layer of PLL was not reproduced. Hence, a microarray of *S. cerevisiae* cells on a PLL patterned surface was not obtained. Several factors was identified to affect the interaction between PLL and *S. cerevisiae*, such as the pegylation of the glass surface, pH of the buffer and the forces introduced by the washing procedure.

Bibliography

1. Awad, W. A., Ghareeb, K., Böhm, J. & Zentek, J. Decontamination and detoxification strategies for the Fusarium mycotoxin deoxynivalenol in animal feed and the effectiveness of microbial biodegradation. *Food Additives and Contaminants - Part A Chemistry, Analysis, Control, Exposure and Risk Assessment* **27,** 510–520 (2010).

2. Marin, S., Ramos, A. J., Cano-Sancho, G. & Sanchis, V. *Mycotoxins: Occurrence, toxicology, and exposure assessment* 2013.

3. Yiannikouris, A. *et al.* Alkali extraction of β-D-glucans from Saccharomyces cerevisiae cell wall and study of their adsorptive properties toward zearalenone. *Journal of Agricultural and Food Chemistry* **52,** 3666–3673 (2004).

4. Pizzolitto, R. P., Salvano, M. A. & Dalcero, A. M. Analysis of fumonisin B 1 removal by microorganisms in co-occurrence with aflatoxin B 1 and the nature of the binding process. *International Journal of Food Microbiology* **156,** 214–221 (2012).

5. Friedrichs, J. *et al.* A practical guide to quantify cell adhesion using single-cell force spectroscopy. *Methods* **60,** 169–178 (2013).

6. Whitesides, G. M., Ostuni, E., Takayama, S., Jiang, X. & Ingber, D. E. Soft lithography in biology and biochemistry. *Annual review of biomedical engineering* **3,** 335–73 (2001).

7. Voss, K. A., Smith, G. W. & Haschek, W. M. *Fumonisins: Toxicokinetics, mechanism of action and toxicity* 2007.

8. Abbax, H. K., Gelderblom, W. C., Cawood, M. E. & Shier, W. T. Biological activities of fumonisins, mycotoxins from Fusarium moniliforme, in jimsonweed (Datura stramonium L.) and mammalian cell cultures. *Toxicon* **31,** 345–353 (1993).

9. Scott, P. M. Fumonisins. *International journal of food microbiology* **18,** 257–270 (1993).

10. IARC. IARC Monographs on the Evaluation of Carcinogenic Risks to Humans. In Some Traditional Herbal Medicines, Some Mycotoxins, Naphthalene and Styrene. *IARC Press* **82,** 437–550 (2002).

11. Nair, M. G. Fumonisins and human health. *Ann Trop Paediatr* **18,** S47–S52 (1998).

12. Yiannikouris, A. *et al.* Adsorption of Zearalenone by beta-D-glucans in the Saccharomyces cerevisiae cell wall. *J. Food Prot.* **67,** 1195–1200 (2004).

13. Yiannikouris, A. *et al.* Chemical and conformational study of the interactions involved in mycotoxin complexation with β-D-glucans. *Biomacromolecules* **7,** 1147–1155 (2006).

14. Yiannikouris, A. *et al.* Comprehensive conformational study of key interactions involved in zearalenone complexation with β-D-glucans. *Biomacromolecules* **5,** 2176–2185 (2004).

15. Neiman, A. M. Ascospore formation in the yeast Saccharomyces cerevisiae. *Microbiology and molecular biology reviews : MMBR* **69,** 565–584 (2005).

16. Madigan, M. T., Bender, K. S., Buckley, D. H., Martinko, J. M. & Stahl, D. A. in *Brock Biology of Microorganisms* 26–28, 423, 604, 179–181 (Pearson Education Limited, 2014).

17. Manners, D. J., Masson, A. J. & Patterson, J. C. The structure of a β-(1,3)-d-glucan from yeast cell walls. *Biochemical Journal* **135,** 19–30 (1973).

18. Orlean, P. *Architecture and biosynthesis of the Saccharomyces cerevisiae cell wall* 2012.

19. Levin, D. E. Regulation of cell wall biogenesis in Saccharomyces cerevisiae: The cell wall integrity signaling pathway. *Genetics* **189,** 1145–1175 (2011).

20. Klis, F. M., Mol, P., Hellingwerf, K. & Brul, S. *Dynamics of cell wall structure in Saccharomyces cerevisiae* 2002.

21. Vega, K. & Kalkum, M. *Chitin, chitinase responses, and invasive fungal infections* 2012.

22. Rees, D. A. & Scott, W. E. Polysaccharide conformation. Part VI. Computer model-building for linear and branched pyranoglycans. Correlations with biological function. Preliminary assessment of inter-residue forces in aqueous solution. Further interpretation of optical rotation in t. *Journal of the Chemical Society B: Physical Organic,* 469–479 (1971).

23. Klis, F. M., Boorsma, A. & De Groot, P. W. *Cell wall construction in Saccharomyces cerevisiae* 2006.

24. Samuelsen, A. B. C., Schrezenmeir, J. & Knutsen, S. H. *Effects of orally administered yeast-derived beta-glucans: A review* 2014.

25. Kollár, R. *et al.* Architecture of the Yeast Cell Wall. *Journal of Biological Chemistry* **272,** 17762–17775 (1997).

26. Kocourek, J. & Ballou, C. E. Method for fingerprinting yeast cell wall mannans. *Journal of Bacteriology* **100,** 1175–1181 (1969).

27. Jigami, Y. & Odani, T. *Mannosylphosphate transfer to yeast mannan* 1999.

28. Hirayama, S., Furukawa, S., Ogihara, H. & Morinaga, Y. Yeast mannan structure necessary for co-aggregation with Lactobacillus plantarum ML11-11. *Biochemical and Biophysical Research Communications* **419,** 652–655 (2012).

29. Kurita, K. *Chitin and chitosan: Functional biopolymers from marine crustaceans* 2006.

30. Arroyo, J., Bermejo, C., García, R. & Rodríguez-Peña, J. M. Genomics in the detection of damage in microbial systems: cell wall stress in yeast. *Clinical Microbiology and Infection* **15,** 44–46 (2009).

31. García, R. *et al.* The Global Transcriptional Response to Transient Cell Wall Damage in Saccharomyces cerevisiae and Its Regulation by the Cell Integrity Signaling Pathway. *Journal of Biological Chemistry* **279,** 15183–15195 (2004).

32. Kapteyn, J. C. *et al.* Altered extent of cross-linking of β1,6-glucosylated mannoproteins to chitin in Saccharomyces cerevisiae mutants with reduced cell wall β1,3- glucan content. *Journal of Bacteriology* **179,** 6279–6284 (1997).

33. Smits, G. J., Kapteyn, J. C., van den Ende, H. & Klis, F. M. Cell wall dynamics in yeast. *Current opinion in microbiology* **2,** 348–352 (1999).

34. Delley, P. A. & Hall, M. N. Cell wall stress depolarizes cell growth via hyperactivation of RHO1. *Journal of Cell Biology* **147,** 163–174 (1999).

35. Arnfinnsdottir, N. B., Ottesen, V., Lale, R. & Sletmoen, M. The design of simple bacterial microarrays: Development towards immobilizing single living bacteria on predefined micro-sized spots on patterned surfaces. *PLoS ONE* **10** (2015).

36. De Souza, N. Single-cell methods. *Nature Methods* **7,** 35 (2009).

37. Mele, E. & Pisignano, D. Nanobiotechnology: soft lithography. *Progress in molecular and subcellular biology* **47,** 341–358 (2009).

38. Qin, D., Xia, Y. & Whitesides, G. M. Soft lithography for micro- and nanoscale patterning. *Nature Protocols* **5,** 491–502 (2010).

39. Pompe, W. *Bio-nanomaterials : designing materials inspired by nature* (ed Pompe, W.) 149–181 (Wiley-Vch, Weinheim, Germany, 2013).

40. Moore, P. B. in *Visualizing the Invisible* (Oxford University Press, 2012).

41. Baker, W. L. The Light Microscope. *Australian Science Teachers Journal* **41,** 62–65 (1995).

42. Sletmoen, M., Davies, C., Psonka-Antonyczyk, K. & Stokke, B. *Biophysical Nanotechnologies: lecture notes for the PhD course in Light and force based molecular imaging* Trondheim, 2011.

43. Jenkins, F. A. & White, H. E. *Fundamentals of optics* 4th (McGraw-Hill, Auckland, 1976).

44. Neuman, K. C. & Block, S. M. *Optical trapping* 2004.

45. Simmons, R. M., Finer, J. T., Chu, S. & Spudich, J. A. Quantitative measurements of force and displacement using an optical trap. *Biophysical Journal* **70,** 1813–1822 (1996).

46. Parasad, P. N. *Introduction to biophotonics* 487–490 (John Wiley & Sons, 2004).

47. Neuman, K. C. & Nagy, A. *Single-molecule force spectroscopy: Optical tweezers, magnetic tweezers and atomic force microscopy* 2008.

48. Berg-Sørensen, K. & Flyvbjerg, H. Power spectrum analysis for optical tweezers. *Review of Scientific Instruments* **75,** 594–612 (2004).

49. Evans, E. & Ritchie, K. Dynamic strength of molecular adhesion bonds. *Biophysical Journal* **72,** 1541–1555 (1997).

50. Evans, E. Introductory Lecture Energy landscapes of biomolecular adhesion and receptor anchoring at interfaces explored with dynamic force spectroscopy. *Faraday Discussions* **111,** 1–16 (1999).

51. Taninaka, A., Hirano, Y., Takeuchi, O. & Shigekawa, H. Force measurement enabling precise analysis by dynamic force spectroscopy. *International Journal of Molecular Sciences* **13,** 453–465 (2012).

52. Bizzarri, A. R. & Cannistraro, S. The application of atomic force spectroscopy to the study of biological complexes undergoing a biorecognition process. *Chemical Society reviews* **39,** 734–749 (2010).

53. Lane, W. O. *et al.* Parallel-plate Flow Chamber and Continuous Flow Circuit to Evaluate Endothelial Progenitor Cells under Laminar Flow Shear Stress. *Journal of Visualized Experiments* (2012).

54. Bacabac, R. G. *et al.* Dynamic shear stress in parallel-plate flow chambers. *Journal of Biomechanics* **38,** 159–167 (2005).

55. Martines, E., McGhee, K., Wilkinson, C. & Curtis, A. A Parallel-plate flow chamber to study initial cell adhesion on a nanofeatured surface. *IEEE Transactions on Nanobioscience* **3,** 90–95 (2004).

56. Le, D. T. L. *et al.* Unraveling the role of surface mucus-binding protein and pili in muco-adhesion of Lactococcus lactis. *PLoS ONE* **8** (2013).

57. Castelain, M. *et al.* Oligomerized backbone pilin helps piliated Lactococcus lactis to withstand shear flow. *Biofouling* **32,** 911–923 (2016).

58. Cosenza, V. a., Navarro, D. a. & Stortz, C. a. Usage of alpha-picoline borane for the reductive amination of carbohydrates. *Arkivoc* **2011,** 182–194 (2011).

59. Ruhaak, L. R., Steenvoorden, E., Koeleman, C. A. M., Deelder, A. M. & Wuhrer, M. 2-Picoline-borane: A non-toxic reducing agent for oligosaccharide labeling by reductive amination. *Proteomics* **10,** 2330–2336 (2010).

60. Xia, Y. & Whitesides, G. M. SOFT LITHOGRAPHY. *Annual Review of Materials Science* **28,** 153–184 (1998).

61. Mack, C. A. *Fundamental Principles of Optical Lithography : The Science of Microfabrication* English (Wiley-Interscience, Chichester, 2007).

62. Menon, R., Patel, A., Gil, D. & Smith, H. I. Maskless lithography. *Materials Today* **8,** 26–33 (2005).

63. Diez, S. *The next generation of maskless lithography* in *Emerging Digital Micromirror Device Based Systems and Applications VIII* **9761** (International Society for Optics and Photonics, 2016), 976102.

64. Shaw, J., Gelorme, J., Labianca, N., Conley, W. & Holmes, S. Negative photoresists for optical lithography. *IBM Journal of Research and Development* **41,** 81–94 (1997).

65. Alom Ruiz, S. & Chen, C. S. Microcontact printing: A tool to pattern. *Soft Matter* **3,** 168–177 (2007).

66. Murray, L. M., Nock, V., Evans, J. J. & Alkaisi, M. M. Bioimprinted polymer platforms for cell culture using soft lithography. *Journal of Nanobiotechnology* **12** (2014).

67. Kaufmann, T. & Ravoo, B. J. Stamps, inks and substrates: polymers in microcontact printing. *Polymer Chemistry* **1,** 371 (2010).

68. Bernard, A., Renault, J. P., Michel, B., Bosshard, H. R. & Delamarche, E. Microcontact printing of proteins. *Advanced Materials* **12,** 1067–1070 (2000).

69. Hermanson, G. T. in *Bioconjugate Techniques* 3rd ed., 787–838 (Academic press, 2013).

70. Harris, J. M. in *Poly(Ethylene Glycol) Chemistry* 1–14 (Springer, 1992).

71. Holmberg, K., Bergström, K. & Stark, M.-B. in *Poly (Ethylene Glycol) Chemistry* 303–304 (Springer, 1992).

72. Kenausis, G. L. *et al.* Poly (L-lysine)-g-poly (ethylene glycol) layers on metal oxide surfaces: attachment mechanism and effects of polymer architecture on resistance to protein adsorption. *The Journal of Physical Chemistry B* **104,** 3298–3309 (2000).

73. Mirtič, A. & Grdadolnik, J. The structure of poly-L-lysine in different solvents. *Biophysical Chemistry* **175-176,** 47–53 (2013).

74. Choi, J.-H. *et al.* Influence of pH and Surface Chemistry on Poly(l -lysine) Adsorption onto Solid Supports Investigated by Quartz Crystal Microbalance with Dissipation Monitoring. *The Journal of Physical Chemistry B* **119,** 10554–10565 (2015).

75. Eckenrode, H. M. & Dai, H. L. Nonlinear optical probe of biopolymer adsorption on colloidal particle surface: Poly-L-lysine on polystyrene sulfate microspheres. *Langmuir* **20,** 9202–9209 (2004).

76. Mazia, D., Schatten, G. & Sale, W. Adhesion of cells to surfaces coated with polylysine: Applications to electron microscopy. *Journal of Cell Biology* **66,** 198–200 (1975).

77. Aguilar-Uscanga, B. & François, J. M. A study of the yeast cell wall composition and structure in response to growth conditions and mode of cultivation. *Letters in Applied Microbiology* **37,** 268–274 (2003).

78. Schiavone, M. *et al.* A combined chemical and enzymatic method to determine quantitatively the polysaccharide components in the cell wall of yeasts. *FEMS Yeast Research* **14,** 933–947 (2014).

79. Pierce, T. S. Crosslinking technical handbook. *Thermo Fisher Scientific, Rockford, IL, USA* (2009).

80. Wozniak, a., van Mameren, J. & Ragona, S. Single-molecule force spectroscopy using the NanoTracker optical tweezers platform: from design to application. *Current pharmaceutical biotechnology* **10,** 467–73 (2009).

81. Firmin, S. *et al.* Modification of aflatoxin B1 and ochratoxin a toxicokinetics in rats administered a yeast cell wall preparation. *Food Additives and Contaminants - Part A Chemistry, Analysis, Control, Exposure and Risk Assessment* **27,** 1153–1160 (2010).

82. Armando, M. R. *et al.* Statistical optimization of culture conditions for biomass production of probiotic gut-borne Saccharomyces cerevisiae strain able to reduce fumonisin B1. *Journal of Applied Microbiology* **114,** 1338–1346 (2013).

83. Taran, F. *et al.* Evaluation of Saccharomyces cerevisiae as an anti-fumonisin B1 additive in a horse digestion model. *World Mycotoxin Journal* **10** (2017).

84. Qin, F., Sletmoen, M., Stokke, B. T. & Christensen, B. E. Higher order structures of a bioactive, water-soluble (1,3)-β-d- glucan derived from Saccharomyces cerevisiae. *Carbohydrate Polymers* **92,** 1026–1032 (2013).

85. Qin, F., Kes, M. & Christensen, B. E. A study of bioactive, branched (1,3)-β-d-glucans in dimethylacetamide/LiCl and dimethyl sulphoxide/LiCl using size-exclusion chromatography with multi-angle light scattering detection. *Journal of Chromatography A* **1305,** 109–113 (2013).

86. Bejaoul, H., Mathieu, F., Taillandier, P. & Lebrihi, A. Ochratoxin A removal in synthetic and natural grape juices by selected oenological Saccharomyces strains. *Journal of Applied Microbiology* **97,** 1038–1044 (2004).

87. Bickle, M., Delley, P. A., Schmidt, A. & Hall, M. N. Cell wall integrity modulates RHO1 activity via the exchange factor ROM2. *EMBO Journal* **17,** 2235–2245 (1998).

88. Pillet, F. *et al.* Uncovering by Atomic Force Microscopy of an original circular structure at the yeast cell surface in response to heat shock. *BMC Biology* **12** (2014).

89. Rikhvanov, E., Fedoseeva, I., Varakina, N., Rusaleva, T. & Fedyaeva, A. Mechanism of Saccharomyces cerevisiae yeast cell death induced by heat shock. Effect of cycloheximide on thermotolerance. *Biochemistry (Mosc)* **79,** 16–24 (2014).

90. Adya, A. K., Canetta, E. & Walker, G. M. Atomic force microscopic study of the influence of physical stresses on Saccharomyces cerevisiae and Schizosaccharomyces pombe. *FEMS Yeast Research* **6,** 120–128 (2006).

91. Friddle, R. W., Sulchek, T. a., Albrecht, H. & Noy, A. Counting and Breaking Individual Biological Bonds: Force Spectroscopy of Tethered Ligand-Receptor Pairs. *Current Nanoscience* **3,** 41–48 (2007).

92. Friddle, R. W., Noy, A. & De Yoreo, J. J. Interpreting the widespread nonlinear force spectra of intermolecular bonds. *Proceedings of the National Academy of Sciences* **109,** 13573–13578 (2012).

93. Samseth, Å. *Immobilisering av Saccharomyces Cerevisiae og virkning av kitosan på den mekaniske styrken til celleveggen til Saccharomyces Cerevisiae* Master thesis (NTNU, Trondheim, 2016).

94. Dunker, K. *Microarrays for High Throughput Analysis of Cellular Heterogeneity* Master thesis (NTNU, Trondheim, 2017).

95. Blau, A. *Cell adhesion promotion strategies for signal transduction enhancement in microelectrode array in vitro electrophysiology: An introductory overview and critical discussion* 2013.

Appendices

A. Acronyms

AFM Atomic force microscopy

BSA Bovine serum albumin

CWP Cell wall protein

μCP Microcontact printing

DI De-ionized water

FB1 Fumonisin B1

FITC Fluorescein isothiocyanate

MQ MilliQ water

NA Numerical aperture

OT Optical tweezers

PBS Phosphate buffered saline

PDMS Polydimethylsiloxane

PEG Poly(ethylene glycol)

PIR Proteins with internal repeats

PLL Poly-L-lysine

QPD Quadrant photodiode

S. cerevisiae Saccharomyces cerevisiae

YPD Yeast extract peptone dextrose

WT wild-type strain of *Saccharomyces cerevisiae*

B. Preparation of solutions

YPD medium preparation instructions

If using YPD power mix, 50 g is suspended in 1 L of distilled water. When using separate products; 10 g of yeast extract, 20 g of bactopeptone and 20 g glucose are mixed and suspended in 1 L of destilled water. The medium was autoclaved at 121°C for 20 min.

When preparing YPD medium for agar plates, 15 g of agar was added to the 1 L YPD medium.

Preparation of PBS buffer

A PBS buffer was prepared by dissolving 40.91 g of $NaCl$, 1.0065 g of KCl, 18.0860 g of Na_2HPO_4 and 1.2250 g of KH_2PO_4 in 5 L of demineralised water. The pH of the buffer was adjusted to approximately 7,5.

C. Percentage of interaction for optical tweezers experiments

The percentage of interaction obtain for the different interacting pairs examined with the optical tweezers are presented in table C.1

Table C.1: A summary of all experiments performed with the optical tweezers, presenting the percentage of interaction observed for each of the examined interacting pairs.

Interacting pairs	**Curves with interactions**	**Total number of curves**	**Percentage (%)**
β-glucan - fumonisin B1 (amino bead)	132	839	15.7
β-glucan - amino bead	52	837	6.2
β-glucan - fumonisin B1 (carboxyl bead)	18	817	2.2
β-glucan - carboxyl bead	26	812	3.2
Mannan - fumonisin B1 (amino bead)	21	828	2.5
Mannan - amino bead	14	790	1.8
Mannan - fumonisin B1 (carboxyl bead)	28	827	3.4
Mannan - carboxyl bead	4	830	0.5
Fumonisin B1 - amino bead	37	886	4.2
Amino bead - amino bead	342	1389	24.6
Amino bead - carboxyl bead	86	899	9.6

D. Data analysis of flow chamber experiments

D.1 Calculations of parameters for analysis

The parameters buffer flow rate and shear stress were automatically calibrated by the custom made excel sheet.

Buffer flow rate

The buffer flow rate, also referred to as the mass flow (Q) is obtained by:

$$\text{flow rate} = \frac{\text{weight of run through buffer (g)}}{\text{duration of stress (s)}} \tag{D.1}$$

An example of an flow chamber experiment and the corresponding measurements recorded in the custom made excel sheet is presented in figure D.1. For the measurement after the washing procedure, the following flow rate was calculated:

$$Q = \frac{13.723}{600} = 0.0229\text{mL/s} \tag{D.2}$$

Shear stress

The shear stress is obtained by the following equation:

$$\tau_w = \frac{3\mu Q}{4h^2 l} \tag{D.3}$$

with Q corresponding to the mass flow (m^3/s), μ is the fluid dynamic viscosity, h is the half-height of the channel and l is the half-width of the chamber.

The height of the channel is 0.2 mm and the length is 25.2 mm. For the same measurement

as examined above, with a flow rate of 0.0229 mL/s, the following shear stress was obtained:

$$\tau_w = \frac{3 \times 0.001 \times 0.0229 \times 0.000001}{4 \times (0.2/2 \times 0.001)^2 \times (25.2 \times 0.001)} \approx 0.07\text{Pa} \tag{D.4}$$

Position of constant-level tank (cm)	Graduation of pump (Pa)	Weight of run through buffer (g)	Duration of stress (s)	Buffer flow rate (mL/sec)	Shear Stress (Pa)	Number of cells	N/N_0 -	% of adhesion %
26,7	BEFORE wash					267		
28	AFTER wash	13,723	600	0,0229	0,07	11	1,571	157,143
32	0	11,113	180	0,062	0,55	8	1,143	114,286
34	0	14,368	180	0,080	0,37	8	1,143	114,286
38	0	20,735	180	0,115	0,48	8	1,143	114,286
42	0	26,97	180	0,150	0,69	7	1,000	100,000
46	0	32,488	180	0,180	0,89	7	1,000	100,000
50	0	37,353	180	0,208	1,07	7	1,000	100,000
54	0	42,326	180	0,235	1,24	7	1,000	100,000
58	0	47,075	180	0,262	1,40	7	1,000	100,000
62	0	51,513	180	0,286	1,56	7	1,000	100,000
66	0	57,064	180	0,317	1,70	7	1,000	100,000
70	0	61,816	180	0,343	1,887	7	1,000	100,000
74	0	66,17	180	0,368	2,04	7	1,000	100,000
78	0	70,564	180	0,392	2,19	7	1,000	100,000
80	0	74,395	180	0,413	2,33	7	1,000	100,000
80	5	106,143	180	0,590	2,46	6	0,857	85,714
80	10	152,25	180	0,846	3,51	6	0,857	85,714
80	20	300,84	180	1,671	5,03	4	0,571	57,143
80	25	376,28	180	2,090	9,95	0	0,000	0,000
80	30		180	0,000	12,44		0,000	0,000
80	35		180	0,000	0,00		0,000	0,000
80	40		180	0,000	0,00		0,000	0,000
80	45		180	0,000	0,00		0,000	0,000
80	50		180	0,000	0,00		0,000	0,000
80	55		180	0,000	0,00		0,000	0,000
80	60		180	0,000	0,00		0,000	0,000
80	65		180	0,000	0,00		0,000	0,000
80	70		180	0,000	0,00		0,000	0,000
80	75		180	0,000	0,00		0,000	0,000
80	80		180	0,000	0,00		0,000	0,000
80	85		180	0,000	0,00		0,000	0,000
80	90		180	0,000	0,00		0,000	0,000

Figure D.1: Demonstration of custom made excel sheet for recording weight of run through buffer and number of cells for each measurement. The excel sheet automatically calibrates the buffer flow rate, shear stress and percentage of adhesion for each measurement.